Quasicrystal systems with simple symmetries

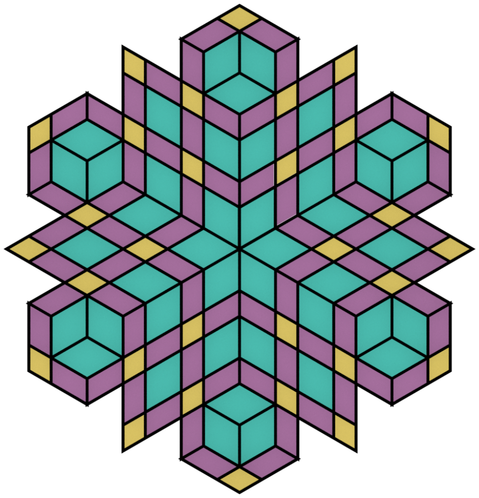

Thesis submitted in accordance with the requirements of the University of Liverpool for
the degree of Doctor in Philosophy by

Sam Coates

February 2019

Abstract

The primary investigations of this thesis concern epitaxial studies upon quasicrystal surfaces: specifically, quasicrystal surfaces which display rotational symmetries found in periodic systems. These types of quasicrystal surfaces are often overlooked. As a result, adsorption or structural phenomena which may be unique to these systems is under–reported. This work aims to bridge this gap.

Using experimental surface science techniques such as STM and LEED, adsorbates on quasicrystal surfaces with 2–fold and 3–fold rotational symmetries have been investigated. In each case, the structure of the clean substrate has also been re–evaluated either with regards to structural models or to geometric constructs such as tilings.

C_{60} molecules deposited on the 2–fold *i*–Al–Pd–Mn surface were found to arrange in a formation known as a Fibonacci square grid – a quasicrystalline structure with 4–fold symmetry. This resulted in the first reported physical example of a Fibonacci square grid. A surface model was used which produces a Mn distribution which matches the geometry of the C_{60} network – indicating that C_{60} molecules adsorb exclusively at Mn atoms, motivated by electron exchange. As a consequence, an open question on the specific structure of the 2–fold *i*–Al–Pd–Mn surface was answered.

Pb adsorption on the 2–fold and 3–fold surfaces of the *i*–Ag–In–Yb system was also explored. This work built on a previous study, where Pb was observed to grow in quasicrystalline layers on the 5–fold *i*–Ag–In–Yb surface. Each layer exhibited a unique structure, explained using planes from the bulk *i*–Ag–In–Yb model. Here, for the 3–fold system, Pb follows a similar adsorption scheme, where each layer is structurally similar to specific planes in the bulk. However, a difference in the density of 'available' adsorption sites in the surface plane leads to a different growth mode. Instead of a layer–by–layer mechanism, Pb was found to grow along z in a quasi–island type fashion, producing 3 dimensional nano–structures.

On the 2–fold *i*–Ag–In–Yb surface, the density of available sites again changed the growth mode. Instead of being explained by bulk planes, Pb adopted the highly dense structure of the substrate, sitting at adsorption sites with high geometry, producing a quasi–Stranski–Krastanov type film.

Additional work includes a new type of aperiodic tiling with 3–fold symmetry. The first example of its kind, this tiling is derived in a similar fashion to the Penrose tiling, and is used to re–examine the 3–fold *i*–Ag–In–Yb surface.

Acknowledgements

Collecting the past three and a half years of work into one volume has been both rewarding and has allowed a certain amount of reflection on my time spent at the University of Liverpool. Having arrived here initially only to complete a Bachelor's degree in Physics, I'd like to thank all those who consciously and unconsciously persuaded me to keep at it. In particular, I'd like to thank Dr. Hem Raj Sharma and Prof. Ronan McGrath who invited me into their group, an act which allowed me to realise which professional path I wanted to follow.

In terms of teaching me the ropes (and beyond) in experimental surface science, I'd like to thank Dr. Sam Haq and Dr. Abdullah Al–Mahboob, whose help and advice gave me an excellent foundation on what (and what not) to do in the lab. Also included in these thanks is Dr. Joe Smerdon, who has also provided both experimental and theoretical insight. Likewise, thanks go to Dr. Julian Ledieu and Dr. Vincent Fournée for the use of their lab in France which started an experiment which is still providing questions and inspiration for further study.

Extra thanks go to Prof. Uwe Grimm and Dr. Ron Lifshitz, whose advice on aperiodic tilings proved extremely useful for this work. Likewise, thanks must go to Stuart Thorn, who collected the data presented in Chapter 7. I'd also like to thank the Engineering and Physical Sciences Research Council and C–MAC committee for providing funding for my research, presentations at conferences, and travel.

Finally, I thank those who have both kept me sane, and also provided that touch of insanity needed in life. To everyone in the tea–room: thank you. Work never feels like work with you around (especially when tea breaks last over an hour...). To the invaluable friends I have made since the start of my University of Liverpool career – I couldn't have done it without you. To my Mum, Dad, and Shelly, whose support is unwavering – the advice to 'do what makes you happy' is a life lesson worth taking. To my sister, Ruby, who is a constant source of inspiration and marvel. And ultimately, to Hannah, whose love and support have empowered me to do things I thought I could not.

Sam Coates, 2019

Contents

Glossary of concepts

$\boldsymbol{\tau}$	An irrational number known as the golden ratio, given as $\tau = \frac{1+\sqrt{5}}{2}$ = 1.618.... The golden ratio is linked to the Fibonacci sequence (1, 1, 2, 3, 5, 8,...), where the ratio of consecutive terms tends towards τ. It is a value interlinked with the studies of icosahedral quasicrystals. As such, evidence of 'τ–scaling' – the multiplication or division of dimensional values in experimental data – is often used as a marker to indicate quasiperiodic order.
Hyperspace	Refers to any space with a higher dimensionality than 3D. For example, '5D hyperspace'.
Tilings	Constructs which use geometric shapes (tiles) to fill a plane with no gaps or overlaps between tiles. Aperiodic tilings are often used to visualise quasiperiodic order in 2D.

Chapter 1

Introduction

Quasicrystals are materials which exhibit long–range order, but are aperiodic in nature. The surfaces of intermetallic quasicrystals provide a stimulating topic for experimental exploration, as they give rise to aesthetically pleasing structural arrangements quite unlike crystalline surfaces studied within the field. Likewise, adsorption studies upon these surfaces can give unique or unexpected results compared to conventional epitaxy. As such, exploring quasicrystalline epitaxy to the same extent of crystalline epitaxy (including a full range of adsorbate types on all available quasicrystalline surface structures) could give invaluable information not only on quasicrystal chemistry and formation, but could, for example, uncover new adsorption growth–mode schemes.

Contained within this thesis, then, are studies of quasicrystal surfaces which are often over–looked, i.e. those with rotational symmetries commensurate with periodic systems (in this case, 2–fold and 3–fold symmetric). In each case, the clean surface has been reinterpreted with respect to structural models, or to tilings with coincidental rotational symmetry. As a consequence, the understanding of each surface is increased. Subsequently, adsorption studies of molecules and elements are conducted to demonstrate the potential for templated growth on these newly understood systems.

The thesis is structured as follows. Chapter 2 provides an introduction into quasicrystals, including their place in crystallography, tools for understanding aperiodic long–range order, and models for visualizing their structure. Chapter 3 details the mechanics, history, and current state of adsorption on quasicrystal surfaces. A brief survey of the experimental techniques used, Scanning Tunnelling Microscopy (STM) and Low Electron Energy Diffraction (LEED) are detailed in Chapter 4.

Chapter 5 presents LEED and STM images of the clean and C_{60} dosed 2–fold *i*–Al–Pd–Mn surface. The C_{60} adsorption network is matched to a Mn distribution in a model of the clean surface. Chapter 6 introduces 2 new related aperiodic tilings which display 3–fold rotational symmetry. In Chapter 7, one of these tilings is used to reinterpret the 3–fold *i*–Ag–In–Yb surface. Subsequent Pb deposition on this surface presents a unique adsorption growth–mode. Likewise, Chapter 8 shows STM images of the 2–fold *i*–Ag–In–Yb surface with enhanced resolution compared to previous studies, which are then matched to a structural model. Again, Pb is deposited, which is found to adsorb at sites of high geometry.

Finally, a summary of all results and a comment on the future of each project is contained within Chapter 9.

Chapter 2

Quasicrystals

Quasicrystalline phases of matter have been observed in a range of materials and are now considered to be a sub–category of crystalline materials, which are defined as those materials which exhibit a discrete diffraction pattern. Typically, a quasicrystalline material is described as possessing long-range aperiodic order with no translational symmetry. Most commonly, these materials can display 'unusual' orders of rotational symmetry, where unusual is considered an order of symmetry which is incommensurate with periodic or Bravais lattice systems (for example, 5–fold, 10–fold, 12–fold). Intermetallic alloys exhibiting these structural properties are the most abundant and most studied quasicrystalline systems, and are called 'quasicrystals' (QCs), derived and shortened from 'quasi–periodic crystals' [1,2].

The first quasicrystal was reported in 1984, by Shechtman, Blech, Gratias and Cahn [1]. Their work described a diffraction pattern obtained from a rapidly quenched Al–Mn melt, which appeared to exhibit aperiodic order with icosahedral symmetry, including 5–fold rotational axes. The idea of a singular phase of a material displaying these properties was not immediately accepted, as an aperiodic system showing long–range order (as evidenced by a diffraction pattern) appeared to be counter–intuitive. Indeed, initial attempts to understand this structure using the then current laws of crystallography included the idea of crystal twinning, where overlapping crystal structures mimic unusual degrees of symmetry [3]. However, by considering entirely new structural arrangements, Blech found a system of 'random packing(s) of non–overlapping parallel icosahedra' which adroitly explained the diffraction pattern observed [1]. Consequently, crystallography was fundamentally changed, and an entirely new category of solid–state structural order had been discovered. Shechtman earned a Nobel prize in Chemistry for this work (2011). To date, there are over

100 chemically unique intermetallic quasicrystals [4,5]. Typically, these are ternary alloys, although stable binary and quaternary QCs also exist [6–9]. Rotational symmetries of these systems range from 5–fold to 10–fold. Intermetallic QCs are created using classical crystal growth techniques, where close control of stoichiometry and growth parameters is required to produce quasicrystalline phases. Two dimensional quasicrystals have also been manufactured at crystalline surface interfaces using a range of materials (metals, colloids, polymers etc.). These have been shown to have 8–, 12–, and 18–fold rotational symmetries [10–13].

So far, intermetallic quasicrystals have limited technological use, although their potential has been explored within numerous fields. Their low friction, high hardness, and corrosion resistance have made them interesting candidates for metallic coatings for use in cooking utensils, or as inclusions in surgical tools [14]. Equally, their chemical properties have been explored with respect to catalysis in the steam reforming of methanol – a method of producing hydrogen [15]. However, technological advancement has been slow compared to ‘traditional’ alloys. Their brittleness is a drawback for coating applications, and there is difficulty in up–scaling materials for industrial catalytic processes when close control of growth is required [16].

Relating the properties of quasicrystals to specific structural aspects is a non–trivial problem. First, how does the structural complexity of a 3–dimensional aperiodic system explicitly affect its physical properties? Second, how much are the physical properties influenced by the chemical complexity of the groups of atoms decorating the vertices of such a material? Reducing the amount of structural or chemical complexity in these systems whilst retaining the essence of a quasicrystalline material provides a plausible approach to understanding these difficult questions. It is also a motivation for this work.

From this standpoint, pre–quasicrystalline crystallographic concepts will be introduced. Following this, aperiodic schemes for producing long–range order will be presented, showing how, for example, n ≥ 5 symmetries are obtained in a crystallographic system. From here, the relationship between these aperiodic arrangements and quasicrystal structure will be developed, necessary for the understanding of further work.

2.1 Basic Crystallography

Crystallography is a basic aspect of solid–state physics. The structure of any crystalline material can be described with respect to one of the 14 Bravais lattices. Here, a lattice

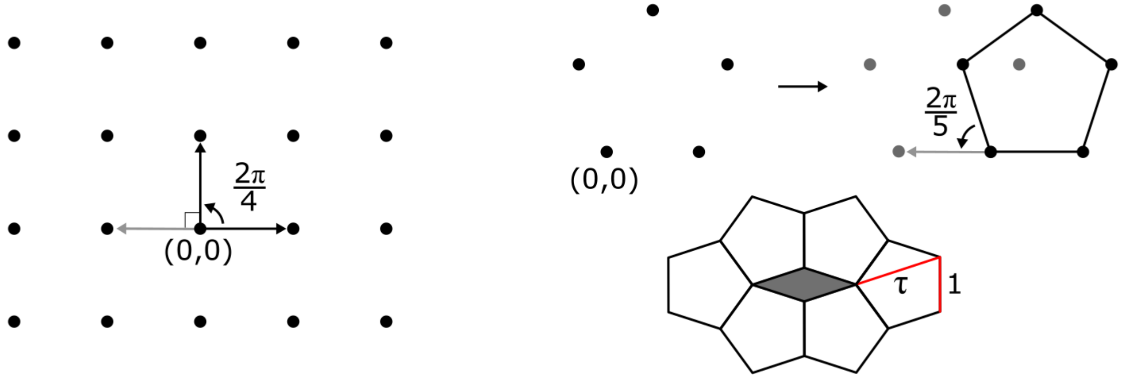

Figure 2.1: **Pre–quasicrystalline crystallography:** **(a)** A square lattice labelled with its unit vectors. A rotation of $\frac{2\pi}{4}$ reproduces the original lattice. **(b)** Pentagonal 'lattice' rotated by $\frac{2\pi}{5}$ fails to reproduce original points. **(c)** Packing of 5–fold units does not cover all space. The ratio between a pentagon's diameter and edge length is shown (τ:1).

describes an infinite set of points arranged in a periodic fashion so that each point is identical, with identical environments. A position vector, **R**, describes how one can translate one lattice point to another:

$$\boldsymbol{R} = n_1\mathbf{a} + n_2\mathbf{b} + n_3\mathbf{c} \tag{2.1}$$

where n_i are integers, and **a, b,** and **c** are translation vectors.

The 14 Bravais lattices reflect the maximum number of ways these periodic lattice points can be arranged in 3–dimensional space. Each Bravais lattice can be described in terms of a crystallographic unit cell – an infinitely repeating unit of points which fills space periodically and completely. By placing a basis (here, an atom or groups of atoms) at each lattice point of a unit cell, we obtain 230 separate symmetry groups by simply combining various symmetry operations upon the Bravais lattices, such as rotation and reflection. Every crystalline structure can be described by one of these 230 space groups, no matter how complex.

We can show how 'allowed' rotational symmetries are linked to these lattice structures using a 2D example, Figure 2.1. Here, we can rotate the vectors used to describe a square lattice about a single arbitrary lattice point. Every $\frac{2\pi}{4}$ turn produces lattice points that can be mapped using translations of the lattice vectors. This can similarly be completed with any Bravais lattice, so long as the angle of rotation maps the original lattice onto itself. Permitted rotations are 2π, $\frac{2\pi}{2}$, $\frac{2\pi}{3}$, $\frac{2\pi}{4}$, $\frac{2\pi}{6}$, (1–, 2–, 3–, 4–, and 6–fold respectively).

We can easily show how 5–fold symmetry cannot be used in a similar fashion. If we take a set of points defined by a regular pentagon, and, starting from an arbitrary origin, rotate the system by $\frac{2\pi}{5}$, we create points that are not mapped onto the original lattice. Similarly, if we attempt the inverse by constructing a periodic lattice with 5–fold units, we cannot fill all space. The same can be said for any n–fold unit, where $n > 6$, and n is an integer.

These rules are generalised by the crystallographic restriction theorem [17]. Thus we have shown that, using the basic tools of crystallography, 5–fold symmetry is incompatible with periodicity. The same is true for other forbidden rotational symmetries.

2.2 Aperiodic order

Aperiodicity with long–range order is the hallmark of a quasicrystal. Here, several examples will be given of aperiodic order, in 1 and 2 dimensions. Included in this explanation is how an aperiodic sequence can evidence long–range order, in the form of a diffraction pattern.

2.2.1 Fibonacci Sequence

The simplest ‘quasicrystal’ is a 1–dimensional set of segments, known as the Fibonacci chain or sequence. It is used frequently in the analysis of QCs, as it is a simple model to illustrate quasiperiodic order. It will be explained by three techniques, as all are pertinent for later discussions: the substitution, cut and project, and section methods.

Substitution

If we consider two segment lengths, S, short, and L, long, and two substitution rules, $S \to L$ and $L \to LS$, we can generate aperiodic order as follows:

$$\begin{array}{ll} (1) & L \\ (2) & LS \\ (3) & LSL \\ (4) & LSLLS \\ (5) & LSLLSLSL... \end{array} \tag{2.2}$$

where (n) is the number of generations. Here, each segment of the chain at each generation is treated individually and substituted according to the substitution rules. For example, generation 4, *LSLLS*, is considered as 5 separate segments, *L, S, L, L, S*. Each segment is then replaced according to the substitution rules.

If the ratio of L/S is an irrational number, we can guarantee that segment vertex points on a line corresponding to the Fibonacci sequence have no translational symmetry. Conventionally, the irrational number used is the golden ratio, given as $\tau = \frac{(1+\sqrt{5})}{2} = 1.618...$, associated with the ratio between successive terms of the numerical Fibonacci sequence (1, 1, 2, 3, 5, 8, 13,...). The golden ratio is a useful tool in quasicrystal studies – the icosahedron, a Platonic solid which is used to characterize a family of quasicrystals (discussed later) is defined by vertex coordinates calculated by a cyclical permutation of (0, ± 1, $\pm\tau$). As a result, experimental evidence of τ–scaling (i.e. multiples or factors of τ) between dimensional quantities in a quasicrystal is often used as a de facto method to quickly assess quasiperiodicity. As a theoretical 1D example, we can consider the ratio of L and S segments in successive generations of the Fibonacci chain. Here, the sum of L segments across two consecutive generations are divided by the sum of S segments across the same generations:

$$\begin{aligned}
G_{2\rightarrow 1} &= \frac{2L}{S} = 2 \\
G_{3\rightarrow 2} &= \frac{3L}{2S} = 1.5 \\
G_{4\rightarrow 3} &= \frac{5L}{3S} = 1.666... \\
G_{5\rightarrow 4} &= \frac{8L}{5S} = 1.6
\end{aligned}$$

where $G_{i\rightarrow j}$ notes the ratio of consecutive generations of the Fibonacci sequence, so that $G_{2\rightarrow 1}$ refers to the sum of L segments across the first and second generations divided by the sum of S segments across the same generations, and so on. The ratio of these summed segments tends towards τ, indicating that the ratio of the total number of L and S segments in each subsequent generation of the chain are ‘τ–scaled’.

Cut–and–project and Section methods

Another way of producing the Fibonacci sequence, which can be extended beyond $n >$ 3D space, is the cut–and–project method, Figure 2.2(a). Here we start with a 2–dimensional

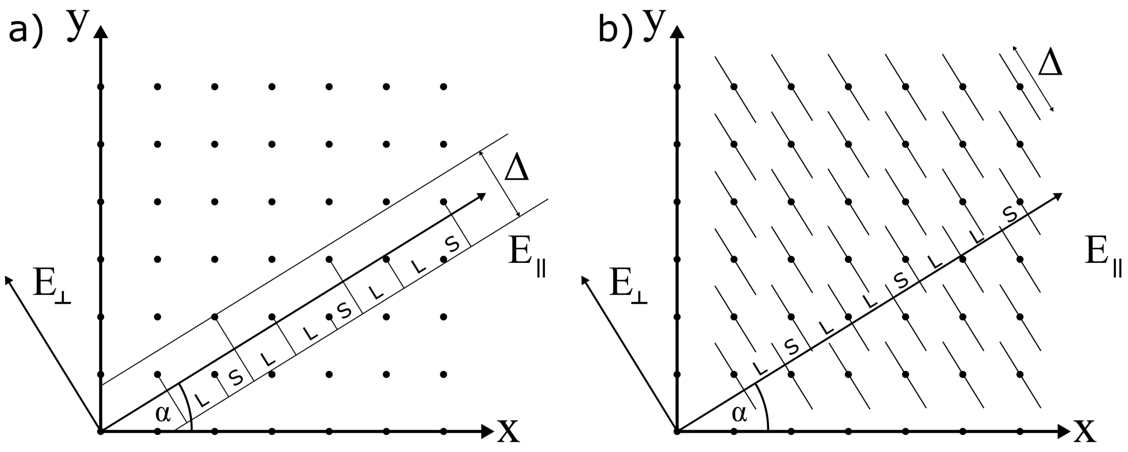

Figure 2.2: **Cut–and–project method:** **(a)** A periodic 2D lattice defined along two orthogonal axes is intersected by a 1D slice, which is rotated with respect to **x** by an irrational angle α. An acceptance window is attached to the slice. E$_{||}$ and E$_\perp$ are subspaces orthonormal to the lattice. Points of the lattice which fall within the acceptance window are projected perpendicularly down onto E$_{||}$, forming a Fibonacci sequence. **(b)** The section method, where atomic surfaces decorate the lattice. A 1D slice rotated with respect to **x** by an irrational angle α intersects specific surfaces to create a Fibonacci sequence.

periodic array of points defined by orthogonal vectors x and y, and a lattice constant of a. The density of points is given by:

$$\rho(x,y)=\sum_{n,m}\delta(x-na)\delta(y-ma) \tag{2.3}$$

where n and m are integers. A second set of orthogonal axes labelled as E$_{||}$ and E$_\perp$ is then rotated around the origin of the original axes by an irrational angle α. In this case, cot$\alpha=\tau$. E$_{||}$ is known as parallel or physical space, whilst E$_\perp$, is perpendicular space. A 1D slice cuts through the periodic array parallel to E$_{||}$. An 'acceptance window' is then attached to this slice, with a width of $\Delta = a$(cos α+ sin α). 'Accepted' points of the 2D lattice within this window are then projected onto E$_{||}$, creating segments of either $S=a$sinα, or $L=a$cos α. These segments are spaced in a Fibonacci sequence.

Likewise, shown in Figure 2.2(b), is the section method. The same formalism as the cut and project method is used, except here, atomic 'surfaces' decorate each of the lattice points, which are oriented perpendicular to E$_{||}$. Their width is also Δ. The 1D slice parallel to E$_{||}$ intersects specific surfaces, creating sections of the Fibonacci chain.

2.2.2 Diffraction from a Fibonacci chain

To show if any system of points exhibits long–range order, we can calculate its diffraction pattern. The diffraction pattern or Fourier transform of a 1D Fibonacci sequence has been derived and described elsewhere [2, 18–21]. Thus, only the pertinent results will be given here. The Fibonacci sequence components produced using the cut–and–project method will be used here.

To produce the diffraction pattern of the 1D chain, we calculate the Fourier transforms of the accepted points of the lattice within the window in Figure 2.2(a). The transform of the infinite lattice is simply a reciprocal lattice defined by a vector $\mathrm{Q}_{hh'}$, where h, h' are the Miller indices. $\mathrm{Q}_{hh'}$ can then be decomposed into perpendicular and parallel space components ($\mathrm{Q}_{\perp}$ and $\mathrm{Q}_{||}$ respectively). The Fourier components of the accepted points are produced by a convolution of this reciprocal lattice and the Fourier transform of the window function (i.e. a function which is 1 inside the window, and 0 outside). This produces Fourier components which are then centred at the vertices of the reciprocal lattice. These components are intersected by an irrational slope $\mathrm{E}_{||}{}^*$ (which is parallel to $\mathrm{E}_{||}$), producing Bragg peaks at positions given by [20]:

$$Q_{||} = \frac{2\pi}{a} \frac{1}{(2+\tau)^{\frac{1}{2}}} (h + h'\tau) \tag{2.4}$$

We know intuitively from Figure 2.2 that these intersections will also be quasiperiodically arranged in 1D reciprocal space.

It can be shown analytically that the intensity of the Bragg peak at each $\mathrm{Q}_{||}$ intersection is dependent on $\mathrm{Q}_{\perp}$ [18, 20]:

$$Q_{\perp} = \frac{2\pi}{a} \frac{1}{(2+\tau)^{\frac{1}{2}}} (h - h'\tau) \tag{2.5}$$

by

$$I_{hh'} = \Delta^2 \frac{\sin^2(Q_{\perp}^{hh'})\Delta/2}{(Q_{\perp}^{hh'}\Delta/2)^2} \tag{2.6}$$

It can be seen that values of $\mathrm{Q}_{\perp} \rightarrow 0$ give maximal intensity. In fact, as a and τ are constants, we can see from equation (2.5) that $\mathrm{Q}_{\perp}$ is at its smallest when $(h – h'\tau) \approx 0$, or, when $\frac{h}{h'} \approx \tau$. The consequence of this is that sharp Bragg peaks of maximum intensity

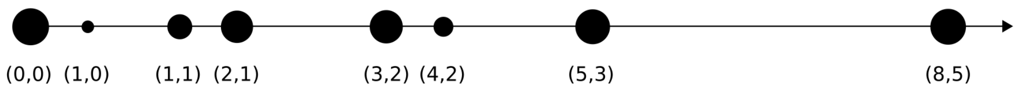

Figure 2.3: **Diffraction of a Fibonacci chain.** Selected Bragg spots with radii scaled with intensity are shown for the calculated diffraction pattern of a 1D Fibonacci sequence. Indices refer to Miller indices (h,h').

come from values of (h,h') that are successive integers in the Fibonacci series, i.e. (5,3), (8,5) etc., shown in Figure 2.3, which displays a few calculated Bragg peaks for certain (h,h').

The demonstration that an aperiodic set of points can display a discrete diffraction pattern is a powerful one, and can be used reliably as a model for explaining how aperiodic systems with higher dimensionality display long–range order. This information is vital for understanding the basics of quasicrystalline structure.

2.2.3 Aperiodicity in 2D

The Fibonacci chain is useful as a model QC system for calculating properties of 1D QCs [22–26]. However, it has no rotational symmetry. We can show how systems can exhibit long–range aperiodic order and also display orders of rotational symmetry not explained by pre–quasicrystalline crystallography by looking at several 2–dimensional examples. These quasiperiodic systems are known as 'tilings'.

Aperiodic tilings can fill all space, with no gaps, using a set of proto–tiles (building blocks). The resultant arrangement has long–range order, yet no translational symmetry. Examples of tilings which exhibit 5–, 8–, and 12–fold symmetry are shown in Figure 2.4 – known as the Penrose (P1), Watanabe–Soma–Ito, and the Stamplfi–Gaehler tilings respectively [27–30]. The constituent proto–tiles of each are shown below the tilings.

Tilings can be constructed in a number of ways. The substitution method simply replaces one proto–tile with a set of smaller proto–tiles, analogous to S and L substitutions. Matching rules can also be used – where the edges of a set of proto–tiles follow rules which

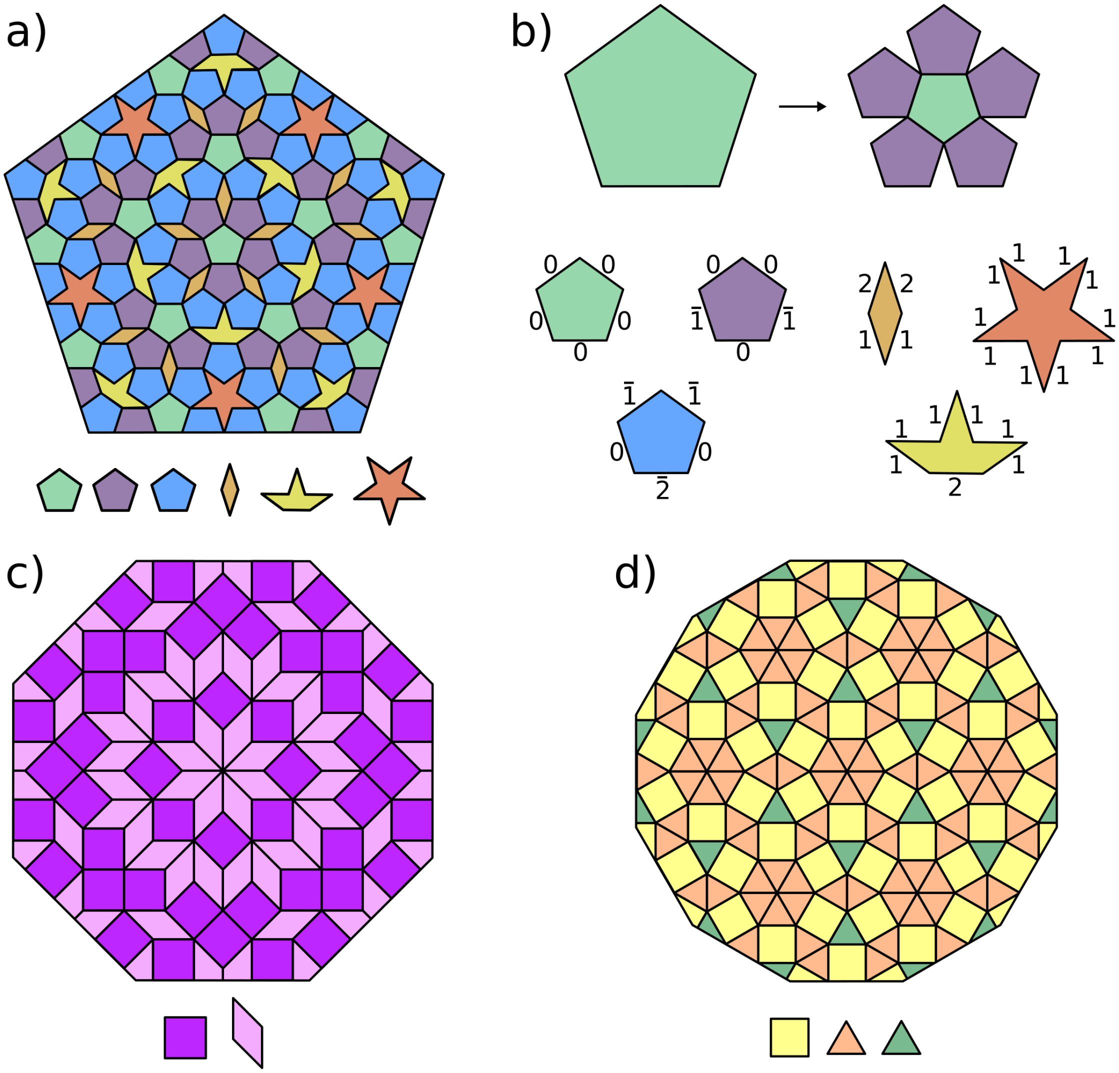

Figure 2.4: **Aperiodic tilings with $n \geq 5$–fold rotational symmetry.** **(a)** The Penrose P1 tiling, which exhibits 5–fold symmetry. **(b)** An example of substitution rules for deflating the Penrose tiling. Matching rules of the constituent tiles are shown. **(c)** The Watanabe–Soma–Ito tiling, which exhibits 8–fold symmetry. **(d)** The Stamplfi–Gaehler tiling, which exhibits 12–fold symmetry.

only allow specific pairings of tiles. Figure 2.4(b) demonstrates the substitution method and tile matching rules for creating the Penrose P1 tiling. Here, the rules allow sides with equal integers yet with unequal parities to be matched, where rotations of the tiles are necessary to fill the plane. Other methods for tiling production and a more detailed discussion on tilings in general can be found in Chapter 6.

The Penrose tiling is particularly useful, as the most common type of quasicrystal exhibits icosahedral symmetries. N. G. de Bruijn used the cut–and–project method – projecting from a 5D cubic structure onto a 2D plane – to predict the Penrose structure across all space [31]. His work thus allows explicit calculations of quasicrystalline structure [32]. It is also an excellent example of using higher–dimensional mathematics to understand aperiodic structure, such as that used to create the 1D Fibonacci sequence.

Additionally, an important tiling used in this thesis is the Fibonacci square grid. Its construction will be detailed in Chapter 5, but for now, it is sufficient to say that it is built by two sets of overlapping orthogonal Fibonacci chains. It has 4–fold symmetry, and its relative structural simplicity compared to the tilings in Figure 2.4 make it attractive for experimental and theoretical exploration. A 3–fold aperiodic tiling can be constructed in a similar fashion, which is detailed in Chapter 6.

2.3 Icosahedral symmetry

The majority of intermetallic QC phases have icosahedral symmetry [4]. As this thesis concerns experimental measurements concerning icosahedral quasicrystals (iQCs), their structure and formalism will be considered here. The icosahedron is one of the five Platonic solids, formed of twenty identical triangular faces. It contains six 5–fold, ten 3–fold, and fifteen 2–fold rotational axes. An icosahedron decorated with an atom at each vertex and an additional central atom has a packing factor of 0.76, greater than hexagonally closed packed (hcp) systems (0.74). However, unlike hcp–based structure, icosahedra are incompatible as periodic unit cells, i.e. they lack translational symmetry in any direction. Thus iQCs are aperiodic in all 3 dimensions.

Figure 2.5 shows six reciprocal space vectors which define the vertices of an icosahedron. These vectors are used to index icosahedral diffraction patterns. They can be projected along any of the high symmetry axes to index the relative rotational orientation of a QC, as shown. They are labelled as $\mathbf{a}_1 = \mathbf{a}(0,0,1)$, $\mathbf{a}_j = \mathbf{a}(\sin\theta\cos 2\pi j/5,\ \sin\theta\sin 2\pi j/5,\ \cos\theta)$ where j=2,...,6, and $\tan\theta = 2$. The vectors ($\mathbf{a}_{1-6}$) can also be labelled using generalised

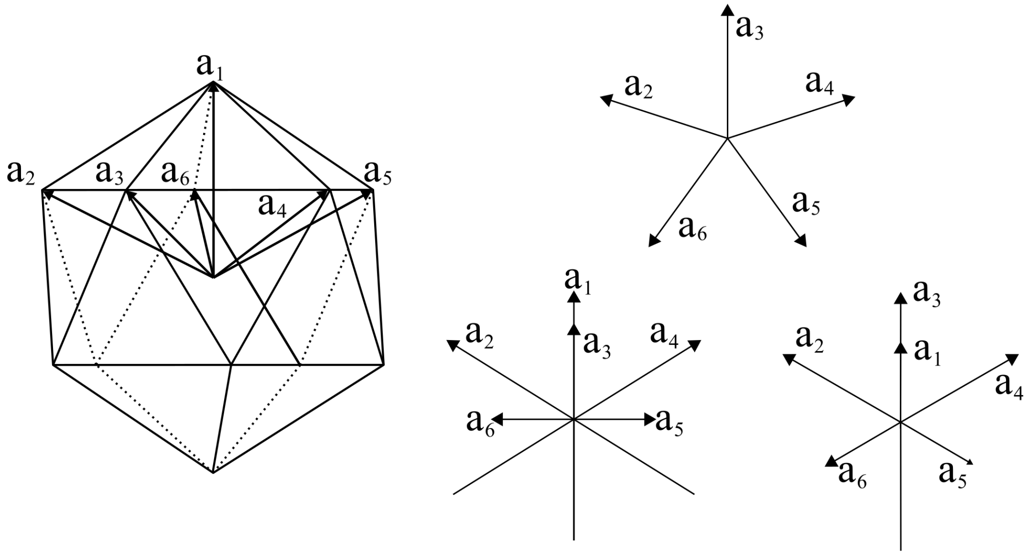

Figure 2.5: **Icosahedral reciprocal vectors:** **(a)** The six vectors required to construct an icosahedron in reciprocal space are labelled $a_{1\ldots6}$. **(b)** Clockwise, from top: the projection of the vectors in **(a)** along one of the 5–fold, 3–fold, and 2–fold symmetric axes.

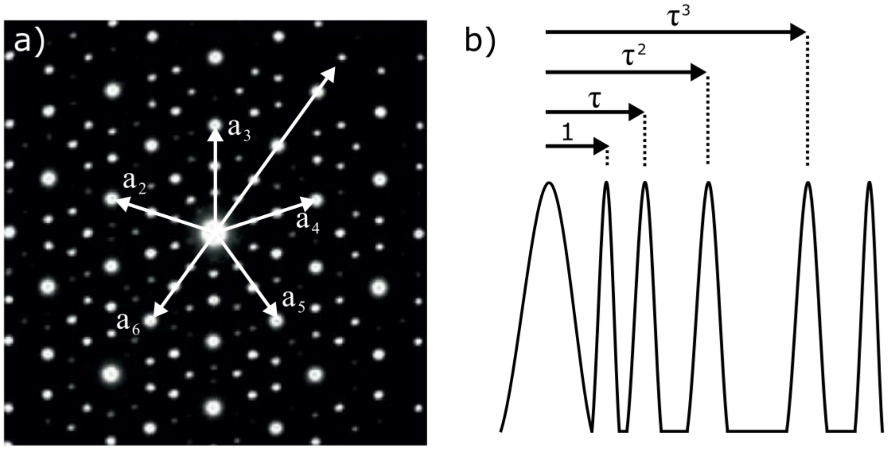

Figure 2.6: **Icosahedral indexing:** **(a)** Diffraction pattern obtained from the quasicrystalline phase of Al–Mn. The pattern is indexed with respect to the icosahedral vectors in Figure (2.5). Reproduced from [1]. **(b)** Line profile of the non–indexed vector in **(a)**. The profile shows τ–scaled spots of high intensity, as predicted by Figure (2.3).

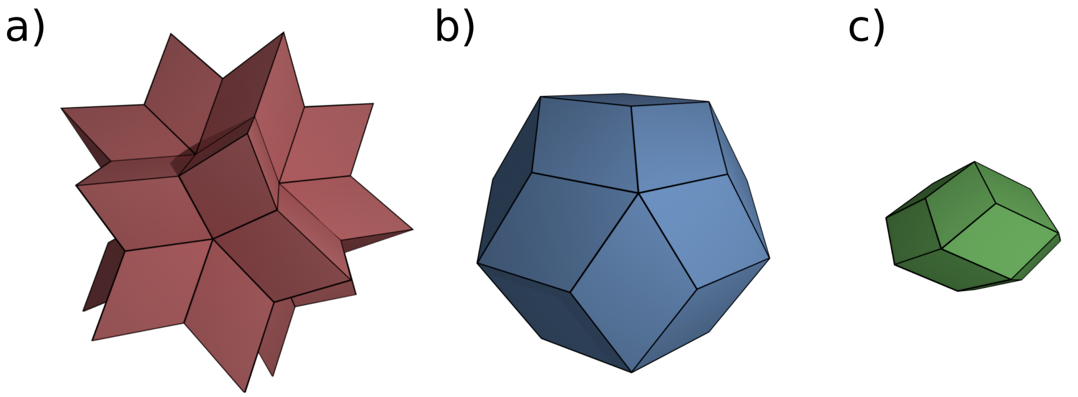

Figure 2.7: **Occupation domain building blocks:** **(a)** Rhombic hexacontahedron (or dodecahedral star). **(b)** Rhombic triacontahedron **(c)** Rhombic icosahedron.

Miller indices as: [100000], [010000], [001000], [000100], [000010], [000001] [5].

Figure 2.6 indexes the original Al–Mn diffraction pattern observed by Shechtman [1]. Here, a_1, the 5–fold direction, is perpendicular to the page. The pattern appears 10–fold due to inversion symmetry. A line profile along one of the high symmetry axes produces a set of Bragg peaks analogous to the 1D diffraction pattern in Figure 2.3.

2.3.1 Higher–dimensional crystallography

Periodic crystals are defined in reciprocal space by a lattice with three basis vectors i.e., their dimensional rank $n = 3$. The notion that iQC diffraction patterns are indexed with six reciprocal space vectors confirms that icosahedral symmetry is incompatible with periodic order in 3D. It also infers that their structure is embedded in a periodic, higher dimensional lattice of rank $n = 6$. Indeed, icosahedral structures can be produced by a cut and projection from an abstract 6–dimensional hypercube [4, 6, 20, 33, 34]. Here, analogous to the projection method of the Fibonacci sequence, acceptance windows (often called 'occupation domains', or ODs), are decorated with atoms and placed at high symmetry 6D lattice points. When the lattice is cut along an irrational slope and projected to 3D space, the intersection of slope and occupation domain produces a 3–dimensional quasilattice with icosahedral symmetry. Three types of quasilattice exist (primitive, body–centred, face–centred), dependent on the type of periodic hyper–lattice used [35].

The structure factor of a quasicrystal can be calculated by the Fourier transform of these occupation domains, so careful calculation of its geometry is important [34]. Early calculations considering spherical ODs for iQCs gave a rough atomic model of the quasicrystal structure for, e.g. i–Al–Pd–Mn [36]. However, this method often caused unphysically short atomic distances, and so, a polyhedral shape was considered for ODs. In the case of iQCs, it is important to describe ODs with building blocks that exhibit icosahedral symmetry in order to describe an icosahedral system [37]. Using i–Al–Pd–Mn as an example again, Yamamoto et al. calculated that ODs could be constructed using three icosahedral building units, the dodecahedral star, rhombic icosahedron, and rhombic triacontahedron that then decorated a 3D Penrose tiling, Figure 2.7 [37].

2.4 Cluster model

The use of hyper–dimensional maths to create quasilattices which exhibit icosahedral symmetry under diffraction is a crucial step towards understanding the structure of iQCs. However, simply indexing the diffraction patterns of these quasilattices or real QCs does not tell us the precise atomic structure of a QC, or, where the atoms are. We can use a simple example to illustrate. If we consider a Penrose P3 tiling (or any aperiodic tiling), it is locally isomorphic i.e. it can be shown that finite patches of an infinite aperiodic tiling are identical. (Note: this is not the same as translational symmetry). Considering this, we see that three structurally different areas of a Penrose P3 tiling, which share locally isomorphic patches, produce three essentially identical diffraction patterns due to their similar structure factors, Figure 2.8 [38, 39]. Conversely, this infers that any number of precise but unique structures can be obtained from QC diffraction patterns.

2.4.1 Approximants

A route that has proven fruitful for understanding QC structure is to look to intermetallics that closely approximate quasicrystals, known as approximants, whose structures can be unambiguously solved. There are a few factors for this motivation. First, obtaining a phase of matter which offers a periodic ‘cousin’ to an aperiodic material has obvious mathematical and modelling advantages. Second, the chemical composition of approximants and QCs are typically close, leading to similar physical properties [40]. In fact, approximants have been described as ‘the missing link between quasicrystals and periodic crystals’ [40]. Structural refinement can thus be achieved by close comparison of known approximant structures to

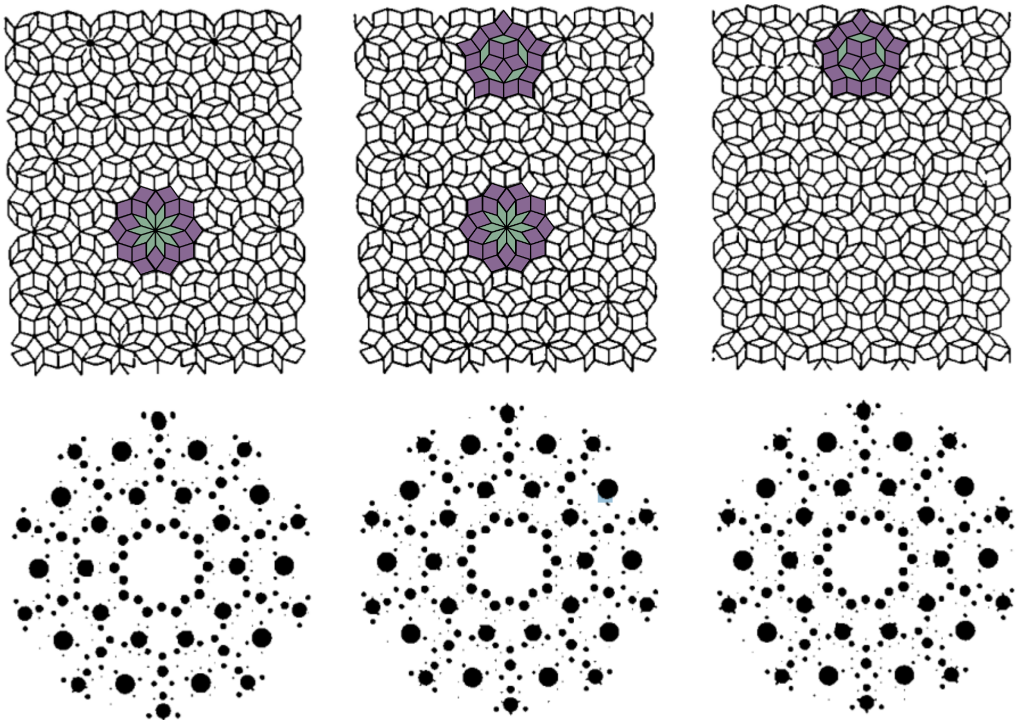

Figure 2.8: **Locally isomorphic Penrose tilings:** *Top:* Three structurally distinct patches of the Penrose P3 tiling. Highlighted are common motifs. *Bottom:* Diffraction patterns from each patch, which are essentially identical. Reproduced and modified from [34].

model QC structures.

On a general note, approximant structure (or indeed, any periodic structure) can be modelled using higher–dimensional crystallography, by cutting through a 6D lattice by a rational slope. We can decorate the 6D lattice with ODs to match the experimentally observed approximant structure, and then make comparisons to the QC partner. Thus, refinements of the approximant OD can lead to better models of the QC OD. Returning to the 2D analogy in creating the Fibonacci sequence using the cut and project method in Figure 2.2, if our angle of intersection is such that cot $\alpha = 2$, we create a periodic chain of *LLS* sections (a 2/1 ratio of L to S). As the slope is tilted towards cot $\alpha = \tau$, we find longer and longer repeatable units of approximation e.g. *LLSLS*, *LLSLLSLS* ($\frac{L}{S}$ ratios of 3/2, 5/3 etc.) [4]. Approximants are categorised by these ratios, where higher order Fibonacci ratios more closely represent true QC structure.

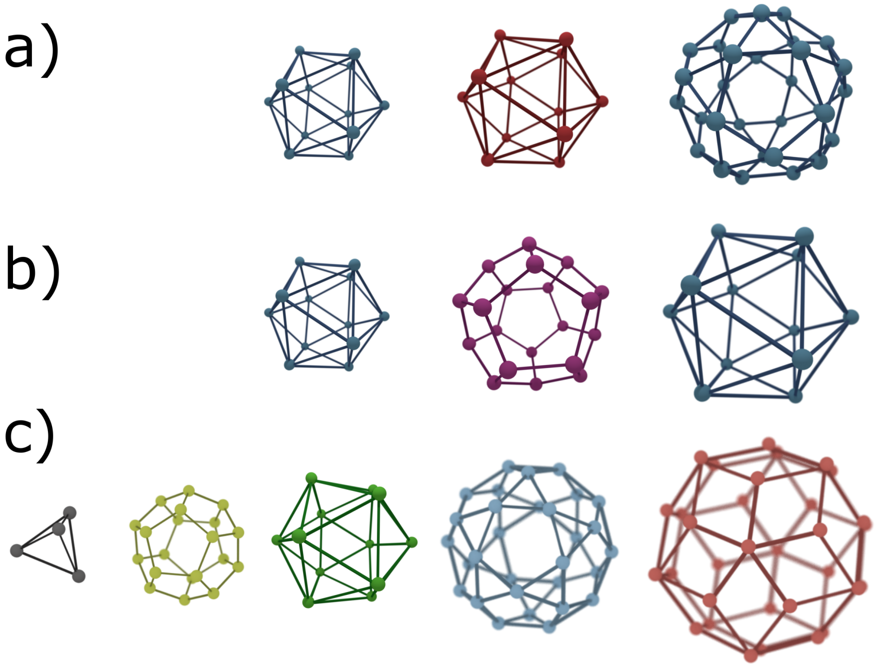

Figure 2.9: **Clusters:** **(a)** Mackay cluster: first shell is an Al/Si icosahedron. Second shell is a Mn icosahedron. Third shell is an Al/Si icosidodecahedron. **(b)** Bergman cluster: first shell is an Al/Cu icosahedron. Second shell is a Li dodecahedron. Third shell is an Al/Cu icosahedron. **(c)** Tsai cluster: first shell is a Cd tetrahedron. Second shell is a Cd dodecahedron. Third shell is an Yb icosahedron. Fourth shell is a Cd icosidodecahedron. Fifth shell is a Cd rhombic triacontahedron.

On a specific note, we can take the α(Al–Mn–Si) approximant as an example of the relationship between approximants and quasicrystals. Here α refers to one of the two structures observed in this phase. Cooper and Robinson used diffraction and calculation of atomic structure factors to understand the α(Al–Mn–Si) system, concluding that the unit cell contained 138 atoms, arranged in ‘different coordination polyhedra’ [41]. These polyhedra were identified as 54–atom Mackay clusters which were attached by Al octohedra [40, 42]. The Mackay cluster is a hierarchical system of concentric atomic shells, packing space densely in an icosahedral fashion [43]. It is constructed by an Al icosahedron, a Mn icosahedron, and an Al/Si icosidodecahedron, Figure 2.9(a). After quasicrystals were discovered, the α(Al–Mn–Si) structural system was found to approximate the i–Al–Pd–Mn QC [42]. This gives the indication that Mackay clusters play a role in the i–Al–Pd–Mn

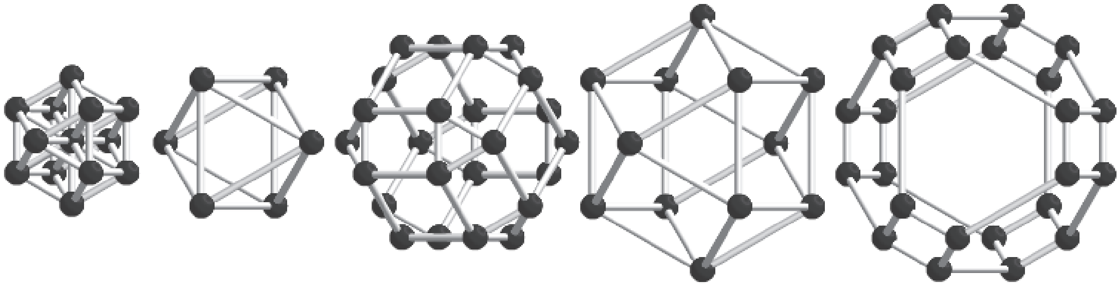

Figure 2.10: **Coordination polyhedra in face–centre aluminium:** The range of polyhedra found around a single Al atom in face–centred Al. Reproduced from [46].

QC structure.

In general then, clusters can be used to understand both quasicrystal and approximant structure. For icosahedral approximants, we can use Mackay, Bergman, and Tsai–types [6, 43, 44], whose geometries are shown in Figure 2.9. The three cluster systems are also known as the Al–Mn–Si, Zn–Mg–Al, or the Cd–Yb classes respectively, in relation to the approximant/QC system type they help to classify. Within this thesis, two types of quasicrystal have been used, differentiated not only by their constituents, but also by their structure type. For example, *i*–Al–Pd–Mn can be modelled using a pseudo–Mackay cluster, whilst *i*–Ag–In–Yb is isostructural to the Cd–Yb cluster model. Both types of these cluster models will be discussed in greater depth within the next section.

2.4.2 Clusters in iQCs

Although clusters build approximant structure, it does not necessarily prove their stability within intermetallic quasicrystals. In fact, the existence of a cluster-based QC system is still debated, where even the definition of a 'cluster' in a QC is questioned [45,46]. Whether clusters are purely geometrical or have structural stability, and whether adjacent clusters can overlap are contested, open questions [47]. Certainly, there is an argument against arbitrary geometric constructions i.e., creating atom–decorated polyhedra in the bulk and assigning them as 'clusters'. An excellent example is the coordination polyhedra which can be formed around any Al atom in face–centred aluminium, shown in Figure 2.10 [46]. Ideally, these clusters should have some chemical or electronic stability. However, it is certainly true that conceptualizing clusters as building blocks when analysing QC structure is important and useful.

Nevertheless, at this stage, we can describe iQC structure using one of the three cluster–types as a basis centred at the vertices of a quasilattice projected from 6D space [45]. A good example is the Cd–Yb cluster system, the first stable binary quasicrystal. The projected structure from the approximant and QC occupation domains fits excellently, and its relative lack of chemical complexity allows for a more precise model than ternary or quaternary QCs, as there is a distinct difference in where each atom type lies based on structure factor/electron density calculations [6].

2.5 Icosahedral quasicrystal surfaces

No known icosahedral quasicrystal surface (or for that matter, related approximant) has a surface reconstruction [5]. As such, we can investigate energetically stable 2D cross sections of a QC using a variety of surface–sensitive techniques. This can assist with the confirmation/refinement of structural models: whilst the surfaces of QCs have been investigated due to their advantageous macroscopic properties (such as low friction, high hardness, and catalytic activity [15, 48, 49]), microscopic studies offer an interesting structural foil to the higher–dimensional methods. The 5–fold surfaces of the *i*–Al–Pd–Mn and *i*–Ag–In–Yb systems will be discussed here, as these QCs are relevant for this thesis.

A large body of work has concentrated on 5–fold iQC surfaces. The motivations are two–fold. First, in general, these orientations are the most energetically stable – producing atomically flat terraces when sputtered and annealed with little to no surface corrugation [5]. Second, they are attractive because of their unusual symmetry. The corollary is that the 2–fold and 3–fold iQC surfaces are less well explored.

2.5.1 5–fold Al–Pd–Mn

The bulk structure of *i*–Al–Pd–Mn can be described by pseudo–Mackay clusters which decorate a 3D quasilattice originating from a face–centred hypercube [36]. Here, the inner icosahedron of a Mackay cluster is replaced by a partially occupied dodecahedron, and a central atom [50]. Refinements to this model include an interpenetrating pseudo–Mackay/ Bergman cluster, and ‘two types of icosahedral clusters and two types [of]...Mackay–type clusters’ [5,37,51,52]. A side–view of a pseudo–Mackay cluster is shown in Figure 2.12. Blue atoms are Al, yellow are Pd, and red are Mn. The positions of the inner Mn dodecahedron have been randomly removed to give only 7 atoms.

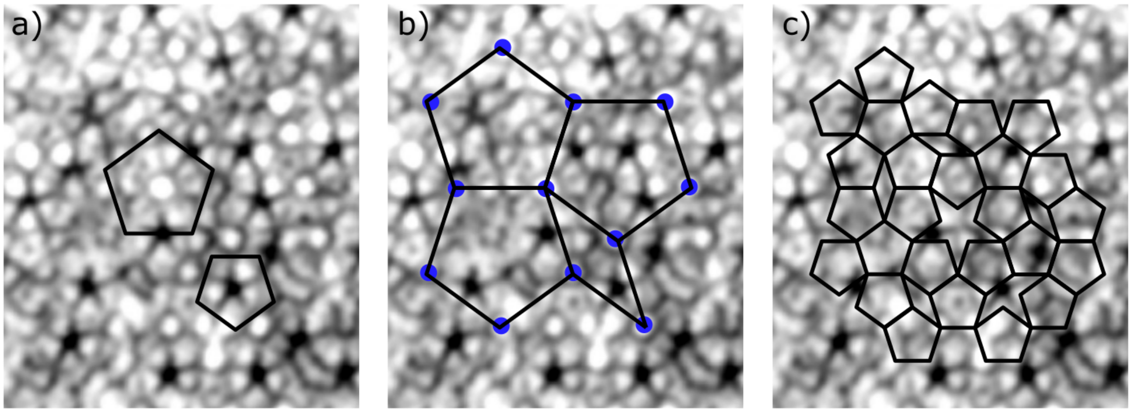

Figure 2.11: **5–fold Al–Pd–Mn surface:** **(a)** STM image (10×8.7 nm^2) of the 5–fold Al–Pd–Mn surface. A white flower and dark star are highlighted by two pentagons. **(b)** A patch of the P1 Penrose tiling is overlaid on **(a)** linking white flower centres, highlighted by blue circles. **(c)** Deflated tiling from **(b)** (edge length = 7.8 Å) links bright features. Reproduced and modified from [53].

LEED and helium atom scattering (HAS) analysis indicated that after sputtering and annealing, the surface perpendicular to the 5–fold orientation is atomically flat and exhibits 5–fold symmetry [5, 18, 54–56]. Likewise, comparisons of bulk reciprocal vectors and surface–projected reciprocal vectors using x–ray diffraction (XRD) and HAS showed that the surface is bulk truncated, with no reconstruction observed [5]. STM likewise indicated an atomically flat surface, with a step–terrace morphology. Here, steps form Fibonacci sequences with two heights, S and L [57–59]. Atomically resolved STM showed features described as 'white flowers' and 'dark stars' which are linked to the truncations of pseudo–Mackay/Bergman clusters [53]. The white flowers have been determined as intersections of pseudo–Mackay clusters with a central Mn atom. The specific nature of the dark stars is disputed dependent on the bulk model, with the most recent interpretation being that they are produced by intersected Mackay clusters at a different height to the white stars [60, 61]. The centres of pseudo–Mackay clusters can be connected by a Penrose P1 tiling of τ^2×7.8 Å, with a deflated tiling of edge length of 7.8 Å linking other bright features (Figures 2.11(b, c) respectively).

A calculation based on a bulk model of pseudo–Mackay/Bergman clusters gives a surface structure which can also be characterized by a P1 tiling of 7.76 Å, where tiling vertices intersect truncated Bergman clusters [62]. These calculations also predicted the white

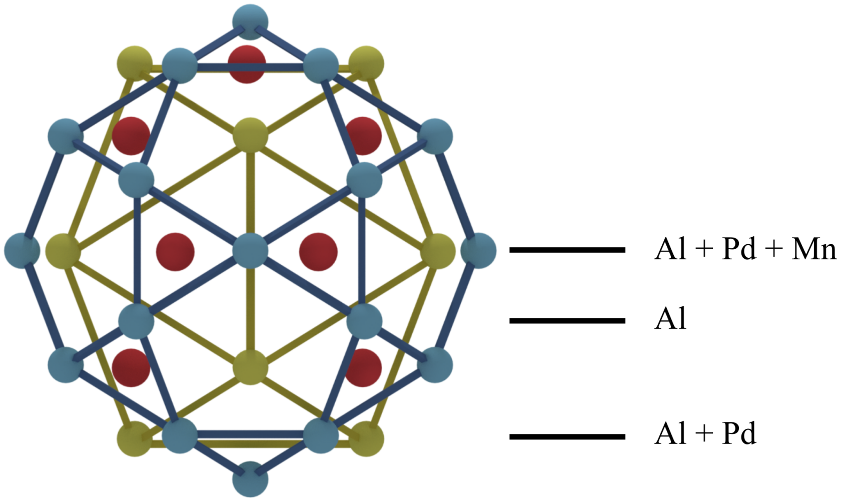

Figure 2.12: **Cluster and plane model:** A side view of a pseudo–Mackay cluster shows how atomically flat surfaces are produced. Three planes with their constituents are highlighted.

flower and dark star structures, indicating that Al and Mn appear as brighter spots with STM [62]. Here, the white flowers were also attributed to truncated Mackay clusters, whilst the dark stars were deemed to be either truncated Bergman clusters, or surface vacancies. Comparisons between these STM studies, dynamical LEED, and the refined structure model [52,54,63] indicated the topmost surface layers are Al–rich, containing no Pd.

The planar structure observed by these surface–sensitive techniques may seem at odds to the proposed cluster model. However, consider the side–view of a pseudo–Mackay cluster, Figure 2.12. Here, we are viewing perpendicular to the 5–fold orientation, i.e. along the surface. We observe planes of varying density depending on their constituents i.e. mixed planes of Al, Pd, Mn. The comparison between STM step–heights, LEED, and the bulk model led to an agreement on how atomically flat planes could be observed at a cluster–based bulk–truncated surface. However, Ebert et al. also explored a cleaved *i*–Al–Pd–Mn surface, with no sputter–anneal treatment. Here, they observed rough protrusions with separations consistent with a Mackay cluster–model [64]. A lack of intra–cluster resolution has left these results open to differing interpretations.

2.5.2 5–fold Ag–In–Yb

Icosahedral Ag–In–Yb is isostructural to i–Cd–Yb, with Ag–In replacing Cd in equal parts [65]. The advantage of studying the i–Cd–Yb system is the high level of structural detail obtained from the cluster model [6]. However, the high vapour pressure of Cd makes i–Cd–Yb unsuitable for study in ultra high vacuum (UHV). Although the specificity of the chemical sites are lost (i.e. positions of Ag–In atoms in the Cd shells contained within the Cd–Yb cluster), i–Ag–In–Yb is suitable for surface study under vacuum.

X–ray photoelectron spectroscopy (XPS) showed that after annealing, the 5–fold Ag–In–Yb surface retained its bulk chemical composition [65]. STM revealed a step–terrace structure, again with L and S steps [66]. However, these steps do not directly follow a Fibonacci sequence. Rather, it can be shown (along the 3–fold axis) that groups of steps are expected to follow a Fibonacci sequence, whereby, for example, $(3L + 2S)/(S + 2L)$ gives τ. Occasionally, less preferred medium M steps were observed, where $L \sim M + S$.

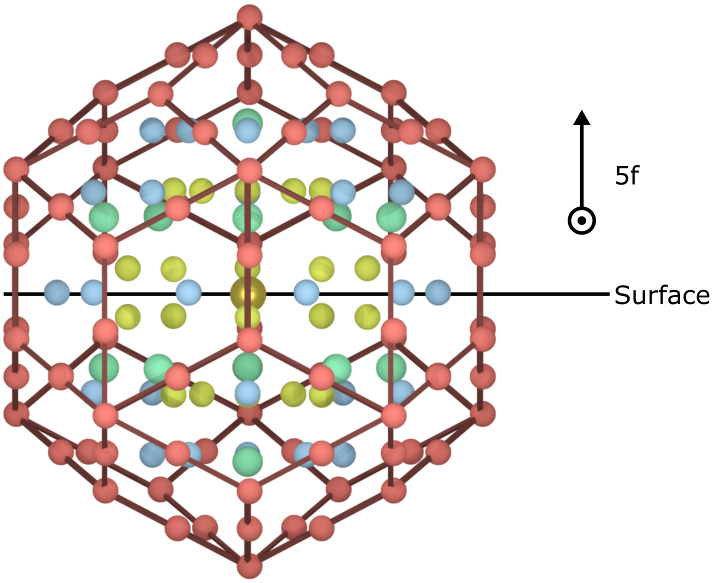

Figure 2.13: **Cd–Yb cluster:** A side–view of the Cd–Yb cluster oriented along one of its 5–fold axes. Each shell is shown with the exception of the 1st. The atoms of each shell are coloured, and the colour scheme used here is consistent through this thesis. The 2nd is yellow, the 3rd green, the 4th blue, and the 5th red. A golden atom is the cluster centre. Labelled is the surface plane. The sticks of the 5th are shown only, for clarity.

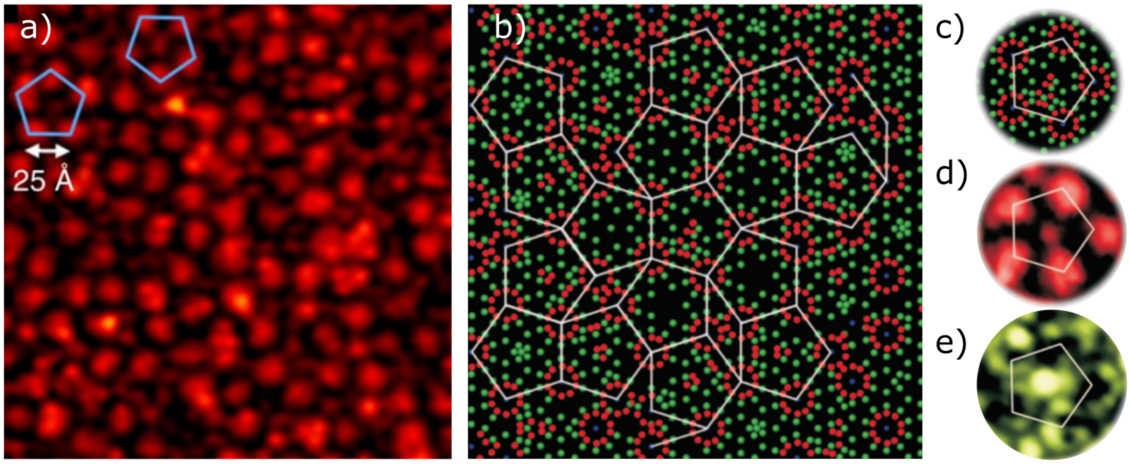

Figure 2.14: **5–fold Ag–In–Yb surface:** **(a)** STM image (30×30 nm^2) of the 5–fold Ag–In–Yb surface. Highlighted are pentagons surrounding cluster centres predicted by the Cd–Yb model. **(b)** Model of the Cd–Yb system, where green circles are Yb atoms, red circles are Cd, and blue circles are the cluster centres. A Penrose P1 tiling of edge length 2.5 nm is overlaid. **(c)** Model schematic of one of the pentagons observed in **(a)**. **(d)** Negative bias STM image of feature **(c)**, showing Ag/In sites. **(e)** Positive bias STM image of feature **(c)**, showing Yb sites. **(a)** reproduced from [67]. **(b–e)** reproduced from [66].

As previously discussed, Cd–Yb clusters are formed by tetrahedron, dodecahedron, icosahedron, icosidodecahedron, and rhombic triacontahedron shells, referred to as the 1st, 2nd, 3rd, 4th, and 5th shells respectively. Figure 2.13 shows a side view of a Cd–Yb cluster, where each shell is coloured separately. The 1st shell (the tetrahedron) is omitted as it is often not included in surface models, expanded upon in Chapter 7. The cluster centre is marked as a golden atom. The 5–fold *i*–Ag–In–Yb surface was found to truncate high–density regions of the Cd–Yb bulk model, which intersected the centres of the clusters, producing flat planes of atoms analogous to Figure 2.12, highlighted in Figure 2.13 [66]. Chapter 7, Figure 7.2, shows an example of how clusters in 3 dimensions produce a surface plane with different shell constituents.

The surface structure of the 5–fold Ag–In–Yb orientation was therefore found to be dependent on the Yb icosahedron and Ag/In icosidodecahedron shells, with rings of Yb and Ag/In atoms forming pentagonal motifs, shown in Figure 2.14. At a negative tip bias (occupied sample states), Ag/In is resolved, whilst positive bias (unoccupied sam-

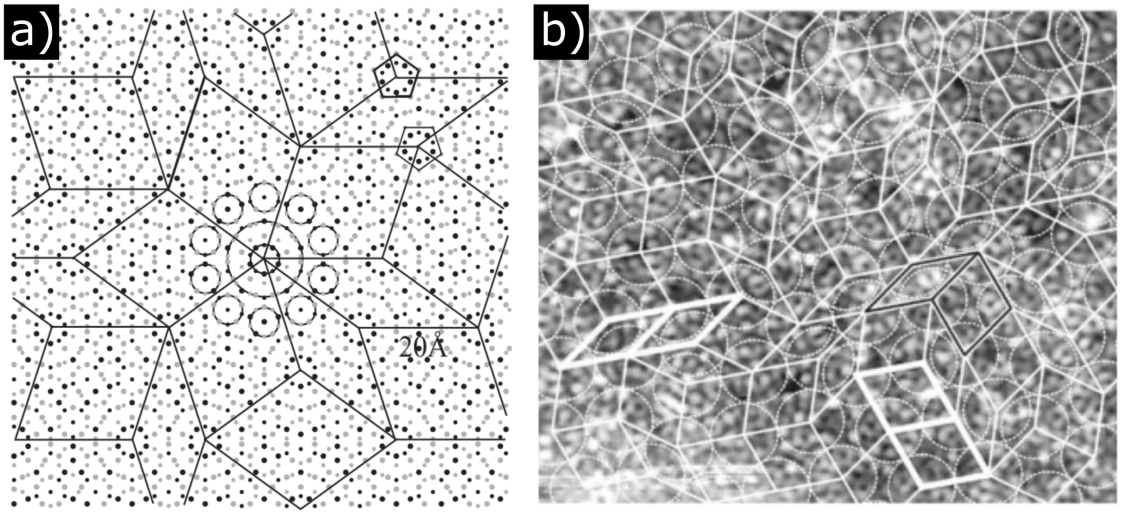

Figure 2.15: **Decagonal QC surface:** **(a)** Model of two decagonal QC planes. Grey circles are Al atoms, black, transition metal. Larger circles are in the surface plane, smaller are in the plane below. A rhombus tiling links cluster centres together. **(b)** STM image of the 10–fold d–Al–Ni–Co surface. Cluster centres are linked by a Penrose P3 tiling. Defects in the tiling are highlighted in bold white. Reproduced and modified from [5].

ple states) resolves Yb. These findings are consistent with theoretical calculations which show that unoccupied states of Cd–Yb are dominated by Yb–5d levels [66, 68]. Similar to *i*–Al–Pd–Mn, a Penrose P1 tiling can be overlaid on the substrate, with an edge length of 2.4 nm. Here, the tiling was shown to explicitly intersect cluster centres.

2.5.3 Decagonal quasicrystals

Although not relevant for this thesis, a short summary of decagonal quasicrystals (dQCs) and an example surface will be given for completeness. Unlike iQCs, decagonal quasicrystals are not aperiodic in all directions. Rather, they can be considered as a set of quasicrystalline planes stacked along a 10–fold rotational axis. The separation of these planes along the QC's 2–fold axis is periodic [5]. The much–studied d–Al–Ni–Co phase will be discussed here.

The d–Al–Ni–Co quasicrystal is found in a variety of phases, either Ni or Co rich [5]. Each of these phases are structurally similar, however, not identical. They can be considered to be composed of columnar 'clusters' of stacks of quasicrystalline planes, roughly

20 Å in diameter [69, 70]. Dependent on the phase, these clusters can be matched to the vertices of a rhombic Penrose tiling (in a phase known as the type I superstructure), or a pentagonal tiling (Co–rich phases). Each plane in the stack has 5–fold symmetry, with neighbouring planes rotated by 36° to each other, producing 10–fold symmetry overall. As with the icosahedral quasicrystals discussed, the 10–fold surface of d–Al–Ni–Co exhibits no reconstruction, although a dynamical LEED study showed a slight vertical relaxation [71].

Figure 2.15(a) shows a model of the 10–fold d–Al–Ni–Co surface plane. Here, two quasicrystalline planes are superimposed to give 10–fold symmetry. Grey circles are Al, black circles are the transition metals. These black positions are filled specifically by Ni or Co dependent on the phase. The centres of columnar clusters are linked with a Penrose P3 tiling. Figure 2.15(b) shows an STM image from the 10–fold d–Al–Ni–Co surface. Clusters are circled, and are linked by a Penrose P3 tiling. Bold tiles indicate patches which break the ideal Penrose tiling, suggesting a randomized tiling [5].

Chapter 3

Thin film growth on quasicrystals

Thin film growth has a wide range of uses, with applications in optics, mechanics, electronics, and chemistry. Modern techniques for thin film growth allow close–control of constituents and thus a certain degree of property tunability. Thin film growth in terms of adatom adsorption at surfaces will be discussed here, with a view to looking at epitaxial modes on crystalline and quasicrystalline surfaces. This review will give context to the results presented later in this thesis.

3.1 Adsorption energetics

The surfaces of crystals were first considered as part of an effort to understand crystal growth, with the development of the terrace–step–kink model (TSK) [72, 73]. A substrate contains atoms with reduced nearest neighbour coordination compared to the bulk crystal. Dependent on their position in the TSK model, these atoms may be more or less suitable for seed points – for example, those with low coordination numbers are more viable for initiating nucleation. The TSK model accurately predicted the presence of step–terrace morphology upon crystal surfaces, observed by techniques such as STM.

Upon the creation of a surface from the bulk material, inter–atomic bonds are broken, leading to a surface free energy. It follows that the surface is less energetically favourable than the bulk, with a certain degree of surface tension expected. Adsorption of adatoms (here generalised as atoms or molecules) may reduce the surface free energy. Adsorption is dependent on the flux of the incident atoms, and the sticking coefficient of the surface (i.e. probability an adatom will stay on the surface). Other factors include the temperature of

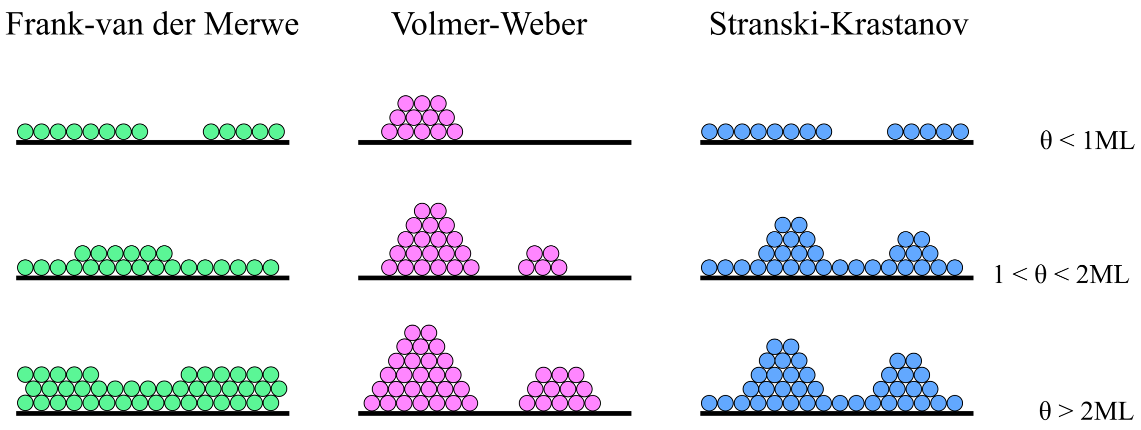

Figure 3.1: **Thin film growth modes:** Frank–van der Merwe (layer–by–layer), Volmer–Weber (island), and Stranski–Krastanov (layer–plus–island) type growth modes shown for a range of coverages.

the substrate, and the chemical affinity between adatom and surface.

If we consider homoepitaxy (i.e. the thin film growth of like–like surface–adtom types), it is easy to consider how surface energy will be decreased, as we are simply simulating crystal growth i.e. replicating layers of the bulk. The structure of a heteroepitaxial film (i.e. unlike surface–adtom types) will depend on how strong the surface–adatom interaction is, and the lattice mismatch between the two species. In either case, a stable thin film can be grown if the surface free energy is decreased when adatoms adsorb. Adsorbates can be bonded to the surface by two mechanisms: either physisorption or chemisorption. Physisorption relies on van der Waals forces, whilst chemisorption involves covalent bonding between adatom and surface. Both schemes have an effect on the diffusion and nucleation of adatoms (i.e. shorter diffusion lengths for chemisorbed species). Thin film growth can be classified in three mechanisms, dependent on the surface and adatom chemistry. The chemical potential per adatom is given as:

$$\mu(n) = \mu_\infty + \left[\phi_a - \phi'_a(n) + \epsilon_d(n) + \epsilon_e(n)\right] \tag{3.1}$$

where n refers to the adatom, μ_∞ is the bulk chemical potential, ϕ_a is the desorption energy of an adatom from a layer of the same adatom type, $\phi'_a(n)$ is the desorption energy of an adatom from the substrate, $\epsilon_d(n)$ is the dislocation energy of the adatom, and $\epsilon_e(n)$ is the adatom strain energy [74].

Here, if $\frac{d\mu}{dn} < 0$ (i.e. adatom–adatom interaction is favoured), we see Volmer–Weber growth – as coverage of the adsorbate increases, adatom islands are grown [75]. If $\frac{d\mu}{dn} > 0$, (i.e. surface–adatom interaction is favoured), we observe Frank–van der Merwe growth, or, layer–by–layer [76, 77]. Stranski–Krastanov growth is a mixture of both, forming a single layer before growing islands [78]. This is due to the sign of $\frac{d\mu}{dn}$ flipping from an accumulation of strain and dislocation energies. All three growth modes are shown in Figure 3.1.

The role of strain and dislocation energy becomes apparent if we again consider homoepitaxy and heteroepitaxy. Homoepitaxy leads to small strain and dislocation values, producing layers of adatoms with structure indicative of the surface (and bulk). On the other hand, heteroepitaxy with adatoms that are highly incommensurate with the substrate atoms will have correspondingly large dislocation and strain energies – resulting in strong adatom–adatom interaction, and thus, island growth.

3.2 Quasicrystalline epitaxy

Quasicrystal surfaces offer interesting substrates for adsorption studies. From a structural standpoint, their distinctive yet non–identical environments provide a different adsorption landscape compared to crystalline materials [79]. As such, how adsorbates are arranged on QCs, and why they are arranged in such fashion gives us information on QC surface structure and chemistry.

The theoretical challenge to forming a commensurate epitaxial interface here is, of course, the interaction between adsorbates which naturally crystallize in a periodic fashion, and a substrate which is naturally quasicrystalline. Indeed, periodic epitaxial interfaces are characterized by a shared interfacial unit cell [80]. Here, of course, QCs have no unit cell. It has been shown, however, that an epitaxial interface can be formed between two crystals so long as they share at least two non–collinear reciprocal space vectors which are projected onto the proposed interface plane [81]. This derivation does not include periodicity as a condition, and so is viable for the inclusion of quasicrystals [56]. Crystalline phases on QC surfaces can be induced by heavy sputtering, depleting specific atom types preferentially, altering the stoichiometry and thus phase [5]. Various studies investigated the interface between these sputtered QC surfaces and the underlying QC structure as an approach to epitaxial growth, finding vector coincidences between the two phases along axes of rotational symmetry, as required [82–85].

Here, examples of different types of epitaxial growth on QC surfaces (not just iQCs) will

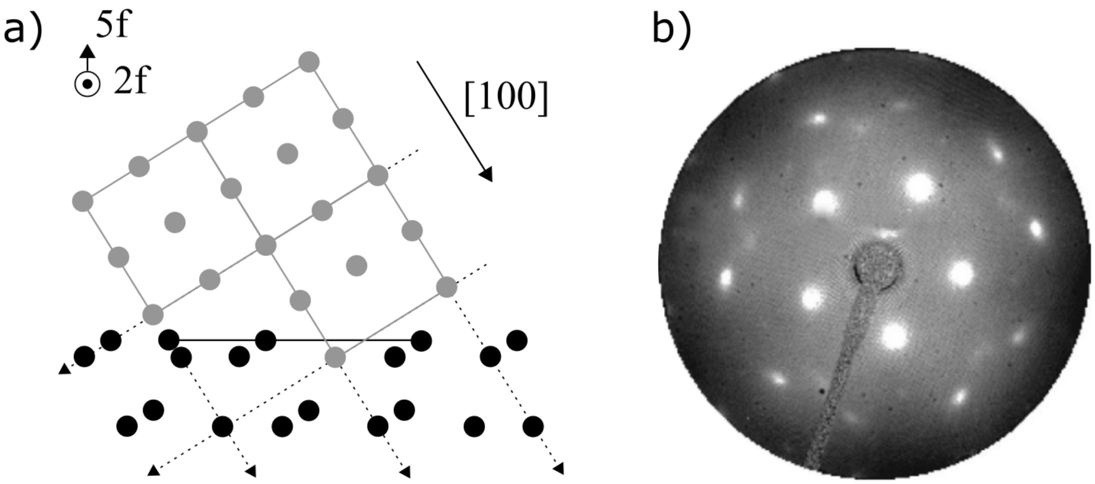

Figure 3.2: **Crystal–quasicrystal epitaxy interface: (a)** FCC Al (grey circles) intersects the 5–fold surface of the *i*–Al–Pd–Mn quasicrystal (black circles), viewed along a 2–fold axis. Other 2–fold axes are shown by dotted arrows. The [100] direction of Al is labelled, showing that it intersects with sets of 2–fold axes at the 5–fold surface. Adapted from [86]. **(b)** LEED pattern taken from the A–Pd–Mn surface, with a thick layer of Al grown on–top. Five bright spots indicate highly crystalline islands oriented in five directions. Reproduced from [87].

be given, classified by the level of influence the QC substrate has on adsorbate structure.

3.2.1 Rotational epitaxy

The minimum impact a QC surface can have on ordered growth is to align the natural crystal structure of the adsorbate along one of the main axes of rotational symmetry. Here, the surface and adsorbate energy is minimised by the lowest energy adsorbate allotrope growing along coincidental, lowest energy rotational axes of the substrate [79, 82, 88]. For example, nano–crystals of Al were grown upon the 5f–Al–Pd–Mn surface, with five domains observed. Each domain exposed the [111] and [100] axes of Al to coincide with the 3–fold and 2–fold axes of the substrate, respectively [86]. An example is shown in Figure 3.2(a). Note that the adsorbed Al is not planar to the surface, in agreement with experiment [87]. The coincidental axes labelled match the vector requirements as discussed earlier. Similar results (5–fold twinning) were found for Ag, Fe, Ni, Co, and Bi/*i*–Al–Pd–Mn, and Al, Ag, Bi, and Xe on decagonal Al–Ni–Co (see [5, 89] for reviews). A Ag film on the 2–fold

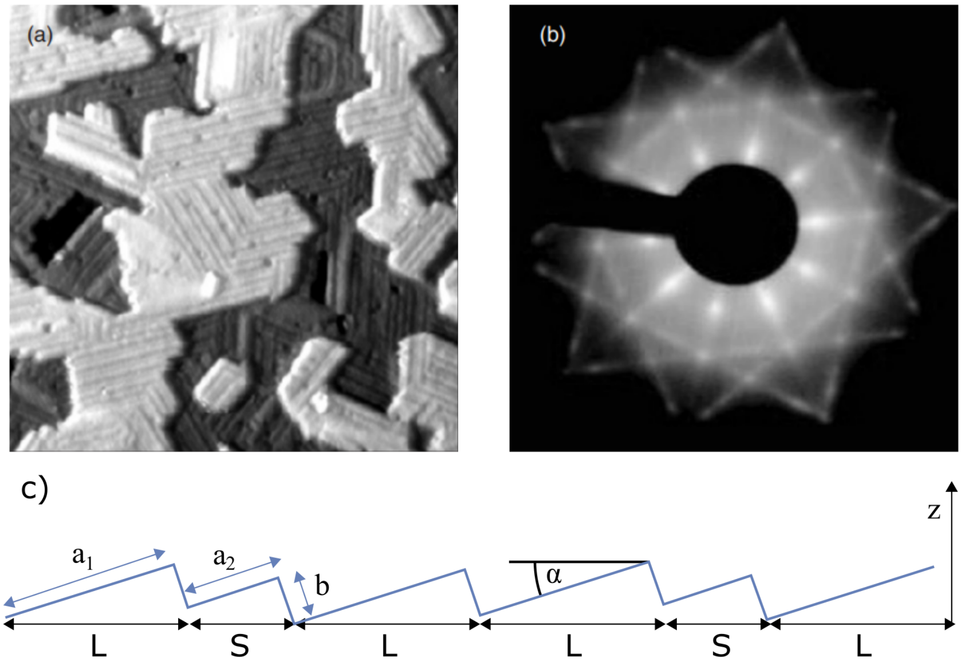

Figure 3.3: **Aperiodically modulated Cu: (a)** STM image of Cu domains oriented along five high–symmetry axes of the i–Al–Pd–Mn surface. Rows in each domain are separated by Fibonacci sequences. **(b)** LEED pattern of the Cu thin film, showing 5–fold twinning of the Cu. The aperiodic nature of Cu perpendicular to the rows is evident by the streaking in the pattern. **(c)** Schematic of how a vicinal surface could approximate aperiodic order. Here, a_1 and a_2 correspond to segments along the [100] plane of a tetragonal bcc Cu structure, with steps along b. α is the angle of the vicinal plane. Reproduced and modified from [90, 91].

i–Al–Pd–Mn surface produces an fcc[111] structure with no twinning, as aligning dense atomic rows at the epitaxial interface leads to one rotational domain [89].

3.2.2 Aperiodic modulation

Rotational epitaxy produces thin films with crystalline order (whose structure is dependent on the coincident lattice [82]), orientated along the substrate high symmetry axes. However, a thin film can also be modulated aperiodically in order to maximise the coincident site lattice with the underlying substrate (equivalent to shifts of the aforementioned reciprocal lattice vectors).

An excellent example of this type of growth is observed when Cu is dosed upon the 5–fold *i*–Al–Pd–Mn surface [92]. Up to $\sim$ 4ML of Cu, intra–layer interactions appear to dominate [91]. At coverages between 5–25 ML, Cu domains grow oriented along the high symmetry axes of the substrate. Within these domains are periodic rows pointing in one direction which have a separation close to Cu–Cu spacing in bulk Cu. These rows are separated by Fibonacci sequences in the perpendicular direction, with a length scale indicative of the pentagrid used to describe the substrate [57]. Phason defects were also detected, which is either an indication of such defects on the surface, or as a method for relieving strain in the Cu from attempts to form a coincident lattice (phasons are the collective motion of jumps or 'flips' of atoms in quasicrystals). As the interlayer separation perpendicular to the surface is periodic throughout the film growth, the Cu is labelled as uniaxially aperiodic. The delayed nature in its appearance (i.e. only from 5 ML and above) was explained by considering a plane vicinal to the (100) direction of a body–centred tetragonal Cu structure [91]. Further experiments utilised the aperiodically modulated Cu to grow a 'checkerboard' structure of pentacene (Pn) molecules [93]. Here, Pn grew in a periodic–like fashion, where *LS* and *SL* segments of the Fibonacci chain were considered indistinguishable, and as one length. This extends the chain into a more periodic sequence [93].

3.2.3 Pseudomorphic/Templated growth

To a certain extent, the previous growth modes discussed have been pseudomorphic, in that adsorbates are structured in an atypical manner to that of its natural crystalline state. Here, examples will be given of overlayers that mirror structural aspects of the QC substrates they adsorb to, i.e. pseudomorphically 'templated' by the quasicrystal surfaces. These overlayers are the most studied modes in QC epitaxy. They pose intriguing questions concerning the behaviour of adsorbate–QC systems, and present examples of limited form single–constituent quasicrystals. The reduced chemical complexity of these systems (i.e. containing only singular building blocks) can also help the exploration of QC behaviour, as they act as models which completely exclude the chemistry of inter–atomic species [67]. Successful templated films have been grown both using elemental and molecular adsorbates across a range of QC substrates. At the atomic level, adsorbates can mimic specific structural features from the substrate. At the molecular level, we can identify specific atomic constituents of the surface based on their chemical interaction with the

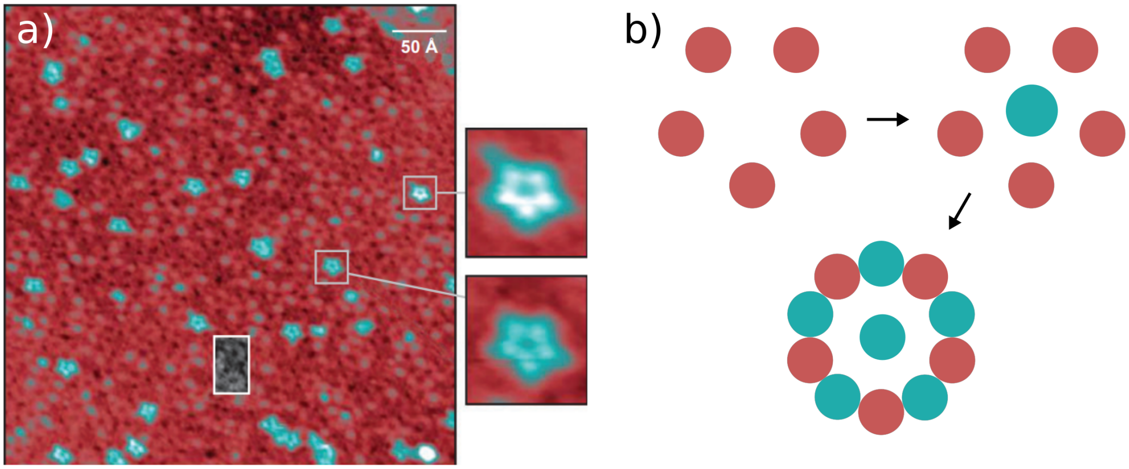

Figure 3.4: **Al adsorption at 5–fold Al–Pd–Mn:** **(a)** STM image (45×45 nm^2) of Al dosed upon the 5–fold surface of an *i*–Al–Pd–Mn QC. Red indicates the substrate, blue indicates the adsorbed atoms. Two pentagonal features are highlighted. **(b)** Schematic showing the adsorption scheme, where an Al atom adsorbs at the centre of a dark star, providing a nucleation site for the 'starfish' formation. Same colour scheme as **(a)**. Reproduced and modified from [99].

adsorbing species. We can therefore utilise both elemental and molecular adsorbates as chemical probes for understanding surface structure.

Elemental films

A number of reviews cover templated elemental adsorption over a range of coverages [5, 94–98]. Here, a few examples will be mentioned.

At low coverages (below 0.1 ML), both Cu and Al occupy the dark star sites of the 5–fold Al–Pd–Mn surface (Figure 2.11), forming structures which are templated by the substrate [94, 99]. Here, the adsorbates diffuse at the surface before 'dropping' into the hollow sites at the centre of the dark stars. Further adatoms can nucleate from these 'centres', forming pentagonal stars, or 'starfish'. The nucleated positions (i.e. legs of the starfish) sit at bridge sites of substrate pentagons, as shown in Figure 3.4. At higher coverages, or when roughly every dark star is filled, a disordered ML is typically formed [94, 99].

There are a number of studies demonstrating successful high–coverage templated/ pseu-

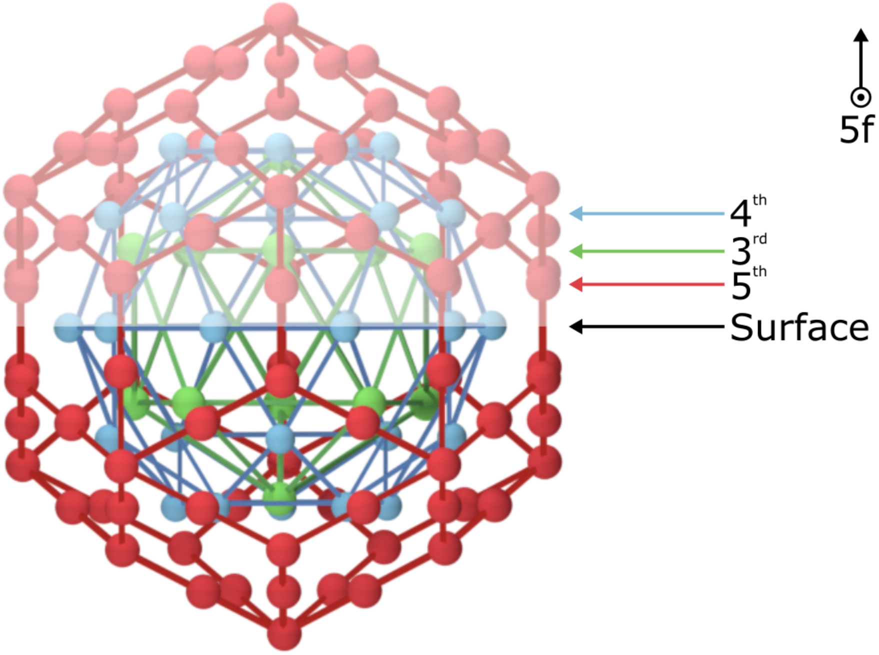

Figure 3.5: **Pb on 5–fold Ag–In–Yb: (a)** A side view of the Cd–Yb cluster, which is oriented so that z is along its 5–fold orientation. The cluster has been truncated through its centre, leaving a surface and vacant planes (translucent atoms). A few planes are labelled, with their constituent shells noted. The 1st and 2nd shells are not shown for clarity.

domorphic growth. Monolayers of Bi and Sb were found to adopt the substrate structure of i–Al–Pd–Mn and decagonal Al–Ni–Co, confirmed by LEED and HAS patterns which exhibit the requisite symmetries and diffraction intensities [56]. Bi adsorption on i–Al–Pd–Mn was also investigated with STM, with the film proving too rough at high coverages. At sub–ML (0.5–0.8 ML) coverages however, STM shows that Bi adopts sites at 'up' orientated pentagons of a Penrose P1 tiling, enclosing a truncated pseudo–Mackay cluster [100]. Likewise, Pb on i–Al–Pd–Mn was found to form a Penrose P1 tiling which was τ–inflated with respect to the tiling that can decorate the substrate. Additionally, this study investigated the properties of the Pb film, finding that a pseudo–gap is formed at the Fermi level (minimal but non–zero states), directly correlated to its quasiperiodic structure [101]. Other successful examples of templated growth include Pb on Al–Ni–Co, and Sn on Al–Cu–Fe [102, 103].

A multi–layer quasicrystalline Pb film was grown using the 5–fold surface of the Ag–In–Yb QC [67]. The growth mode of Pb in this system is unique to the previous systems, and of relevance for this thesis. Here, we can consider a Cd–Yb cluster oriented along a 5–fold rotational axis. If we view the cluster perpendicularly, we are looking along the 5–fold surface. As in Figure 2.12, we see planes of atoms stacked along z, Figure 3.5. In the case for the creation of the surfaces of the i–Ag–In–Yb system, the cluster is truncated through its centre. When Pb was dosed upon 5–fold Ag–In–Yb, each layer adsorbed at sites which were explained by specific vacant planes of the Cd–Yb model 'above' the surface. This multi–layer system was the first example of a quasicrystalline thin film that could be described as 3–dimensional. It has therefore been described as the 'simplest quasicrystal', and is an excellent example of a quasicrystalline system with reduced chemical complexity [67].

Molecular films

The variety and tunability of QC thin films can be increased by molecular adsorption. Organic molecules were initially used to explore the chemical reactivity of QC surfaces, with the majority of studies exploring these systems at room temperature [79, 104]. These explorations typically found no ordering of the chosen molecule. However, either by selecting the 'right' molecule, or by using elevated temperatures (allowing surface diffusion) templating of molecular species was achieved. In turn, the selection of adsorption sites by the adsorbing species gives indications of surface chemistry, or even surface structure. C_{60} has been routinely used as it behaves isotropically (unlike more complex molecules), and has 2–, 3–, and 5–fold symmetry – an important match to icosahedral QCs [104]. Indeed, symmetry matching can play an important part in molecule–QC interaction [105].

C_{60} was chosen as an adsorbate on the 5–fold Al–Pd–Mn surface as its cage diameter ($\sim$7Å) is equivalent to the height of the dark star vacancies observed. At low coverages and at room temperature, it was found to adsorb at positions which were τ–scaled, forming sections of the pentagrid used to describe the dark star hollows [57, 106]. These results mirror (on a different length scale) the Al/i–Al–Pd–Mn experiment detailed above (Figure 3.4). Higher C_{60} coverages resulted in a disordered layer.

Experiments using substrates above room temperature yielded ordered layers of C_{60}. These have been grown on the 5–fold Al–Cu–Fe surface, and the 10–fold Al–Ni–Co and Al–Cu–Co surfaces (i–Al–Cu-Fe is structurally very similar to i–Al–Pd–Mn [107], Al–Ni–Co

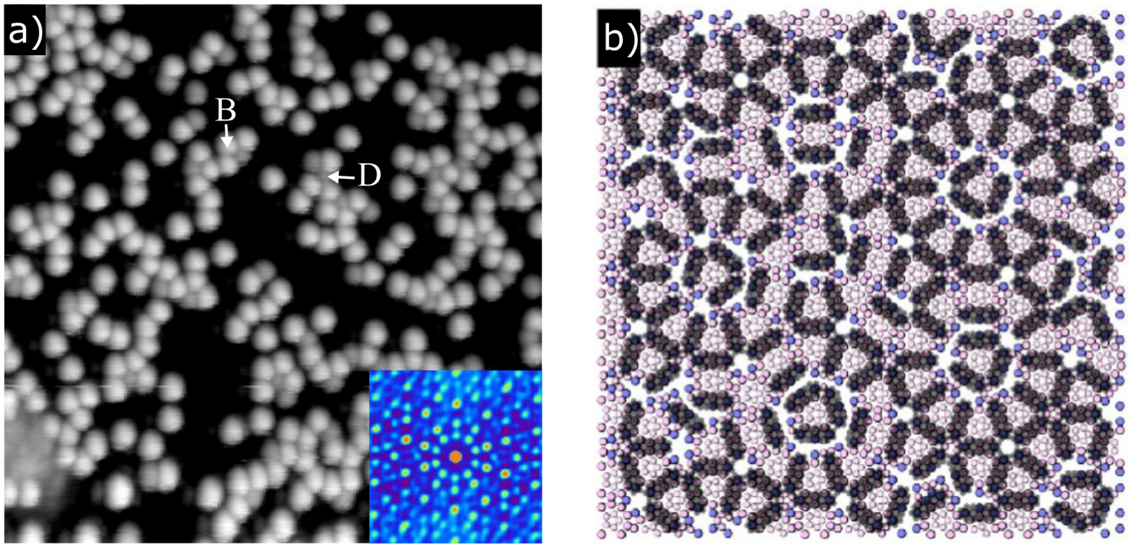

Figure 3.6: **Quasicrystalline molecules:** **(a)** STM image (40×40 nm^2) of C_{60} forming a quasicrystalline adlayer on top of Al–Cu–Fe. Here, bright (labelled as B) C_{60} adsorb to surface Fe atoms, while dark (D) C_{60} adsorb to sub–surface Fe. An autocorrelation function (inset) shows the symmetry and aperiodicity of the molecules. **(b)** Model of Pn adsorbing at *i*–Ag–In–Yb. Here, each end of the Pn molecule adsorbs to Yb atoms (purple atoms). Ag/In atoms are pink. Pn molecules are the dark translucent rods. **(a)** and **(b)** reproduced and modified from [110].

and Al–Cu–Co are isostructural [108, 109]). For example, in the C_{60}/Al–Cu–Fe system, two adsorption sites were found, labelled as bright (B) and dark (D), Figure 3.6(a). Each were associated with Fe adsorption sites, where the bright C_{60} bonded to surface Fe, and dark C_{60} to sub–surface Fe. These dark C_{60} were suggested to slightly reconstruct the sub–surface layer so that a bond could be made [110]. The premise that the minority constituent (here, Fe) plays an important role in adsorption/templating mirrors some of the findings where atomic templating was observed (Si, Bi, and Pb on *i*–Al–Pd–Mn all adsorb at truncated pseudo–Mackay clusters, the centre of which is a lone Mn atom).

The implication from these studies is that, at a unique adsorption–site network, there is a strong enough molecule–surface interaction for C_{60} films to grow in a quasicrystalline manner rather than in its close–packed crystalline form [111]. These QC C_{60} examples are in contrast to self–assembled C_{60} layers upon non–QC metal surfaces. Here, generally, C_{60} grows in a close–packed (hexagonal/honeycomb) fashion with initial nucleation often

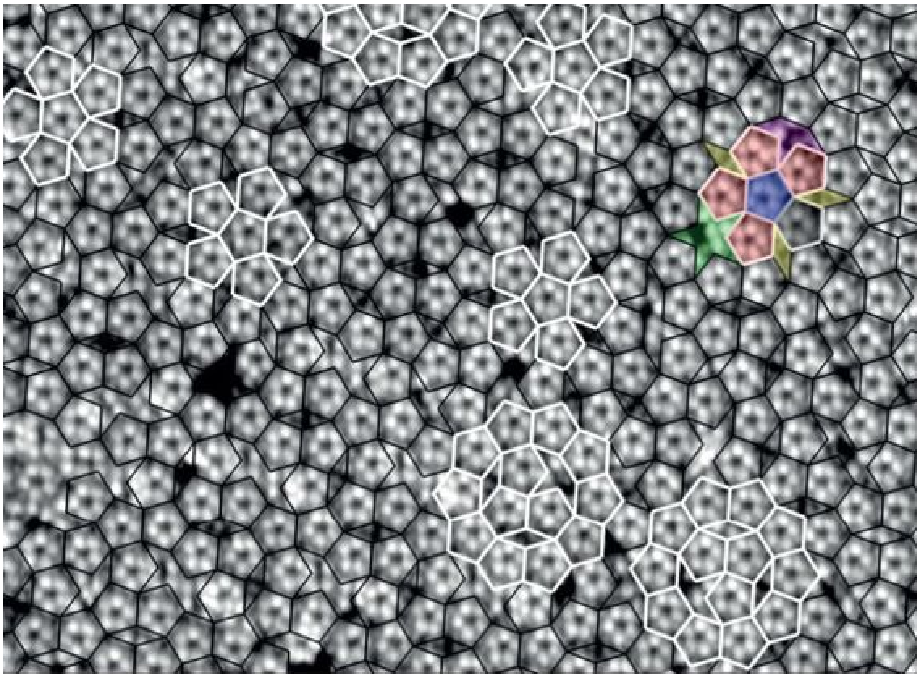

Figure 3.7: **Hydrogen–bonded 2D quasicrystal:** Ferrocenecarboxylic acid on top of a Au(111) substrate self–assembles into a quasicrystalline film with 5–fold rotational symmetry. Overlaid are tiles of the Penrose P1 tiling [115].

observed at step edges [112]. The lattice parameters of these hexagonally close–packed structures are approximately equal to the Van der Waals diameter of an individual C_{60} molecule (1 nm). In this case, intermolecular (Van der Waals) interactions are the primary driving force behind the structure of these films, with molecule–substrate interactions principally affecting the properties of the film. These crystalline phases will often align with high symmetry orientations of the surface, or will bear some indication of the substrate structure – for example, reflecting the herringbone reconstruction of the Au(111) surface [112]. Likewise, changes in brightness detected in these crystalline C_{60} films are often an indication of a surface reconstruction caused by the C_{60}, electronic effects, or are indicative of molecular orientation on the surface [112–114]. The difference in C_{60} film structure (i.e. QC or close–packed) and the interactions that mediate the film growth (i.e. molecule–substrate or intermolecular) are demonstrated in Chapter 5.

Aside from C_{60}, Pn was found to adsorb on the 5–fold Ag–In–Yb surface at specific sites between two Yb atoms at room temperature. Here, the separation of these particular Yb atoms is approximately the length of a Pn molecule. Pn was observed by STM to show a 4–lobed structure, as opposed to its natural 5–lobed state. It was presumed that its electronic structure was altered by the substrate and adsorption site. The Pn positions are quasicrystalline (as determined by the substrate), and their orders of rotation are commensurate with the substrate. This was demonstrated by auto–correlation functions calculated simply using the positions and then, separately, including the rotation of a rod–shaped molecule [110]. A further example of molecular–QC templating is that of corannulene on the 5–fold Ag–In–Yb surface. Both at room temperature, and raised temperatures, the molecule forms a QC layer [116].

Aside from QC surface–molecule systems, there are some examples of molecules forming quasicrystalline arrangements outside of the influence of QC substrates that are of general interest. Here, molecules form stable quasicrystalline arrays upon periodic substrates, or in liquid/micellar formations [10, 13, 115, 117–119]. Figure 3.7 shows an example, where ferrocenecarboxylic acid (FcCOOH) has self–assembled into a quasicrystalline overlayer on a Au(111) substrate. Here, pentamers of the molecule are hydrogen–bonded in a cyclic fashion, joined by FcCOOH dimers. An overlay of a Penrose P1 tiling highlights the quasiperiodic ordering [115].

Chapter 4

Experimental Methods

4.1 Introduction

The methods used within this thesis are based on investigating surface and adsorbate structure of quasicrystals and adsorbate overlayers on these surfaces. The techniques used are amongst the most widespread and well–known within surface science. Here, a brief summary of these techniques will be given, with caveats or specifics relating to quasicrystals stated. Most examples are taken from [120], which provides an excellent summary of surface science in general.

4.2 Ultra High Vacuum

Like any reactive metal sample, ultra high vacuum conditions are important for studying clean quasicrystal surfaces. In air, Al–based QCs oxidize similarly to elemental Al, with the surface passivated by nanometre thick layers of oxide similar to Al_2O_3 [121]. Likewise, the oxidation of the Ag–In–Yb QC surface is similar to the oxidation of each its constituents [122]. In each case, the quasicrystalline structure of the surfaces is destroyed. It is important, then, to provide an environment free of ambient gases with which to study these surfaces. Likewise, UHV conditions are often a pre–requisite for some surface sensitive techniques, due to the requirement of a large mean free path for incident radiation, for example. The basic techniques for creating an ultra–high vacuum environment will be demonstrated here, including how the pressure of the system is measured, as well as sample preparation under these conditions.

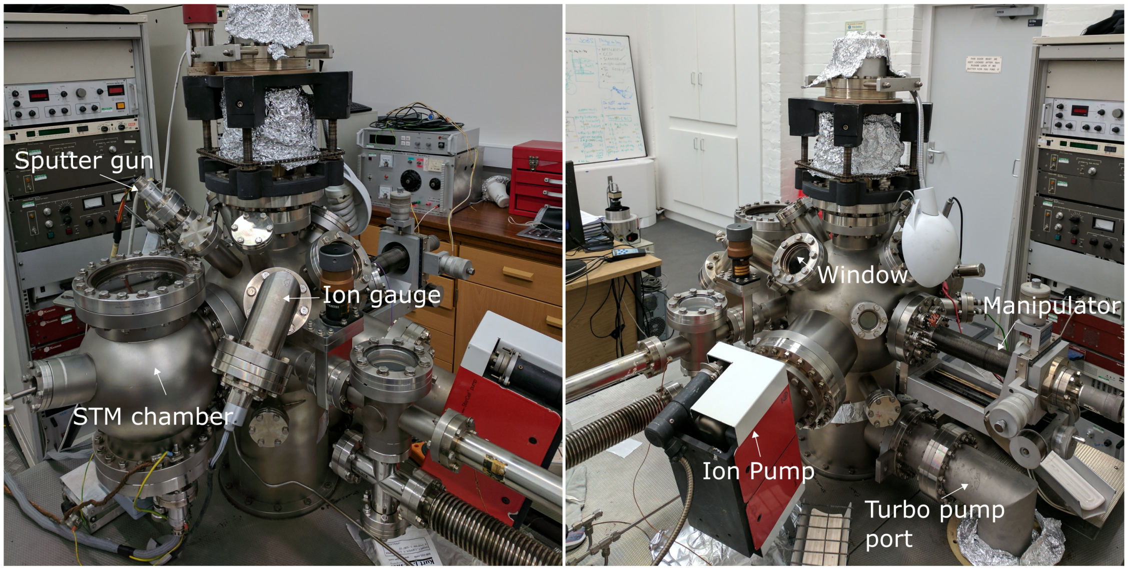

Figure 4.1: **UHV chamber:** The UHV chamber used to produce the results in Chapter 8, with highlighted parts for later discussion.

4.2.1 Pumps and gauges

A UHV chamber is a stainless steel or mumetal vessel, with appropriate ports for connecting the various electronics used for experimental techniques. Additionally, it has ports for windows for ease of manipulating samples within the chamber, and for pumps to connect to. Figure 4.1 shows an example, with labelled ports and windows. Also highlighted is a manipulator, which is used to hold the sample and to change its position within the chamber.

To evacuate a UHV chamber to the requisite ultra–high vacuum pressure (10^{-10}–10^{-11} mbar), a series of pumps are used, as no single pump can reach ultra–high vacuum pressures alone. Initially, roughing pumps are used to create a rough vacuum (10^{-3} mbar), before turbomolecular and ion pumps are used to reach the UHV vacuum level. Titanium sublimation pumps can additionally be used to improve the vacuum further [120].

A rotary vane pump is a type of roughing pump, typically able to pump down to 10^{-3} mbar. These can be used simply to achieve a relatively low vacuum, or, to act as a backing pump for a turbomolecular pump. Here, an eccentrically mounted rotor rotates around a stator block. Gas on the chamber side is trapped between the rotor and stator, before being compressed and expelled through an exhaust to the atmosphere. Figure 4.2(a) shows

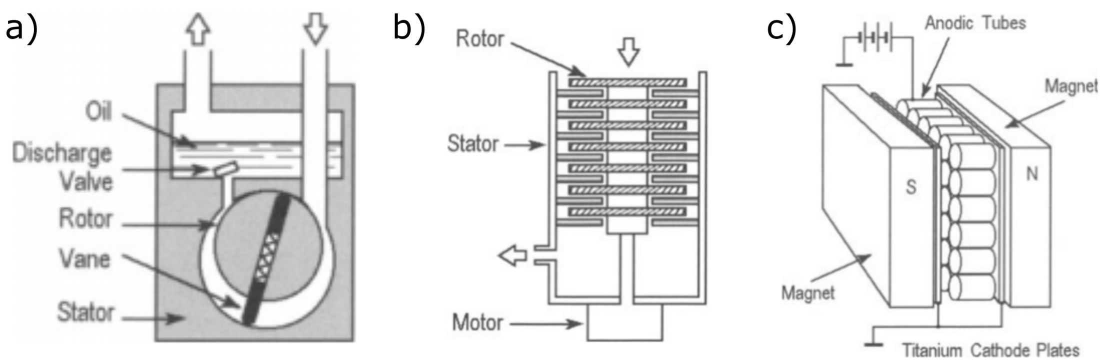

Figure 4.2: **Pump schematics:** **(a)** The schematic of a rotary vane pump. An eccentrically mounted rotor spins, trapping gas between the walls of the rotor and stator block. This compresses and expels gas through an exhaust. An oil reservoir acts as a sealant. **(b)** Schematic for a turbo pump. A set of rotor and stator blades are labelled, which force gas molecules towards an exhaust. **(c)** The schematic of an ion pump. Labelled are Ti cathodes and stainless steel cylinders. Reproduced and modified from [120].

a schematic.

A turbomolecular pump also uses a set of rotor vanes, which have an angled leading edge, and are stacked between stator vanes. The rotor vanes rotate at high speeds (50,000–100,000 RPM) directing gas molecules to its exhaust. Figure 4.2(b) shows an example. Turbo pumps are excellent at providing vacuum conditions, yet their high rate of rotation can induce vibratory noise when conducting STM, for example [120].

Ion pumps provide an elegant solution, having no moving parts. Here, two Ti cathode plates are separated by an array of anodic steel cylinders. A magnetic field is applied across the whole assembly, parallel to the cylinders. Electrons are emitted from the cathode plates, travelling in a helical motion around the steel cylinders due to the applied magnetic field. These electrons ionise gas molecules, which are accelerated to a cathode plate by an electric field. Upon impact, Ti is sputtered onto the surrounding chamber walls, steel cylinders, and cathode plates. The result is that the ionised molecule is buried into the cathode, and neutral molecules can react with the sputtered Ti, leading to a net reduction in the pressure. Figure 4.2(c) shows a schematic of an ion pump. The pressure of the system can also be measured in the ion pump, as the number of incumbent ionized molecules per second gives an indication of the overall pressure.

Finally, a titanium sublimation pump (TSP) is often used to remove further gases.

This works similarly to the sputtered Ti from the ion pump. Here, a Ti filament is heated by a high current, subliming Ti atoms which are sputtered onto the walls of the chamber. Active gases interact with the Ti, reducing the overall pressure.

To pump a chamber from atmospheric pressure to UHV, the rotary and turbomolecular pumps are used to reach pressures down to 10^{-7}–10^{-8} mbar. Afterwards, the whole system is 'baked' i.e. covered with a metallic 'tent' and heated to $\sim$120°C. This is to help evaporate and remove any residual gases, particularly water vapour. Then, the ion pump is de–gassed (i.e. removing adsorbed gas molecules from the pump assembly) and turned on. Likewise, other filament–based instruments are slowly degassed during or shortly after the bake–out, to reduce contamination when they are used later.

To measure the pressure of the chamber (below 10^{-3} mbar), an ion gauge is used. Similar to the measurement of pressure from an ion pump, the number of ionized molecules which impinge upon a collector are a direct indication of the pressure of the system. Here, again, a filament emits electrons which are attracted to a grid which is held at a positive potential. The electrons ionize molecules and atoms in the chamber, which are then collected, giving a current proportional to the number of molecules within the system. For lower pressures, useful for knowing when the requisite pressure for backing a turbo pump is reached, a Pirani gauge can be used. Here, the resistance of a filament is monitored, so that the higher the resistance measured, the lower the pressure.

The data presented within this thesis were obtained using two separate UHV machines, one of which is shown in Figure 4.1. This machine consists of a central chamber connected to an STM scanner, as labelled. The chamber was evacuated to ultra–high vacuum using a rotary, turbo, and ion pump. A TSP was routinely used in addition to these pumps. An extra rotary and mini–turbo pump were used to evacuate a load lock – an intermediary port between the UHV chamber and atmosphere which allows for sample insertion/removal without breaking the main chamber vacuum. The base pressure of the main chamber was routinely in the low 10^{-10} mbar range. The second UHV machine consisted of two separate, yet connected, chambers – one 'preparation' chamber, and one 'analysis'. Again, these were evacuated using rotary, turbo, ion, and TSP pumps. A gate valve separated the two chambers when necessary. This set–up allows complete isolation of the STM scanner and LEED optics when preparing the sample. The base pressure of the preparation chamber was typically in the high 10^{-10} mbar range, whilst the analysis chamber was held in the mid 10^{-11} mbar range.

4.2.2 Sample Preparation

Large single–grain quasicrystals can be grown using any of the typical crystal growth techniques, such as the Czochralski, Bridgman, floating–zone, or self–flux method [123]. Each will be briefly described. The Czochralski method [124] uses a 'seed' crystal (i.e. a small single–grain crystal or polycrystal with the same or similar composition of the desired material), typically oriented along a specific direction, which is attached to a 'pull rod'. This seed crystal is inserted into a molten solution of the correct stoichiometry of the desired alloy, which is held in a crucible. The seed is then pulled slowly from the molten mixture, and rotated as it is pulled. As the pulled mixture cools, it crystallizes, Figure 4.3(a). Similarly, the Bridgman method uses a seed crystal inserted into a melt. Here, however, the molten mixture is cooled gradually from the seed end, either using a heating element with a temperature gradient, or by slowly pulling the crucible through two (high and low) temperature zones [125].

The floating–zone method employs a polycrystalline 'feed' rod of the same composition of the target quasicrystal, Figure 4.3(b). Here, a heating coil creates a high temperature

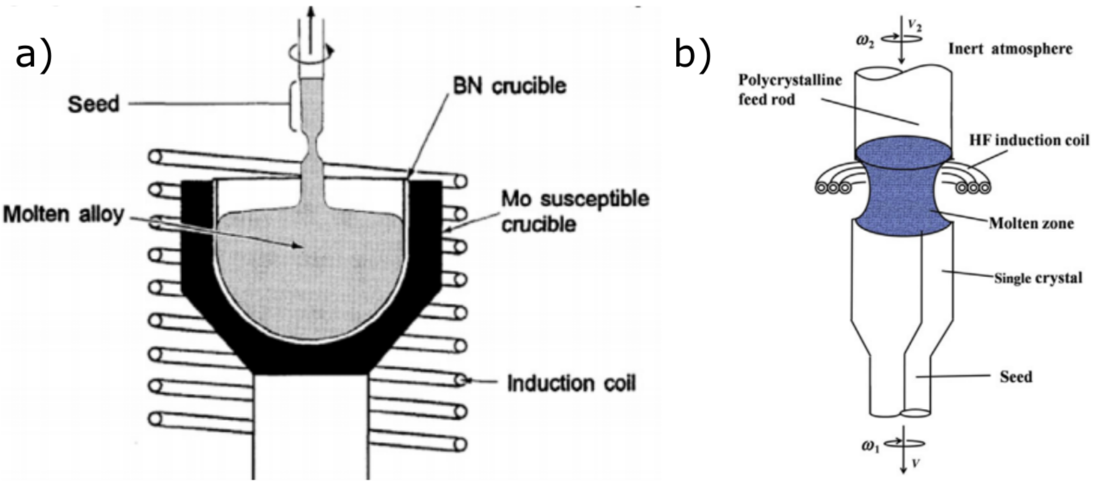

Figure 4.3: **Crystal growth techniques: (a)** The Czochralski method. A seed crystal is inserted into a melt which is held (in this case) a boron nitride crucible. The melt is heated by an induction coil. The seed is retracted and spun. The cooling melt crystallizes. **(b)** The floating zone method. An induction coil melts a 'floating' zone of a polycrystalline feed rod. The rod is pulled through the heating coil, so that the floating zone is moved upwards. A single crystal is created at the bottom. Reproduced and modified from [123].

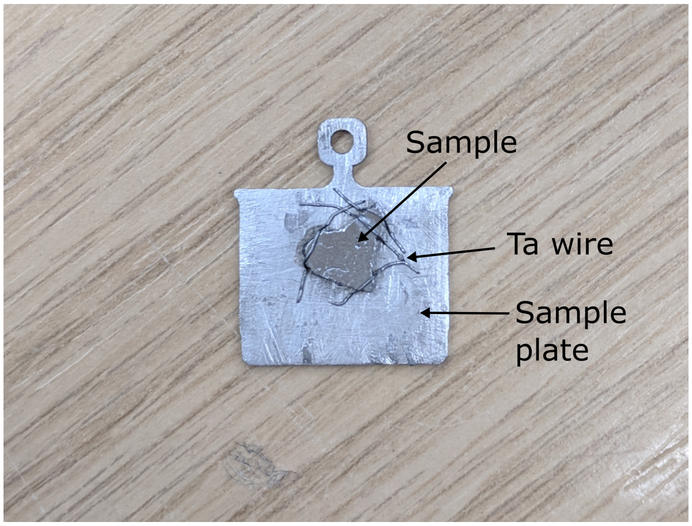

Figure 4.4: **Sample plate and sample:** An example of a quasicrystal mounted to a sample plate. Here, the sample pictured is a 10–fold Al–Ni–Co. It is mounted to the sample plate using tantalum (Ta) wire, as shown.

zone which melts the polycrystal as it is pulled through. Single–crystal growth occurs by moving this 'floating zone' from the bottom to the top of the feed rod. Finally, the self–flux method relies on the fact that for some QC alloys, the solid QC is in equilibrium with its melt in its phase diagram. Here then, the correct ratio of pure constituents is melted in a crucible or tube, and slowly cooled. For each type of growth method used, a detailed phase diagram for the relevant mixture of constituents is needed for successful growth.

Upon growth of a single grain quasicrystal, a 'sample' which will be used for surface investigations is produced by cleaving the ingot along the required high–symmetry direction (deducted by Laue diffraction). These samples are typically 10–15 mm in diameter, and perhaps 1.5 mm thick. Before insertion into UHV, these samples are polished using diamond paste and a lapping film. The lapping film or paper is an abrasive material (0.01–45 μm grades), upon which a small amount of diamond paste is placed (1 mm diameter bead). The required surface of the sample is then placed face–down onto the diamond paste, and polished using a figure of 8 formation for approximately 15 minutes, with even pressure applied across the sample. This ensures that no one orientation is polished favourably, or that facets are induced. Successively finer grades of diamond paste are used (6–0.25 μm) after each 15 minute cycle. In between cycles, the sample is washed in a beaker containing methanol (or other suitable solvent), inserted into an ultrasonic bath, to remove residual paste.

After a mirror shine of the surface is produced, the sample is mounted to a plate which can be used for manipulation inside the UHV chamber, shown in Figure 4.4. This plate is typically made of stainless steel, tantalum, or molybdenum. The sample is fixed in place by spot–welding tantalum wire straps to the plate. A tight fit is needed to ensure no sample movement during surface investigation. Once the sample is mounted, it can be inserted into the load lock of a UHV machine, which is then pumped down until it can be opened to the main chamber, and inserted into the manipulator.

4.2.3 Surface Preparation

To prepare atomically flat surfaces, cycles of sputter–annealing are used. Sputtering is the process of using ionised inert gases to clean the surface. Within an ion gun, a filament emits electrons producing ions of the chosen inlet gas (here, Ar) which are then accelerated to energies of 0.5–5.0 keV [120]. These ions are directed towards the sample. The sample is tilted to provide a grazing angle for the impinging matter, so that the ions are not directly embedded into the surface. Additionally, the sample is grounded, so that impinging ions do not build up a net charge which would cause other ions to be deflected by repulsive interactions. The drain current of the incident ions gives a measure of the number of ions in the sputter beam. Incident ions then eject both physisorbed and chemisorbed species from the surface, alongside surface atoms. This process therefore removes contamination, but also causes damage to the surface structure, producing a rough topography. Typically, surface atomic species which are not tightly bound or the lighter mass elements are ejected preferentially. When quasicrystals are sputtered, a crystalline phase is created through this change of stoichiometry [5, 126].

To gain an atomically flat surface, the sample is then heated, which is known as annealing. This provides enough thermal energy for surface atoms to diffuse and maximise their coordination number. It also allows for the desorption of any Ar ions which have adsorbed to the surface. Likewise, it enables diffusion of atomic species from the bulk, which replenishes the elements removed preferentially by sputtering. Repeated cycles of sputtering and annealing create a flat, ordered surface which is suitable for structural analysis or adsorption studies.

4.2.4 Evaporation of adsorbates

To deposit adsorbates onto the surface, physical vapour deposition is used. Here, high purity adsorbates are sublimed through either filament heating or an e–beam evaporator, dependent on the sublimation temperature of the source material. For lower sublimation temperatures (molecules and low–melting point metals) filament heating is often adequate. Here, the adsorbate is contained within a high melting point cell (Pyrex, for example) with a tungsten filament tightly wound around the cell. The filament provides conductive and radiative heat to sublime the adsorbate, which is directed towards the substrate. Other direct heating methods include passing a current through a tungsten foil packet which contains the adsorbate.

For higher melting point materials, an e–beam evaporator is used. Here, the adsorbate is either a rod, or is contained within a high melting–point crucible, typically alumina or molybdenum based. A high voltage is applied to the rod/crucible, with a nearby heated filament providing thermally emitted electrons which are attracted to the rod/crucible by its high voltage bias. This provides a localised high temperature, evaporating the adsorbate within the crucible.

4.3 Surface analysis techniques

4.3.1 Scanning Tunnelling Microscopy

Scanning tunnelling microscopy is a widely used surface specific technique developed by Binnig and Rohrer, for which they received a Nobel prize (1986) [127]. STM explores the joint electronic density of states of the sample surface and the tip, which gives an indication of the surface topography. Careful consideration of data is important, as protrusions could be topographical, or merely an increase in the local density of states.

In operation, the STM uses (ideally) an atomically sharp tip, typically made of W, Pt–Ir, or Au, which is physically sheared or electrochemically etched ex–situ. From here, the tip is inserted into the STM scanner which consists of piezoelectric ceramics which govern fine control in x, y, and z. The tip coarsely approaches towards the sample, before being finely controlled to within < 1 nm of the surface. Figure 4.5(a) shows a schematic of the basic principle. Here, the wave functions of the surface and the closest tip atom overlap [120]. By applying a bias to either the tip or the sample, electrons can tunnel between the two. If we consider applying a bias to the tip, then filled surface states are

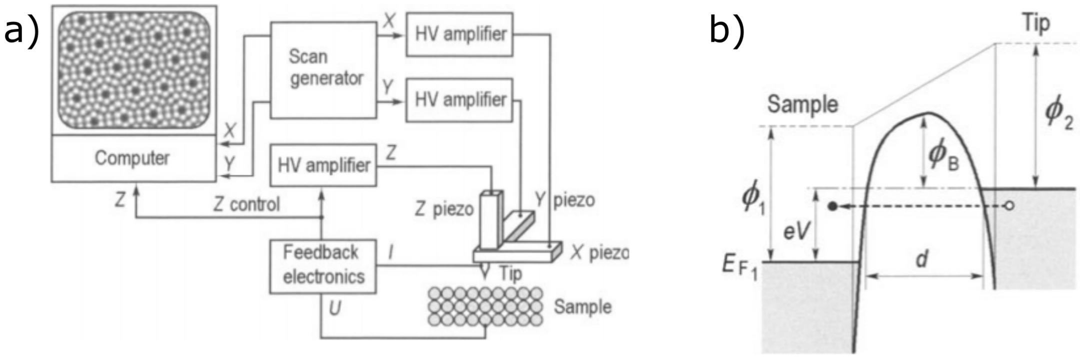

Figure 4.5: **Schematic of STM: (a)** A diagram of the basics of STM. A tip is attached to a scanner which is moved using piezoelectric ceramics. The signal from the piezoelectrics are amplified and interpreted to give an STM image. **(b)** A diagram showing the principle of quantum tunnelling to produce an STM image. ϕ_i refers to the work functions of the sample and tip, whilst E_{Fi} are their Fermi levels. Other notations are referred to in the text. Reproduced and modified from [120].

explored if the bias voltage is positive and vice versa for negative bias. Figure 4.5(b) shows an example of how negative bias explores empty states. The tunnelling current produced is given as:

$$j = \frac{D(V)V}{d}\exp(-A\phi_B^{1/2}d) \tag{4.1}$$

where d is the effective tunnelling gap, *D(V)* is the electron density of states, A is a constant, and ϕ_B is the effective barrier height of the junction between the Fermi levels of tip and surface [120]. Inspection of Equation 4.1 reveals a high dependence of the tunnelling current on d – the distance between tip and surface. Indeed, a change of 1Å causes an order of magnitude difference in the tunnelling current. Lateral resolution is dependent on the shape of the tip, so that single atom tips provide the greatest resolution (∼2Å).

STM is run in two different modes, constant current or constant height. In constant current mode, the z piezo changes the height of the tip above the surface to keep a constant tunnelling current set–point. The changes in z are then interpreted as topographic data. Constant height mode keeps the tip at set height above the surface, so that topographic changes in the surface result in a change in tunnelling current. Constant current mode is the most widely used method, and is used in this work [120].

Structural analysis techniques

Within this thesis, the primary interest in STM images is to identify substrate and adsorbate structure. As such, it is appropriate to explain techniques/software which are used to help deduce ordering in images. Two techniques which are used with regularity in this work are fast Fourier transforms (FFTs) and autocorrelation functions. Both FFT and autocorrelation function analysis are accomplished in this thesis using the WSxM and Gwyddion software packages [128, 129]. Likewise, these packages are used for measuring distances, heights etc.

The FFT process deconvolves any signal from an image into its sin and cosine functions, each with its own amplitude and frequency. The transformation of a real–space image is then represented in the Fourier domain, where each point in the Fourier domain corresponds to the frequencies of these functions. High intensity spots in the Fourier domain correspond to repeated 'measurements' of particular frequencies i.e. common separations in real–space. Consequently, taking an FFT of an image reveals any repeated pattern in any direction. Therefore, the rotational symmetry of an STM image may also be inferred from an FFT.

Taking an autocorrelation function of an STM image also shows its measure of order. Here, the analysis is completed in real–space. The image matrix of an image is taken and shifted some distance in x and y with respect to the origin. The difference between the original and shifted image is then taken. As a consequence, any similarities between the shifted images will give rise to a similar pattern in the autocorrelation.

If we consider quasicrystals and the Fourier transform of a 1D Fibonacci chain, then we produce a dense set of components in the Fourier domain analogous to its diffraction pattern in Section 2.2. As with the diffraction of a 1D chain, however, spots of appreciable intensity in Fourier space are only found at certain frequencies. A similar phenomena occurs when taking the autocorrelation function.

Throughout the discussion sections of the data presented in this thesis, FFT and autocorrelation function analysis is used to assess the long–range structure of both substrate and adsorbate. As previously mentioned in Chapter 2, section 2.2, if quantities which are representative of a crystal's long–range order are τ–scaled, then said structure is considered quasicrystalline (e.g. high intensity diffraction spots). This holds for both FFT and autocorrelation analysis. Both techniques highlight rotational symmetries and long–range order (through the presence of high intensity spots relating to commonly occurring frequencies/separations). If we consider the FFT of a single quasicrystalline phase, the presence of high intensity τ-scaled spots along high–symmetry directions indicates an irrational ratio between length scales within the structure (for example 1:τ, or S:L), which in turn indicates aperiodicity, or, a lack of translational symmetry. By the definition used in this thesis and the wider literature, a structure which gives such an FFT would be classified as quasicrystalline i.e. a structure with aperiodic long–range structure. Of course, careful analysis is required both in Fourier and real–space to ensure that multiple (periodic) phases are not producing sets of high intensity spots with a commensurate, rational modulation ratio of ∼1.6, akin to the twinning argument proposed by Pauling to explain quasicrystalline diffraction patterns [3].

STM image distortion

With the possible exception of images obtained through low–temperature operated STM, raw STM images are rarely free of any distortion. Distortion here refers to any artefact of the image that is not directly or graphically representative of the topography of the surface. These can be induced by, for example, the STM tip, the piezoceramics in the scanner, or, the interface between tip and surface. The software used here has options for removing/fixing these, with a few examples detailed here. Plane levelling is used to correct the fact that tip and sample are never truly perpendicular, levelling out heights across the scan. Drift correction corrects the drift which arises from thermal expansion in the scanner. Finally, scar removal averages out corrupted lines/points which arise from a fault in the closed loop between tip and surface.

4.3.2 Low Energy Electron Diffraction

Theory

Low energy electron diffraction is another technique which is used to probe surface structure. Here, a beam of electrons scatter elastically from the sample surface, providing information on the reciprocal space lattice of the surface. Low energy electrons are as their de Broglie wavelengths are comparable to or less than inter–atomic distances at a surface:

$$\lambda = \frac{h}{\sqrt{2mE}} \tag{4.2}$$

where h is Planck's constant, m is the mass of the electron, and E is the energy of the electrons. If E = 30–200 eV, the wavelength of the electron is approximately 1–2 Å.

Likewise, their mean–free path is short, leading to elastic collisions occuring only in topmost surface layers [120].

As this technique relies on diffraction, analysis of the deflected electron beam is required. The reciprocal lattice of a set of points in real–space is defined by:

$$\mathbf{G}_{hkl} = h\mathbf{a}^* + k\mathbf{b}^* + l\mathbf{c}^*$$

where h, k, and l are Miller indices, and $\mathbf{a}^*$, $\mathbf{b}^*$, and $\mathbf{c}^*$ are reciprocal space vectors, related to real–space lattice vectors $\mathbf{a}$, $\mathbf{b}$, $\mathbf{c}$ by:

$$\mathbf{a}^* = \frac{2\pi\mathbf{b}\times\mathbf{c}}{\mathbf{a}\cdot(\mathbf{b}\times\mathbf{c})}, \quad \mathbf{b}^* = \frac{2\pi\mathbf{c}\times\mathbf{a}}{\mathbf{b}\cdot(\mathbf{c}\times\mathbf{a})}, \quad \mathbf{c}^* = \frac{2\pi\mathbf{a}\times\mathbf{b}}{\mathbf{c}\cdot(\mathbf{a}\times\mathbf{b})},$$

Now, the wave vector of an incident ($\mathbf{K}_0$) and scattered ($\mathbf{K}$) electron beam are related by:

$$\mathbf{K} - \mathbf{K}_0 = \mathbf{G}_{hkl}$$

and as the scattering is elastic, $|\mathbf{K}|=|\mathbf{K}_0|$. Furthermore, as the periodicity of the surface lattice is zero in the direction normal to the surface, we can say that

$$\mathbf{K}^{||} - \mathbf{K}_0^{||} = \mathbf{G}_{hk}$$

i.e. the incident and deflected beam only need to be considered in terms of directions parallel to the surface. This also implies that the conservation of momentum need only be considered for the parallel component of the wave vectors.

Now, the reciprocal lattice of the surface can be considered as a set of rods which extend perpendicularly from the surface lattice, where the reciprocal lattice points are infinitely dense along the rods. We can then model an incident wave vector $\mathbf{K}_0$ terminating at a reciprocal lattice rod that has its origin at a surface lattice point. A sphere of intersection (known as Ewald's sphere) is therefore defined by the radius of the incident wave vector, with an origin at the centre of the incident wave vector. The rods which intercept the Ewald sphere therefore give the wave vectors $\mathbf{K}$ for diffracted beams, shown in Figure 4.6(a) [120]. These 'allowed' beams give spatial information on the surface lattice in reciprocal space.

The intensity of these beams can be interpreted to give information on the arrangement of atoms in the surface unit cell. The technique used to discern this information is known as LEED I–V, where the intensity of the observed diffraction spots is monitored as a function

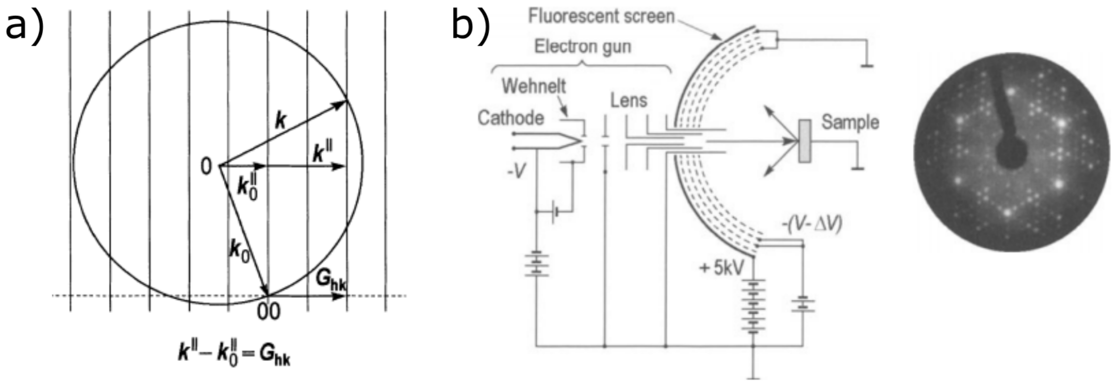

Figure 4.6: **LEED schematic:** **(a)** The construction of the Ewald sphere which shows the allowed diffracted beams from an incident beam $\mathbf{K}_0$. **(b)** A schematic of the LEED experimental setup, with an example LEED pattern from the Si(111)7×7 reconstruction. Reproduced and modified from [120].

of changing electron energy. This is an iterative process, which is compared to calculated I–V curves generated for a number of possible structures. For example, a LEED pattern gives the surface reciprocal lattice. From here, an initial surface structure is proposed, and I–V curves are calculated bearing this structure in mind. These theoretical curves are then compared to experimental ones, and the structural model is refined until a satisfactory match is made. The fit between theory and experiment is given quantitatively by the reliability factor R. The lower the R–factor (< 0.5), the better the match [120].

LEED pattern of a quasicrystal

The diffraction of a Fibonacci chain was derived in Section 2.2.2. A 1D Fibonacci structure can be described by two periodic functions, each with mutually incommensurately modulated periods [20, 130]. Each function therefore is spaced periodically in reciprocal space with sets of Bragg peaks at an incommensurate periodicity of Q_1 and Q_2, and additional sets from linear combinations of Q_1 and Q_2. This leads to an infinitely dense set of Bragg peaks. However, as previously shown, only a few of these peaks have any appreciable intensity. This simple demonstration shows how a quasicrystal can exhibit a LEED pattern despite its aperiodicity.

Experimental setup

The basic constituents of a LEED unit are shown in Figure 4.6(b). These are an electron gun with a focussing Wehnelt cylinder, and a hemispherical fluorescent screen, which is used to observe the diffracted beams from the sample surface. The screen is held at a high voltage for acceleration of diffracted electrons. In front of the screen are four grids, the first of which is grounded to act as a block between the field of the screen and the sample. The second and third grids are held at potentials close to the potential of the cathode of the electron gun, and are used to reject inelastically scattered electrons. The voltage of these screens can be adjusted to give the greatest signal–to–noise ratio, where the larger the difference to the cathode voltage, the brighter the spots and background intensity. The fourth grid is again grounded, and acts as a voltage screen between the other grids and the field of the fluorescent screen.

Chapter 5

2–fold *i*–Al–Pd–Mn: clean surface and C_{60} adsorption

The work contained in this chapter focusses on the 2–fold surface of the *i*–Al–Pd–Mn quasicrystal, C_{60} adsorption on the QC phase, and other impurity phases detected at the surface. Also of note is the introduction of the Fibonacci square grid to this thesis. This 4–fold rotational quasicrystal plays an important role in the results discussed here. Previously only considered as a theoretical construct, it is shown that C_{60} adsorbs in a Fibonacci square grid structure at the 2–fold *i*–Al–Pd–Mn surface as a result of a sparse Mn adsorption site distribution.

5.1 Introduction

In comparison to the 5–fold termination, the 2–fold surface of the *i*–Al–Pd–Mn quasicrystal has been relatively under–researched. LEED and XPS studies indicated that this surface could exhibit 'a bulk–terminated face–centred icosahedral 2–fold surface with a bulk composition' [131]. Prior to the work detailed here, two studies were successful in using STM to gain atomic resolution of 2–fold *i*–Al–Pd–Mn [132, 133]. However, neither came to any conclusive agreement on the specific nature of the surface in terms of atomic motifs, in contrast to the body of work discussing the origin of the white flowers and dark stars of the 5–fold surface [57–60, 62].

As evidenced by STM, the 2–fold surface shows step heights that follow a τ–scaled relationship, $h \times \tau^n$, where $h = 0.24$ nm, and n is an integer. [132–134]. These heights

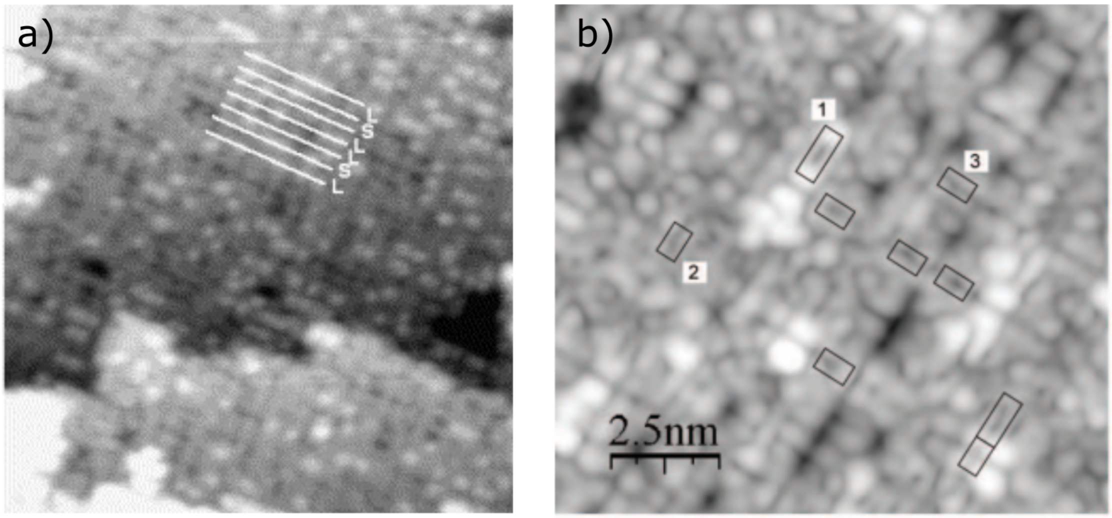

Figure 5.1: **STM of 2–fold *i*–Al–Pd–Mn:** **(a)** STM image (60×60 nm^2) of the clean 2–fold i–Al–Pd–Mn surface. A row structure is visible, with bright features in rows highlighted, forming a Fibonacci sequence. Reproduced from [132]. **(b)** High resolution STM image (10×9 nm^2). Highlighted are rectangles with 1:τ^n edge lengths. For example, rectangle 1 has edge lengths of 0.480 nm and 1.257 nm (1:τ^2). Reproduced from [133].

have been related to the edge lengths of pentagonal faces of Bergman clusters along the 5–fold orientation, with the conclusion that the 2–fold surface does not relax in any manner [133]. Terraces are rough, with rows and troughs oriented in two orthogonal directions. These features are thought to be due to missing rows of atoms in the formation of the surface, attributed to preparation conditions [133]. Bright features in rows were found to be separated by Fibonacci sequences with $S = 1.4$ nm, $L = 2.2$ nm, Figure 5.1(a) [132]. Likewise, rectangles with edge length ratios of 1:τ^n were observed, tentatively identified as contributions from Al atoms, Figure 5.1(b) [133].

Deposition of Ag on the 2–fold i–Al–Pd–Mn surface resulted in an fcc(111) structure, with the Ag growing along the atomic rows to produce one rotational domain [89]. Cu has also been deposited, producing islands which show a LEED pattern which is commensurate with the substrate – here, atomic–scale resolution of the Cu was not achieved, so a detailed discussion on its structure was not possible [132].

The Penrose P1 tiling was used as a tool to aid structural understanding of the 5–fold surface, connecting the centres of truncated Bergman clusters [53]). In comparison, the lack

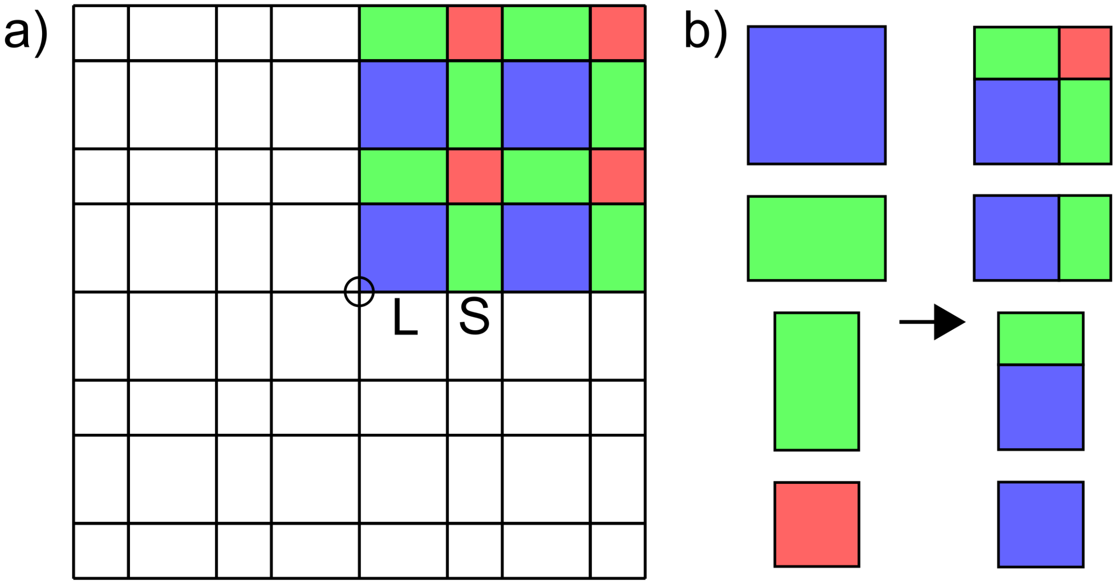

Figure 5.2: **Fibonacci square grid:** **(a)** Superimposed orthogonal sets of Fibonacci chains create the square grid, composed of $S\times S$, $S\times L$ and $L\times L$ tiles (red, green, and blue respectively). **(b)** Deflation rules for each proto–tile.

of identifiable motifs makes application of similar techniques on the 2–fold surface difficult. However, it was noted that the LEED pattern and FFT observed from the 2–fold surface was 'very reminiscent of the square Fibonacci tiling', a 4–fold aperiodic tiling introduced by Lifshitz [21, 132].

The Fibonacci square tiling, or grid, can be constructed by superimposing two identical sets of extended Fibonacci chains perpendicularly to each other, Figure 5.2. The square grid has 4–fold symmetry, exhibits aperiodic, long–range order, and displays no translational symmetry. Lifshitz argued that it was a model quasicrystal, and that the definition of a quasicrystal should not depend on the exhibition of classically 'forbidden' symmetries. The grid can be decomposed from the orthogonal superposition of chains into proto–tiles. They are labelled as $S\times S$, $S\times L$ and $L\times L$ tiles in Figure 5.2, with reference to the segments of the chain that enclose each tile. Each tile can be inflated/deflated according to the scheme presented in Figure 5.2(b). Indeed, it is easy to consider how such a structure could aid characterisation of the 2–fold i–Al–Pd–Mn surface, if the length scale of one of the constituent sets of Fibonacci sequences differed to the other, producing 2–fold symmetry.

Similarly, basis decoration of the vertices of the grid could produce a 2-fold symmetric structure embedded within a 4–fold framework. Lifshitz noted in his original paper that there had been no observation of a physical quasicrystal with Fibonacci square (or cubic) grid ordering. However, photonic properties of manufactured arrays with the Fibonacci square grid structure have been investigated [22].

In this study, new STM images are presented, showing a conclusive structural match to specific truncations of the bulk model structure proposed by Bourdard et al. [36]. The surface is identified as two closely separated planes, with the bright features previously observed identified as Al dimers. This surface model produces a sparse Mn distribution that shows a Fibonacci square grid structure, with occasional τ–deflated positions. This model successfully explains adsorption sites for the epitaxial growth of C_{60} at the surface, which produces a Fibonacci square grid structure with the same length scale as the Mn distribution. This study was motivated by the previous studies of templated molecular growth on raised temperature QC substrates, in which C_{60} adsorbed at minority constituents of each surface, as described in Chapter 3.

5.2 Experimental details

An i–Al–Pd–Mn quasicrystal was polished perpendicular to its 2–fold orientation using a series of successively finer diamond pastes (6–0.25 μm). After each polishing treatment, the sample was washed in methanol. After insertion into UHV, the surface was prepared by sputter–annealing treatments. Each sputter used Ar^+ for 30 minutes, with an average drain current recorded as 6.5 μA. Each anneal lasted 2 hours at 900 K. Surface ordering and cleanliness was monitored by LEED and STM, where the diffraction pattern was indexed with respect to the clean Cu(111) surface, measured by the same LEED optics, at the same electron energy.

For the C_{60} experiments, the molecules were evaporated in–situ using a Pyrex tube filled with the powdered C_{60}, with a tungsten filament tightly wound around the tube. During deposition, the substrate was held at room temperature (300 K).

5.3 Results

5.3.1 Clean bulk–terminated 2–fold *i*–Al–Pd–Mn surface

LEED

The termination of the 2–fold *i*–Al–Pd–Mn surface (i.e. bulk–truncated, reconstruction) can be found by indexing its diffraction pattern with respect to the six bulk reciprocal vectors discussed in section 2.3. The spatial distribution of the projected vectors is given in Figure 2.5. Similarly, the lengths of the vectors in the 2–fold plane can be calculated by the projected lengths of these bulk reciprocal vectors onto the 2–fold orientation, where each length is dependent on the angle of projection. If the reciprocal space vector length of a diffraction spot is equal to the corresponding projected surface vector (including multiples and τ–scaled values), then the surface can be considered to be bulk–terminated.

Figure 5.3(a) is a LEED pattern taken from the clean surface of the 2-fold Al-Pd-Mn quasicrystal. It shows intense diffraction spots aligned along two perpendicular high symmetry directions. Spot positions along the 2–fold axes are τ–scaled, as evidenced by the vector lengths of two successive spots, a = 1.41 ± 0.03 Å^{-1} and b = 2.25 ± 0.09 Å^{-1} giving a ratio of b/a = 1.6 ± 0.1. Figure 5.3(b) shows the same LEED pattern, decorated

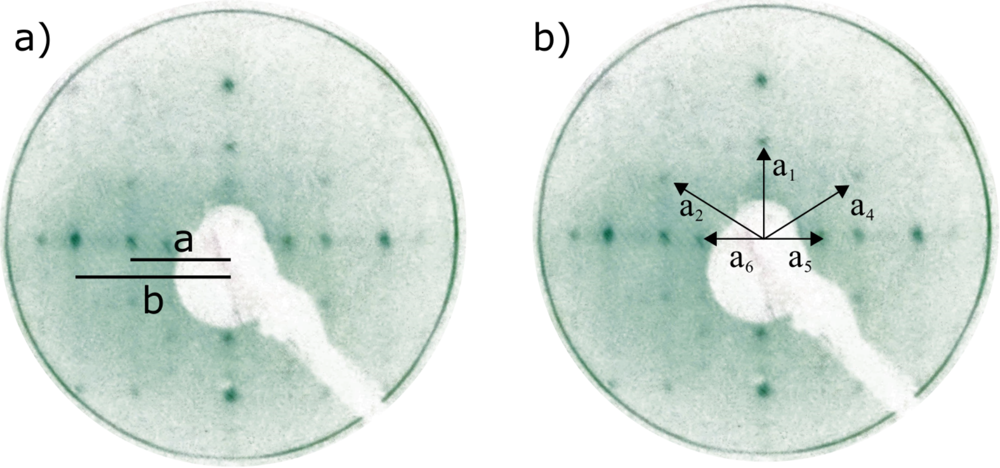

Figure 5.3: **2–fold *i*–Al–Pd–Mn LEED pattern:** **(a)** Diffraction pattern (60 eV) from the 2–fold *i*–Al–Pd–Mn surface. High intensity spots are highlighted in one direction by lengths a and b, where $b = \tau a$. **(b)** The 2–fold projected vectors from Figure 2.5 overlaid onto the pattern, showing spots of high intensity along high–symmetry directions.

with the projected vectors from Figure 2.5. Each vector points to a high intensity spot.

The projected vector lengths are calculated as: $\mathbf{a}_1 = \mathbf{a}_B\cos(\alpha)$, $\mathbf{a}_2 = \mathbf{a}_B\cos(18°)$, and $\boldsymbol{a}_6 = \boldsymbol{a}_B\sin(\alpha)$, where $\cot^{-1}\alpha = \tau$, and $\mathbf{a}_B = 1.04$ Å^{-1}, the bulk (i.e. non–projected) reciprocal vector corresponding to the 'physical space projection of the 6–D periodic reciprocal lattice of $1/\mathbf{a}$ lattice constant' [5]. Vectors $\mathbf{a}_4$ and $\mathbf{a}_5$ are mirror symmetrical to $\mathbf{a}_2$ and $\mathbf{a}_6$ respectively. Not shown is $\mathbf{a}_3$, which is τ deflated from $\mathbf{a}_1$. The vector length of spot a in Figure 5.3(a) corresponds to $\tau\times\mathbf{a}_6 = 1.42$ Å^{-1}. Thus, the surface is consistent with a bulk truncation, as reported [131–133].

STM of the clean surface

STM images of the clean surface shows similar features to those previously discussed [132, 133]. A step–terrace morphology is observed, with step heights forming Fibonacci chain segments, where $S = 0.26 \pm 0.02$ nm, and $L = 0.39 \pm 0.03$ nm. Figure 5.4(a) shows an atomically–resolved STM scan of the surface. Highlighted are two rectangles with edge length ratios of 1:τ^n connecting bright protrusions (e.g. rectangle 2: 0.48×2.0 nm^2). Rows (on top of which the bright protrusions sit) are marked by a Fibonacci chain, where $S = 1.25 \pm 0.02$ nm, and $L = 2.02 \pm 0.02$ nm. The rows and troughs of the surface lead to a root–mean–squared (RMS) roughness of 0.046 ± 0.004 nm. An FFT of Figure 5.4(a) shows a set of spots which are τ–scaled in two orthogonal directions, Figure 5.4(b). Labelled in one direction are τ–scaled spots of high intensity. Note that in the orthogonal direction spots at equivalent positions are reduced in intensity, a consequence of the 2–fold symmetry of the surface – this shall be discussed in detail later. Each of these observations is consistent with the STM scans shown in Figure 5.1 [132, 133].

The bright protrusions can be used as a rudimentary motif in analogy to the bright flower or dark star motifs from the 5–fold surface. They are distributed in two orthogonal directions, parallel and perpendicular to the row orientation. Sets of protrusions parallel to the rows can be separated by segments of a Fibonacci chain, whose length–scale is τ–inflated to the perpendicular row separation, so that $S_{||} = L_{\perp}$. These two (τ–related) length–scales are also a consequence of the two–fold symmetry of the surface, similar to the ratio of spots b and a in Figure 5.3(a), or the ratio of $\mathbf{a}_1$ to $\mathbf{a}_6$ in Figure 5.3(b). Occasionally, τ–deflated positions are also observed, so that $S_{||}/\tau = S_{\perp}$. Figure 5.4(c) shows an enhanced area of Figure 5.4(a), highlighting three sets of protrusions, with their relationship to the row separation marked. Pairings of the spots can build 1:τ^n edge length

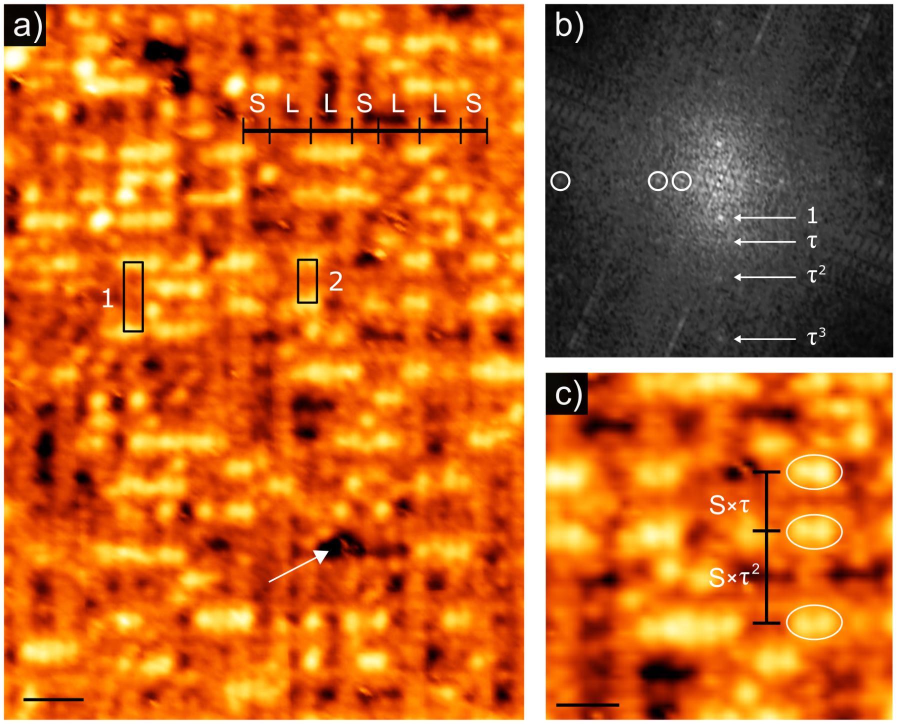

Figure 5.4: **STM from 2–fold *i*–Al–Pd–Mn:** **(a)** STM image (V_b = 1000 mV, I_t = 0.217 nA) of the clean 2–fold *i*–Al–Pd–Mn surface. Highlighted are two rectangles formed by bright protrusions, with edge length ratios of 1:τ^n. A Fibonacci chain separates rows. Scale bar represents 3 nm. **(b)** The FFT of **(a)**. Spots are highlighted in two orthogonal directions, with τ–scaled separations. **(c)** An enhanced view from **(a)**, showing bright protrusions separated by a τ–inflated length scale Fibonacci chain compared to the rows. Scale bar represents 2 nm.

rectangles. The protrusions are composed of two bright spots, forming a dimer.

The dimers and overall surface structure can be understood with respect to a model proposed by Boudard et al. [36,135]. Figure 5.5(a) shows two closely separated planes from the Boudard model (Δz = 0.092 nm). Typically, single dense atomic planes separated by observed step heights can be considered as surface terminations [96]. Here, the collective density of the two planes is equivalent to a single dense plane. Blue atoms are Al, yellow are Pd, and red are Mn, where the Mn atoms are the centres of the pseudo–Mackay clusters [50]. The larger atoms are the top surface plane. A side view of the planes shows their height difference, and relative composition (i.e. no Mn in the sub–surface plane).

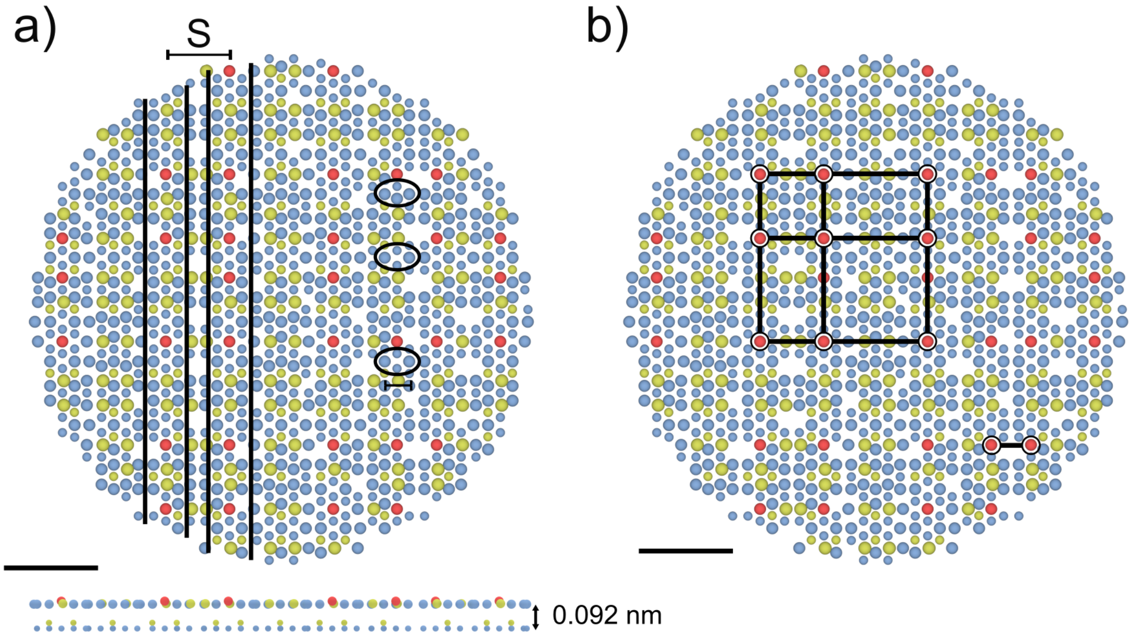

Figure 5.5: **Model of the 2–fold *i*–Al–Pd–Mn surface:** **(a)** *Top:* Surface model consisting of two closely separated atomic planes. The top plane has enlarged atoms compared to the bottom plane. Blue atoms are Al, yellow are Pd, and Mn are red. Dimers of Al atoms are highlighted. *Bottom:* The separation of planes as viewed perpendicularly to the surface. **(b)** Same as **(a)**, but with Fibonacci square grid tiles linking Mn atoms together. Here, S =1.26 nm, L = 2.04 nm. A τ–deflated Mn pair is marked. Scale bars represent 2nm.

Highlighted by circles in Figure 5.5(a) are top–layer Al atoms which are separated by 0.484 nm. This distance fits very well with the intra–dimer separation measured by STM (0.49 ± 0.02 nm). Likewise, the separation of the planes, 0.092 nm, fits with the measured height of the dimers above the rows (0.089 ± 0.004 nm). Rows formed by surface and sub–surface atoms are marked by parallel lines, upon which Al dimers sit. The model rows can be separated by a Fibonacci sequence of S =1.26 nm, L = 2.04 nm, again consistent with the row separation measured by STM (an S length is marked on Figure 5.5(a)). Finally, the height difference between the protrusions and the darkest features, one of which is highlighted by an arrow in Figure 5.4(a), is 0.25 ± 0.02 nm. In the model, the distance between the top layer and the plane below the sub–surface layer is 0.24 nm, an excellent fit. Therefore, the morphology of the surface can be explained by a partial desorption of the top surface layer, leaving behind Al dimers which sit atop the Al–dense rows. This matches with the missing row theory expressed in [133]. In addition, calculations suggest that Al/Mn atoms contribute to bright STM contrast within the i–Al–Pd–Mn system [62]. Furthermore, there is a precedent of constituents from a partially desorbed surface layer exhibiting morphology indicative of the surface model or symmetry, for example, in the ξ'–Al–Pd–Mn approximant [136]. Here, STM showed two planes on the pseudo–10–fold surface, where the top layer was partially desorbed, leaving groups of atoms sitting on top of the substrate. Isolating these groups of atoms and taking an FFT from them reproduced the pseudo–10–fold symmetry of the orientation [136].

As a result of the model planes selected, there is a very sparse Mn distribution in the top surface layer. The Mn atoms can be linked by a Fibonacci square grid, as shown in Figure 5.5(b). The length–scale of the grid is the same as the row separation observed in the model/by STM i.e. $S = 1.26$ nm, $L = 2.04$ nm. Occasionally, τ–deflated positions occur (highlighted in Figure 5.5(b)), appearing to break long–range 4–fold symmetry.

5.3.2 Quasicrystalline C_{60}

Dosing the 2–fold i–Al–Pd–Mn surface with C_{60} produces a quasicrystalline network, with orthogonal chains of C_{60} separated by Fibonacci sequences with identical length scales in both directions. Figure 5.6(a) shows an STM image with segments connecting C_{60} molecules – here, S = 1.26 nm and L = 2.04 nm. The majority of molecules therefore sit at the vertices of a Fibonacci square grid, as shown in Figure 5.6(b). The occupation of the vertices of the prescribed grid is approximately 70 %. The remaining molecules which are not described by this grid can be labelled by a τ–deflated grid, a section of which is overlaid on top of the original, in white. Closely separated C_{60} molecules at consecutive τ–deflated positions appear squashed, as their smallest separation is $S/\tau = 0.77$ nm, smaller than the van der Waals diameter of individual molecules. These positions and their steric interactions will be discussed in detail later.

Fast Fourier transforms

To assess the degree of order of the adsorbed molecular film, an FFT has been taken from Figure 5.6, where the substrate has been filtered out so that only the C_{60} molecules are visible. Figure 5.7(a) shows the FFT, which displays high intensity spots along two orthogonal directions. First and second order spots are highlighted at the vertices of two

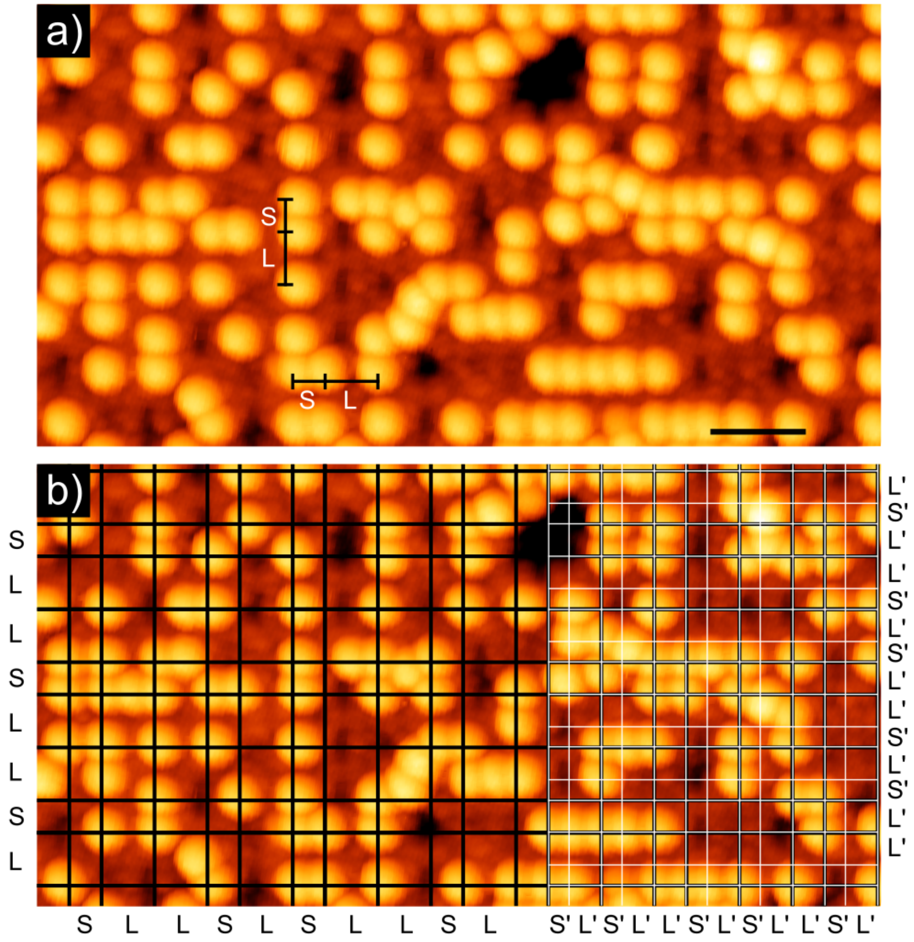

Figure 5.6: **C_{60} on 2–fold i–Al–Pd–Mn:** **(a)** STM image (V_b = -700 mV, I_t = 0.217 nA) showing C_{60} arranged quasiperiodically on the 2–fold i–Al–Pd–Mn surface. Segments of Fibonacci chains are marked in two orthogonal directions, linking individual molecules. Here, $S = 1.26$ nm, $L = 2.04$ nm. Scale bar represents 4 nm. **(b)** Image **(a)**, with a Fibonacci square grid overlaid, with segments labelled in each direction. Again, $S = 1.26$ nm, $L = 2.04$ nm. On the right–hand side, a τ–deflated grid is overlaid on top in white.

concentric τ–scaled squares. Two equivalent vertices of each square are highlighted in pink and yellow respectively. The length–scales of the k–vectors pointing to these spots correspond to the values of S and L from the C_{60} grid. The high intensity, τ–scaled nature of the spots indicates a quasiperiodic film has been produced. As expected, the spots can form a Fibonacci square grid in reciprocal space.

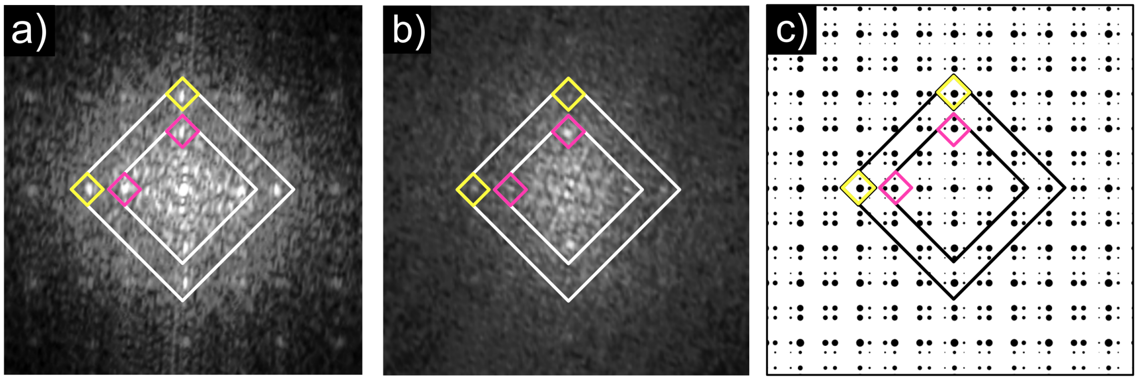

Figure 5.7: **Comparison of FFTs:** **(a)** An enhanced view of the FFT from the clean 2–fold i–Al–Pd–Mn surface (Figure 5.4((b)). Highlighted in white are τ–scaled squares. Small pink and yellow squares highlight spots at equal k–vectors at two corners of each white square. **(b)** FFT taken from the C_{60} contribution to Figure 5.6(a). Spots are labelled as in **(a)**. The scales of **(a)** and **(b)** are equal in k–space. **(c)** FFT calculated from a Fibonacci square grid. Spots are labelled as in **(a, b)**. Scale is arbitrary.

As the Fibonacci square grid exhibits 4–fold symmetry, it is pertinent to compare the rotational symmetries of the film and the 2–fold symmetric substrate. Figure 5.7(b) shows the FFT from the clean surface, where both Figure 5.7(a, b) are at the same length–scale. The high intensity spots of the surface FFT therefore correspond to the length–scale of the row separations, or S and L of the C_{60} grid. Figure 5.7(b) has been annotated similarly to the FFT of the C_{60} grid, with τ–scaled squares. The rotational symmetries of these two transforms can be determined by the ratio of the intensity of spots at equal k–vector lengths in the two primary axes i.e. pink/pink or yellow/yellow. A 2–fold FFT would exhibit a ratio above or below 1 for equivalent spots [133], whereas a 4–fold FFT would have a ratio of exactly 1. The intensity of each highlighted spot, and thus their ratios, has been calculated by integrating the pixel intensity around the local spot area. For the C_{60} film, Figure 5.7(a), the ratio is 1.03 ± 0.01. For the clean surface, Figure 5.7(b), the ratio is 1.27 $\pm$ 0.01. Hence, the FFT from the molecular film shows 4–fold symmetry, commensurate with a Fibonacci square grid. As the k–vector length–scale is equal in both FFTs, this difference in intensity indicates that the molecules are highlighting surface constituents with a distribution not observed in the clean STM image.

For further comparison, Figure 5.7(c) is a Fourier transform of a Fibonacci square grid of arbitrary length. Here, the positions and intensities of the spots are calculated using an orthogonal superposition of Fourier transforms of cut–and–projected 1–D Fibonacci chains, a method set out in [21], utilising the Fourier transform calculations described in Chapter 2. The FFT is decorated as in Figure 5.7(a, b). The intensities of spots at equal k–vector lengths is equal, as expected.

Autocorrelation functions

The long–range order of the film in real space can also be characterized by taking the autocorrelation function of the STM data. Again, the contribution from the substrate has been removed, so that only the C_{60} network is considered. Figure 5.8(a) shows the function of the data in Figure 5.6(a), with a Fibonacci square grid overlaid, where $S =$ 1.26 nm, $L = 2.04$ nm. Spots of high intensity intersect with the vertices of the grid. The streak–like behaviour of local areas of the function is attributed to the nature of the STM scan (i.e. the slow scan direction is parallel to the streak direction). A deformed square is also highlighted, attributed to the C_{60} molecules at τ–deflated positions. Here, either steric interactions induce a displacement (or squashing, as previously mentioned), or, inverted Fibonacci chain segments created by τ–deflated C_{60} positions create a distortion. Both points will be discussed later.

Figure 5.8(b) shows an autocorrelation function taken from a 50×50 nm^2 Fibonacci square grid model where $S = 1.26$ nm, $L = 2.04$ nm. Here, point–like objects decorate each vertex of the grid. The autocorrelation function shows high intensity spots, with a square grid overlaid matching the dimensions of the experimental grid in Figure 5.8(a). The excellent fit between model and experimental functions confirms the validity of the C_{60} Fibonacci grid model.

The τ–deflated C_{60} vertices in Figure 5.6(a) do not contribute extra sets of spots to the experimental autocorrelation function, and are therefore at a low occupancy compared to the vertices of the 'original' grid. This is revealed by the close match between the two autocorrelation functions, as the model function does not consider any τ–deflated positions. Indeed, as measured by STM, only ~8% of the C_{60} molecules sit at vertices solely described by the τ–deflated grid (i.e. at vertices not shared between the original and τ–deflated sites). This is contrary to what is expected from the relationship between a Fibonacci grid and its τ–deflated cousin: a perfect τ–deflated Fibonacci grid has τ^2 the number of vertices than the original grid[1]. The relative number of points in a τ–deflated grid that do not overlap

---

[1] If a chain of $LSLLS$ is deflated to $LSLLSLSL$, the relative number of segments produced is $\sim \tau$.

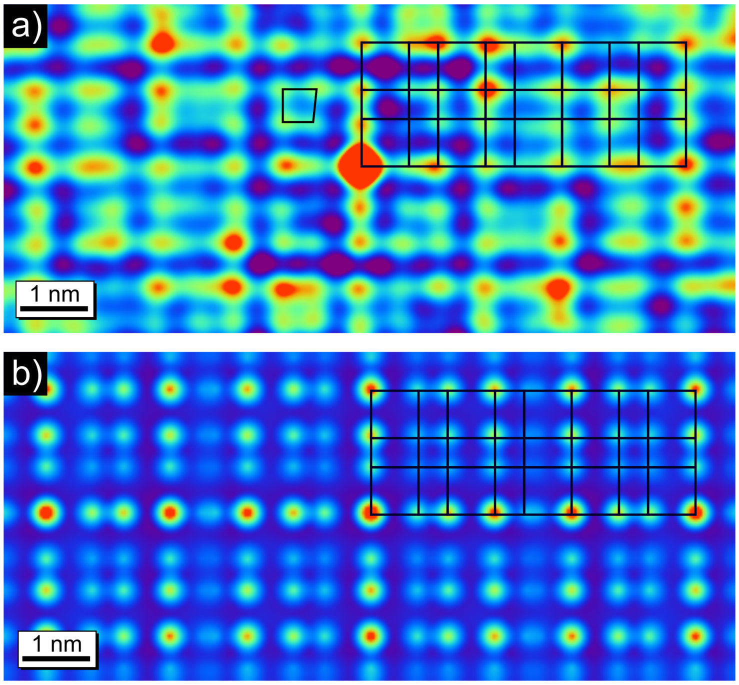

Figure 5.8: **Autocorrelation function of C_{60}:** **(a)** The autocorrelation function from the molecules in Figure 5.6(a), where the substrate contribution has been removed. A Fibonacci square grid is overlaid, with $S = 1.26$ nm, $L = 2.04$ nm. A deformed square is also highlighted, which originates from steric contributions displacing S/τ C_{60} molecules. **(b)** A model autocorrelation function, taken from a perfectly decorate Fibonacci square grid, again with $S = 1.26$ nm, $L = 2.04$ nm. An equivalent grid to **(a)** links spots of high intensity.

with the original grid is thus $\tau^2 - 1 = \tau$, or, τ times as many points as the original grid. This is in stark contrast to the number of vertices occupied experimentally. Therefore, there is little to no spatial contribution (aside from the steric deformations) from the τ–deflated positions observed in the autocorrelation function. The same may hold for the FFT in Figure 5.7(a). These sites may break the 4–fold symmetry of the film over an infinitely large patch, but are at low enough occupancy so as to be considered as defects of the grid, rather than creating a 2–fold structure. As previously mentioned, a suitable physical decoration of the square grid could break its 4–fold symmetry.

The measurements of the grid directly from the STM image and the analysis of the

---

Extending this to orthogonal chains in 2–D gives τ^2.

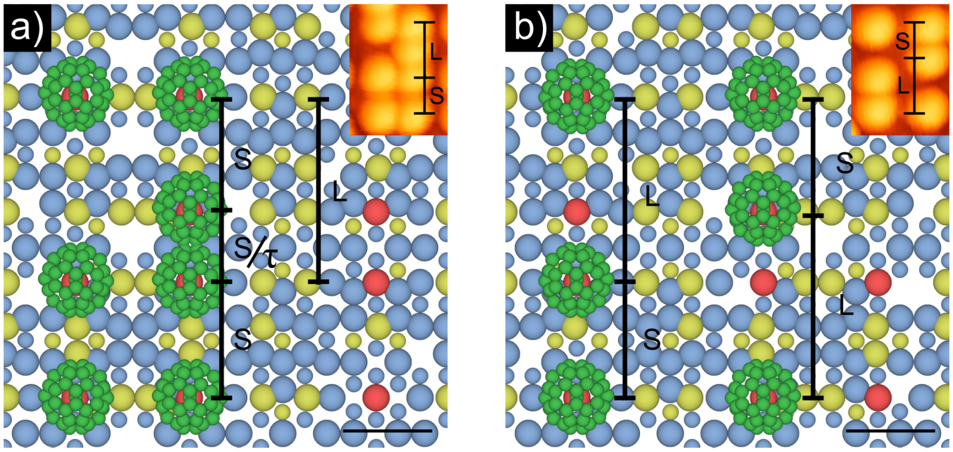

Figure 5.9: **C_{60} model and experimental motifs:** **(a)** A model schematic of C_{60} (green) decorated Mn atoms producing $S \times S$ and $S \times L$ tiles. A τ–deflated position is also occupied. Inset is the corresponding motif as seen by STM in Figure 5.6. **(b)** Inverted LS and SL chain segments of C_{60} decorated Mn atoms. Vacant Mn atoms are at τ–deflated positions. Inset is the corresponding motif as seen by STM in Figure 5.6. C_{60} orientations are arbitrary.

FFT patterns and autocorrelation functions all point to an adsorption network with a Fibonacci square grid distribution that exhibits a minimal amount of τ–deflated positions. As introduced with the surface model in Figure 5.5, we see that Mn atoms in the surface plane match these attributes exactly, whilst Al and Pd adsorption sites are too densely distributed, and would produce a disordered film. Comparisons made below between model Mn sites and experimental C_{60} motifs also confirm this theory. Furthermore, previous studies have shown that Mn can act as active adsorption sites on QC surfaces [137].

Models of C_{60} motifs

C_{60} adsorption sites on the surface can be rationalised with reference to Mn atomic positions. The insets in Figure 5.9(a, b) show a couple of C_{60} motifs taken from Figure 5.6. The main figures show models of these motifs using the model surface structure. Figure 5.9(a) shows $S \times S$ and $S \times L$ tiles, with a τ–deflated position also occupied. As evidenced by the STM inset, the C_{60} at the S/τ position is deformed, or slightly displaced by this small separation presumably due to the steric interaction between the neighbouring molecules. Such distortions will then translate into the autocorrelation function, as previously discussed.

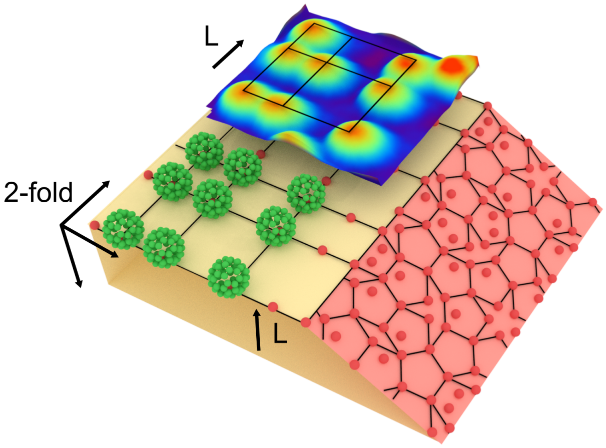

Figure 5.10: **2–fold and 5–fold model comparison:** The relationship between the 2–fold and 5–fold Mn distribution in i–Al–Pd–Mn is shown. The 5–fold orientation is coloured pink, with Mn atoms joined by a Penrose P1 tiling of edge length 0.77 nm. The 2–fold orientation is cream, with Mn atoms joined by a Fibonacci square grid of $S = 1.26$ nm, $L = 2.04$ nm. Model C_{60} molecules decorate a patch of the grid, and a 3–D STM image is overlaid, showing the occupancy of the square grid tiles.

However, the S/τ positions can be occupied without steric distortion. Figure 5.9(b) shows two C_{60} occupied segments of a Fibonacci chain which are inverted i.e. LS and SL. The inversion occurs due to the particular occupation of the local τ–deflated Mn positions. Again, this may translate into a distortion of the autocorrelation function of the STM image, as two separate mirror–inverted Fibonacci chains are represented here. Combined with the STM, FFT, and autocorrelation analysis, the fit to these model motifs indicates that Mn atoms at the surface provide a sparse adsorption network for the C_{60} to grow a Fibonacci square grid. Furthermore, as C_{60} is an electron acceptor [138], and Mn an electron donor [105], there is also an electronic motivation for this adsorption scheme. Additionally, as previous mentioned, the k–vector length–scale of the FFTs in Figures 5.7(a, b) are equal, showing spots of high intensity at real space lengths indicative of the either the C_{60} grid or the row separation. The extra spots (and increased intensity of shared spots) of the molecular FFT therefore highlight surface constituents with a distribution not observed in the clean STM image, i.e. the Mn network.

The relationship between the 5–fold and 2–fold Mn distribution in i–Al–Pd–Mn is shown in Figure 5.10, where a slab of the model structure is shown with only Mn atoms.

The 5–fold orientation (pink) is linked with a Penrose P1 tiling, and the 2–fold (cream) by a Fibonacci square grid. For comparison, model C_{60} molecules decorate a section of the grid, and a 3–D STM image is overlaid of the same tiles. The L lengths labelled correspond to the size of the grid, and to a collection of step heights between terraces, both 2.04 nm.

5.3.3 Other surface phases observed on the clean surface

During investigation of the clean quasicrystal surface, several other structural phases were observed. Previously, an orthorhombic domain was described in this system [132]. Preparation conditions and sputtered QC surfaces lead to similar observations on the 5–fold surface [139, 140]. The phases discussed here can be considered either as facets of the 2–fold surface, or as a separate phase produced by impurities. Each of these structural differences were observed after using the same preparation conditions as to obtain the clean quasicrystal surfaces. The domain sizes of each phase were on the order of 100 nm or less, unsuitable for conducting elemental analysis of their constituents (via XPS, for example).

Figure 5.11(a) shows an STM scan which displays aperiodically spaced, triangular protrusions. Vertices of these triangles can be linked with a Fibonacci chain of $S = 0.43 \pm 0.04$ nm, $L = 0.76 \pm 0.05$ nm, as labelled. This L value corresponds to the edge length of the Penrose tiling which decorates the Mn distribution in the 5–fold surface, or the S/τ separation of Mn atoms in the 2–fold surface. Therefore, it is suggested that this domain is a facet along the 3–fold orientation, with a Mn dense surface forming a quasicrystalline arrangement of triangles. A model motif of Mn has been overlaid, obtained from the same model used to describe the 2–fold surface. The fit of the model suggests a partially desorbed surface layer.

Figure 5.11(b) shows a periodic phase, with a unit cell of $a = 0.64 \pm 0.02$ nm, $b = 0.62 \pm 0.02$ nm, highlighted. Figure 5.11(c) is a rectangular phase, with a unit cell of $a = 0.56 \pm 0.08$ nm, $b = 0.42 \pm 0.02$ nm, also highlighted. Both surface domains can be explained by planes of the body–centred cubic β–Al–Pd phase, which has a lattice constant of $0.304 - 0.306$ nm [141]. As previously mentioned in section 3.2.1, crystalline and quasicrystalline structures may have high symmetry axes which coincide. Metastable films of the β–Al–Pd phase have been observed at the i–Al–Pd–Mn surface after sputtering of high–symmetry orientations [136, 140]. Considering this, the phases shown in Figure 5.11(b, c) are tentatively identified as the [100] and [112] directions of the β–Al–Pd phase. Representations of each model unit cell are overlaid on each image. For Figure 5.11(b),

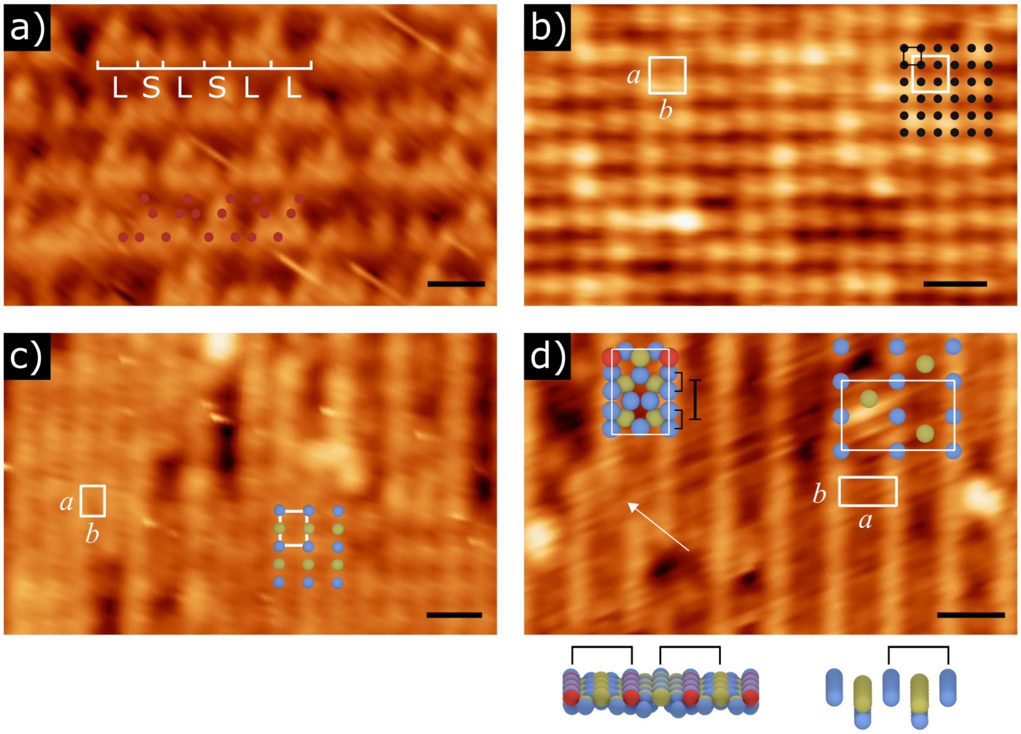

Figure 5.11: **Different surface domains:** **(a)** 3–fold facet with a Fibonacci sequence indicated. A model Mn distribution is overlaid. **(b–d)** shows unit cells with a and b values in the text. Each also shows the relationship between model structures and those observed by STM. Scale bars represent 1 nm. **(b)** The β–Al–Pd(100) surface. **(c)** The β–Al–Pd(112) surface. **(d)** Either the 2–fold surface of the ξ'–Al–Pd–Mn approximant (left model), or the β'–Al–Pd($\bar{1}0\bar{1}$) surface (right model). An arrow indicates a row 'flip'. Underneath are side views for each model showing how the row structure is formed.

the β–Al–Pd(100) unit cell would be cubic, with $a = b = 0.304$–0.306 nm. It is presumed that the unit cell measured by STM (approximately twice the model structure) is due to a lack of atomic resolution, and that clusters of atoms are represented by each protrusion. Indeed, there is a good match (± 3%) between twice the model value and those measured by STM. The β–Al–Pd(112) unit cell is $a = 0.528$ nm, $b = 0.431$ nm. Here, there is a good match with b measured in Figure 5.11(c): ± 3 %. If only either Al or Pd are resolved, the measurement of a is doubled compared to the model. Considering this, the model and experimental values match within ± 6%.

Finally, Figure 5.11(d) displays another periodic phase, characterized by bright and dark rows. The unit cell is measured as: $a_{STM} = 0.85 \pm 0.01$ nm, $b_{STM} = 0.45 \pm 0.03$nm as labelled. A defect or dislocated row is highlighted by an arrow. This phase can be tentatively identified as either the 2–fold orientation of the ξ'–Al–Pd–Mn approximant (i.e. the ξ'–Al–Pd–Mn(100) surface), or the β'–Al–Pd($\bar{1}0\bar{1}$) surface.

The ξ'–Al–Pd–Mn approximant unit cell is given as: $a_{\xi'} = 2.35$ nm, $b_{\xi'} = 1.66$ nm, $c_{\xi'} = 1.23$ nm [36]. Here, the 2–fold orientation is perpendicular to a, giving a surface unit cell of $b_{\xi'} = 1.66$ nm, $c_{\xi'} = 1.23$ nm. When compared to STM measurements, $a_{STM} = b_{\xi'}/2$ ($\pm 3\%$) and $b_{STM} = c_{\xi'}/3$ ($\pm 9\%$). A model has been overlaid on Figure 5.11(d, left) for comparison, with a unit cell highlighted in white. The comparatively large difference between b_{STM} and $c_{\xi'}$ can be considered as a modulation of the separations of pairs of atoms along each row (an example is highlighted), giving an average value that roughly corresponds to $c_{\xi'}/3$. Here, it is presumed that the two atoms are resolved as one protrusion. For example, if we take the Mn–containing row, the average separation of atom pairs is 0.50 ± 0.06 nm, within error of the value of b_{STM}.

Conversely, the β'–Al–Pd phase has a unit cell $a_{\beta'} = 1.57$ nm, $c_{\beta'} = 0.53$ nm [142]. The [$\bar{1}0\bar{1}$] direction consists of mixed planes of Al/Pd separated by planes of either pure Al or pure Pd, depending on stoichiometry. The mixed plane creates a row structure of either Al or Pd atoms that forms a surface rectangular unit of $b_{\beta'(\bar{1}0\bar{1})} \times a_{\beta'(\bar{1}0\bar{1})} = 0.48 \times 0.78$ nm^2, so that $a_{STM} = a_{\beta'(\bar{1}0\bar{1})}$ ($\pm 6\%$) and $b_{STM} = b_{\beta'(\bar{1}0\bar{1})}$ ($\pm 8\%$). A model unit cell has been overlaid on Figure 5.11(d, right), where Al atoms have been arbitrarily chosen as the bright row constituents.

The average height corrugation between the dark and bright rows is 0.5 ± 0.1 Å. This can be explained by selecting a plane, or set of planes, from the ξ'–Al–Pd–Mn approximant to produce a row–like structure in which one set of rows desorbs preferentially, or, are not detected by STM. One such set of planes is shown underneath Figure 5.11(d, left), where Mn or Al rich rows are labelled. The corrugation could simply be a slight relaxation of the β'–Al–Pd($\bar{1}0\bar{1}$) surface, where rows of one atom type relax in z, shown underneath Figure 5.11(d, right).

5.3.4 C_{60} adsorption on the different surface phases

Adsorption of C_{60} was observed on the ξ'–Al–Pd–Mn/β'–Al–Pd and β–Al–Pd phases. Figure 5.12(a) shows a low coverage STM image of two phases of C_{60} on the ξ'–Al–Pd–Mn/ β'–Al–Pd surface i.e. the surface phase detected in Figure 5.11(d). Labelled are the unit

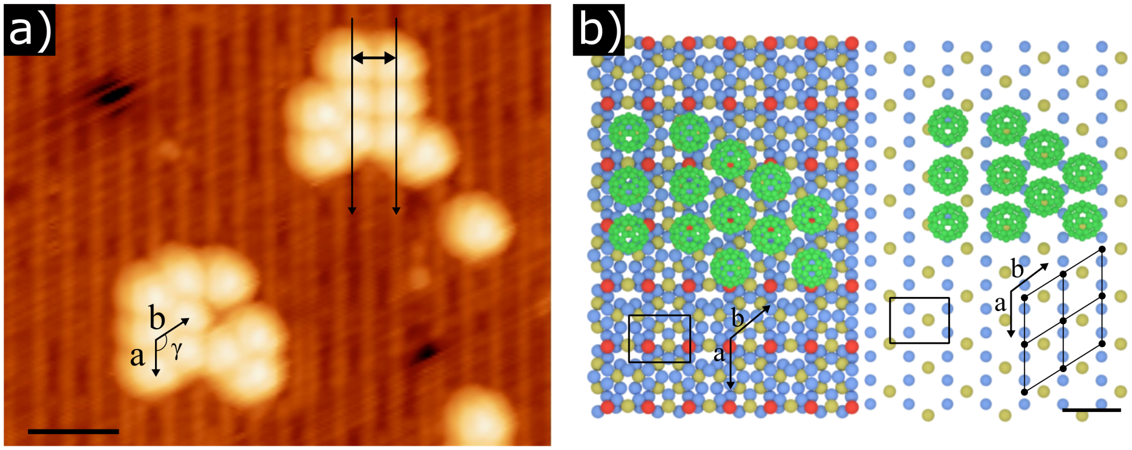

Figure 5.12: **C_{60} on periodic phases: (a)** Two phases of C_{60} structure are observed on the ξ'–Al–Pd–Mn/β'–Al–Pd surface. The unit cell vectors of a honeycomb structure are indicated as a and b. A parallel row structure is also highlighted. Scale bar represents 2.0 nm. **(b)** Model structure of the C_{60} phases in **(a)** on ξ'–Al–Pd–Mn (left) and β'–Al–Pd (right). Adsorption sites are marked by C_{60}, or unit vectors. A C_{60} lattice is marked for the β'–Al–Pd($\bar{1}0\bar{1}$) surface phase. Scale bar represents 0.5 nm.

cell vectors of one phase, a honeycomb–structured island, with $a_{C_{60}} = 1.00 \pm 0.07$ nm, $b_{C_{60}} = 1.03 \pm 0.05$ nm, and $\gamma = 123 \pm 2°$. Each C_{60} appears to sit in–line with the row structure, either directly on top of bright rows or between them. Also marked as a second phase are parallel rows of C_{60} which are separated by 1.25 ± 0.05 nm, approximately $0.75 \times b_{\xi'}$, or, $1.5 \times a_{\beta'}$. The separations along the parallel C_{60} chains are 0.98 ± 0.02 nm. A switch of bright/dark substrate rows is observed between the start and end of rows of C_{60}, both in its honeycomb and parallel row form. Two arrows are overlaid on the parallel row structure, with the left–hand arrow initially on a bright row, and the right–hand on a dark. At the ends of each arrow, the row structure is switched. This indicates either that C_{60} adsorption induces a row reconstruction, or, that the row switching defect produces an attractive site for C_{60} to nucleate.

Prospective adsorption sites for each C_{60} phase on each surface structure are shown in Figure 5.12(b). For each surface model, the honeycomb phase has been matched so that the C_{60} intersects with the row structure described in Figure 5.11(d). For ξ'–Al–Pd–Mn, the model C_{60} structure has unit cell values of $a = 1.0$ nm, $b = 0.99$ nm, and $\gamma = 123°$, a good fit within error to the experimental values, Figure 5.12(b, left). Here, rows containing Mn have

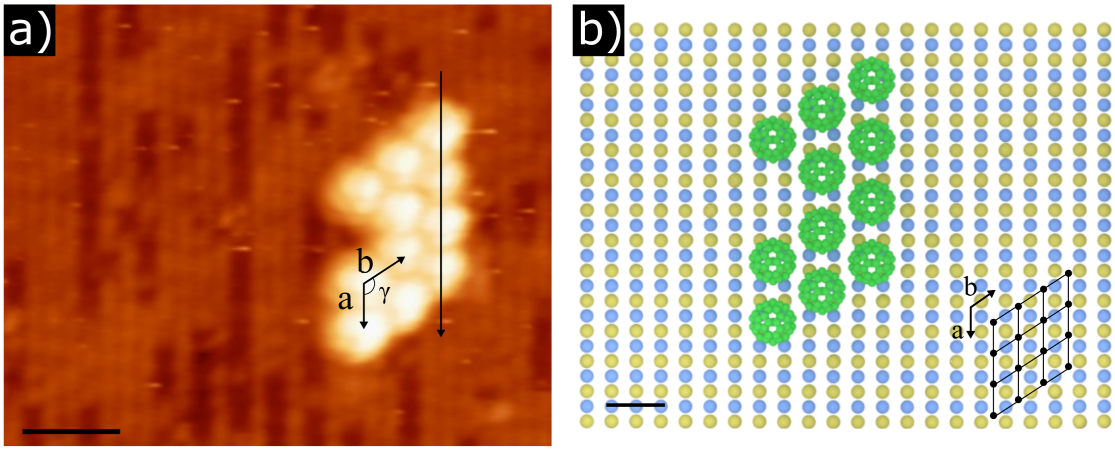

Figure 5.13: **C_{60} on periodic phases:** **(a)** A honeycomb structure of C_{60} on the β–Al–Pd(112) phase. Unit cell vectors are highlighted. Scale bar represents 2 nm. **(b)** Model structure of the C_{60} phase in **a)**. Again adsorption sites are marked by C_{60}. A C_{60} lattice is also shown. Scale bar represents 1 nm.

been chosen arbitrarily as adsorption sites. The lack of templated growth indicates a weak bond to any potential site. Additionally, the imposed constraint of $b_{STM} = c_{\xi'}/3$ creates chemically non–specific adsorption sites in the C_{60} network i.e. the C_{60} can adsorb between any pair of surface atoms along the rows. Likewise, the parallel row C_{60} molecules are speculated to adsorb at chemically non–specific sites, forming rectangles with dimensions 0.95 nm × 1.24 nm, as highlighted.

For β'–Al–Pd, the model honeycomb C_{60} structure has unit cell values of $a = 0.97$ nm, $b = 0.92$ nm, and $\gamma = 122°$, adsorbing at bridge sites in the Al/Pd rows, Figure 5.12(b, right). The parallel structure forms rectangles of 0.97 nm × 1.18 nm, as highlighted. Compared to the C_{60}/ξ'–Al–Pd–Mn model, the match between these values and the experimental measurements is less impressive. However, the geometry of adsorption sites is much more chemically specific. If we presume the surface rows are Al, for example, then C_{60} would adsorb at a bridge site between Al atoms of the rows (honeycomb) or at a Pd site between four Al atoms (parallel), Figure 5.12(b), right.

In either case, it is apparent that intermolecular forces are responsible for the structure of the C_{60} here, as opposed to a strong substrate–molecule bond. In contrast to the quasicrystalline phase, C_{60} is growing in a close–packed structure with a periodicity approximately equal to the Van der Waals diameter, aligned along high symmetry directions (i.e. along the row direction). This behaviour is similar to C_{60} on other non–QC surfaces, as mentioned in Chapter 3. This may explain the lack of chemical specificity or adsorption site ambiguity in the models proposed in Figure 5.12. The parallel row structure in this case may simply be a result of two rotated close–packed C_{60} domains meeting at a common interface.

Figure 5.13(a) shows C_{60} at the β–Al–Pd(112) surface. Here, only a honeycomb structure is observed. Again, unit cell vectors are highlighted, where $a = 0.96 \pm 0.07$ nm, $b = 1.01 \pm 0.04$ nm, and $\gamma = 122 \pm 2°$. Each C_{60} row appears to sit at a bridge site between two substrate rows, as indicated with an arrow. The proposed adsorption sites are shown in Figure 5.13(b), where C_{60} sit between four atoms, two Al, and two Pd. The unit cell of the model structure is $a = 1.06$ nm, $b = 1.01$ nm, and $\gamma = 121.5$, an excellent fit with the experimental values. As with the ξ'–Al–Pd–Mn/β'–Al–Pd C_{60} phases, intermolecular interactions appear to dominate, creating a close–packed C_{60} structure. Again, the proposed adsorption sites are arbitrary, with the only stipulation that the close–packed structure is oriented along the surface row direction.

The difference between these close–packed C_{60} results and those of the Fibonacci square grid C_{60} is, of course, the change in surface structure. The unique nature of the Mn distribution in the quasicrystalline phase provides a network for selective adsorption, whilst the interaction between the C_{60} and non–QC phases is as most common metal surface/C_{60} interfaces.

5.4 Summary

The surface structure of the 2–fold termination of the i–Al–Pd–Mn quasicrystal has been investigated and compared to the model proposed by Boudard et. al. Here, bright dimers at the surface observed by STM are attributed to Al dimers in a surface model consisting of two closely separated planes. The surface plane also displays a sparse Mn distribution with a Fibonacci square grid structure.

C_{60} is found to adsorb exclusively to Mn sites at the 2–fold i–Al–Pd–Mn surface, itself forming a Fibonacci square grid of equal size to the Mn network. This observation leads to a confirmation of the surface model, as well as representing the first measurement of a physical Fibonacci square grid. The observation of such a structure has extended the quasicrystal family beyond the forbidden symmetry systems previously observed. From a general standpoint, this work shows that a distribution of minority constituents in complex metallic alloys can present a unique adsorption landscape. For example, utilising similar networks and choosing the correct molecule could permit the construction of a molecular magnet array of chosen magnetic behaviour. Furthermore, the relative simplicity of the constructed quasilattice opens up a stepping-stone to the understanding of complex phenomena in quasicrystals.

Different surface phases of the system have also been investigated, with a 3–fold aperiodic patch identified as the 3–fold orientation of the i–Al–Pd–Mn system. Several periodic domains were observed, and attempts have been made to identify them with respect to structural models of chemically similar phases. The lack of templated growth of C_{60} on these periodic phases compared to i–Al–Pd–Mn illustrates the different adsorption potentials induced by structurally and chemically related phases which are similar, yet unique.

Chapter 6

3–fold aperiodic tilings

In this chapter, two examples will be given of aperiodic tilings which exhibit 3–fold rotational symmetry, the first such tilings. Their construction and relationship to each other will be discussed. In Chapter 7, one of the tilings will be used to link 3–fold *i*–Ag–In–Yb surface features together. A third tiling derived by a different method is also contained within Appendix A. This work was completed in collaboration with Prof. Uwe Grimm and Dr. Ron Lifshitz, who helped explain the various techniques of creating valid aperiodic tilings (in particular, vertex matching rules and deflation behaviour), as well as assisting with the nomenclature of the field.

6.1 Introduction

Aesthetics has been conjectured as the driving force behind a mathematical mind, as opposed to simply logic [143]. Both share simplicity and brevity as two basic criteria [144]. Additionally, the role of aesthetics has been cited as '(a), motivating the choice of certain problems to solve, (b), guiding the mathematician to discovery, and (c), helping a mathematician decide on the significance of a certain result' [145]. Often, the concept of mathematical beauty is associated with elegant theorems and proofs [146]. However, the ability to convey a mathematical argument in a concise, visually beautiful way can be invaluable. Likewise, its power as an educational (and publicly engaging) tool is important [147].

An excellent example to encapsulate both the aesthetically pleasing and logical arguments are aperiodic tilings. The concept of mapping aperiodicity in two dimensions was briefly introduced in section 2.2. Several examples of tilings were given which fill 2D space completely, yet exhibit non–periodic, long–range order. These can be constructed both using geometric matching/substitution rules, or by projection from higher dimensions. Of particular importance in this thesis is the Penrose tiling, which accomplishes all of the above whilst also being the first to display 5–fold symmetry, an excellent tool for modelling quasicrystals with icosahedral structure. [28]. Penrose himself extolled the virtue of the aesthetically pleasing in his work [27].

It is often commonplace, then, in the analysis of images from either QC surfaces or epitaxial structure to use a relevant rotationally–symmetric tiling. There are examples of pentagonal 5–fold, decagonal 10–fold, and dodecagonal 12–fold systems being decorated with specific tilings to aid their understanding, or to confirm their aperiodic structure [5, 6, 53, 57, 62, 66, 67, 79, 148, 149]. Indeed, highlighted within this work is the 4–fold Fibonacci square grid tiling, linked to the molecular overlayer grown on 2–fold Al–Pd–Mn [21]. Visualizing a tiling with atom–decorated vertices can be a simple way to interpret quasicrystalline structure.

Aperiodic tilings with lower orders of rotational symmetry which may be related to QCs have not been widely explored, as the main focus has been on icosahedral QCs with 5–fold orientation. Certainly, 2–fold, and 3–fold symmetries are hardly unique in crystallography. Here however, a new set of linked aperiodic tilings will be introduced which display 3–fold symmetry. Their construction will be shown by two methods, ranging from purely geometric and aesthetic creations to an inferred hyper–dimensional projection. One of these tilings will be used to re–interpret the clean 3–fold i–Ag–In–Yb surface in Chapter 7.

First, a brief summary of the Penrose tiling will be given to give these results some methodological context.

6.1.1 Penrose Tiling

The first Penrose tiling, the P1, has already been introduced in section 2.2.3, Figure 2.4. His third version, the P3, was created by ‘a little slicing and rejoining’ of the six P1 tiles, so that he ended up with just two – a fat and thin rhombus [28]. The relationship between the P1 and the P3 tilings is shown in Figure 6.1(a).

The first method we consider to build the P3 tiling is substitution/deflation. Figure 6.1(b) shows the rules for deflating the two tiles, where each tile is split into two ‘Robinson’

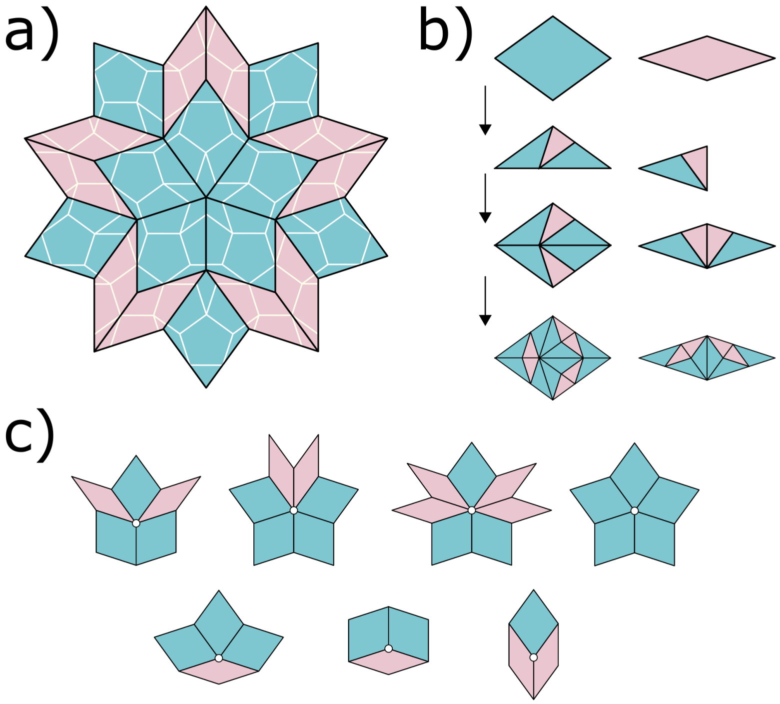

Figure 6.1: **Penrose P1 and P3 tiling:** **(a)** The Penrose P3 tiling (pink and blue tiles), with the P1 tiling overlaid in white. **(b)** The deflation rules for each rhomb of the P3 tiling. Each can be split into two triangles which are then deflated. **(c)** The vertex configurations of the P3 tiling.

triangles (a mutually locally derived tiling [150, 151]) which are then deflated into further triangles. These can then be combined to create a deflated tiling.

The second method is vertex matching, similar to the edge matching rules introduced for the P1 tiling in Figure 2.4. Here instead, a maximum number of configurations for vertices are given. Figure 6.1(c) shows the seven configurations for the P3 tiling. These are sometimes referred to as eight configurations, where the star configuration of the fat rhombs is simply rotated by 36°. Vertex enforcement is a more robust way of building the P3 tiling than using edge matching rules. These rules can be used to build the tiling infinitely, whilst still covering all space and maintaining aperiodicity. Edge matching rules can lead to ‘dead surfaces’, where, through no errors of construction, either empty spaces are created, or, the ‘next step’ to continue the tiling is ambiguous. Therefore, edge matching rules are considered a consequence of vertex enforcement, rather than a method of construction

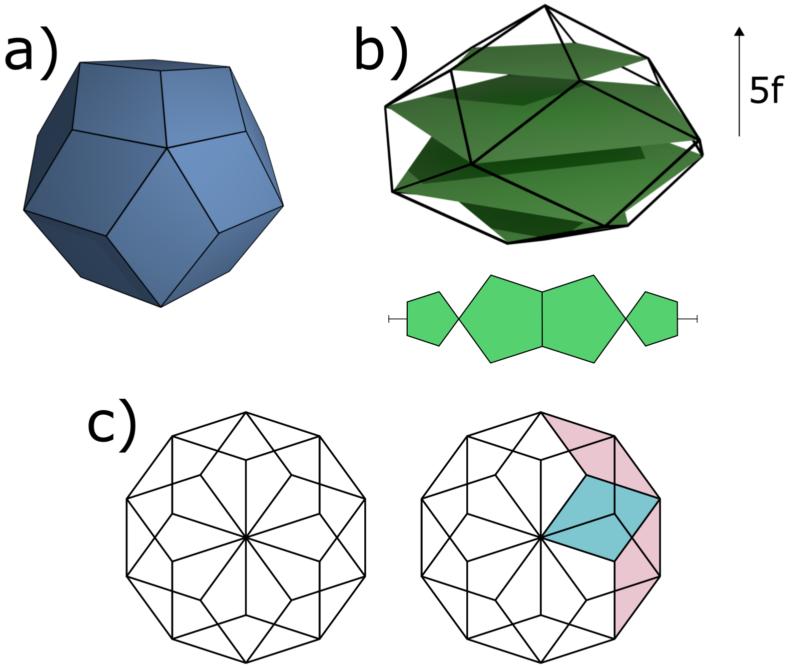

Figure 6.2: **Penrose tiling acceptance window:** **(a)** The rhombic icosahedron. **(b)** The four planes inside of the rhombic icosahedron along the 5–fold direction. The pentagonal planes are shown below. **(c)** The projection of **(a)** along the 5–fold direction. Also shown with P3 tiles.

[20, 31].

The third way of building/creating the P3 tiles is by projecting from higher dimensional space. Analogous to the Fibonacci sequence described in section 2.2, the vertices of the P3 Penrose tiling can be created by projecting a certain 2D surface from 5D space onto a 2 dimensional plane [31, 152, 153]. For the cut–and–project method used to create the Fibonacci sequence, section 2.2, a line is cut through 2D space, with an attached acceptance window. If points fall within this window, they are projected to construct the Fibonacci sequence. Here, the 2D surface in 5D space is analogous to the 1D line. The (multiple) windows which accept the projected points are defined by a 3 dimensional body, which itself is a projection onto 3D perp–space by the unit cell of the 5D lattice. Figure 6.2(a) shows the 3D shape, which is the rhombic icosahedron also used as a constituent of the 3D Penrose tiling. Planes are labelled inside the body in Figure 6.2(b), making four pentagons of either different size or orientation, shown below. These are the acceptance windows for the Penrose tiling.

An interesting coincidence which will be utilised later, is that the projection of the edges of the rhombic icosahedron along its 5–fold orientation produces the P3 tiles. Figure 6.2(c) shows an example of the projection, along with a few constituent P3 tiles.

6.2 Method

Two 3–fold aperiodic tilings will be produced using two different methods. First, a Fibonacci tri–grid is produced, using a similar method to that used to create the Fibonacci square grid. Then, the rhombic icosahedron from Figure 6.2 will be used to infer proto–tiles for a linked tiling.

6.3 Results

Fibonacci tri–grid

The tri–grid tiling is created in a method analogous to the Fibonacci square grid. Here, three sets of Fibonacci sequences are overlaid at relative angles of 120°. Figure 6.3(a) shows such a construction with the axes of 3–fold rotational symmetry passing through the pink circle. To generate the two other examples shown, one set of the three grids is simply shifted by either L or $L+S$ along its relevant axis.

Each have similar tiles: triangles, trapezoids, and shields, shown underneath each. Figure 6.3(c) also has diamonds. The three tri–grids shown are therefore distinct in terms of tile constituents and tile frequency. Their construction is similar to the different types of Penrose tiling created by different cuts through hyperspace which are locally isomorphic [34]. Their difference is best demonstrated by their vertex distribution – Figure 6.4 shows just the vertices of each type, alongside auto–correlation functions taken from each to demonstrate their aperiodicity. High intensity spots which are marked are τ–scaled, as expected.

Using the tiles given by the superposition, one can construct a set of deflation and vertex configuration rules for a given tiling. Figure 6.5 shows an example of such a tiling after six generations of deflations starting from the green triangle. Adjacent are the deflation rules and vertex configurations which enforce particular matching rules. The obvious drawback however are the non–discrete deflation rules – the trapezoid deflating into 4 separate sets of

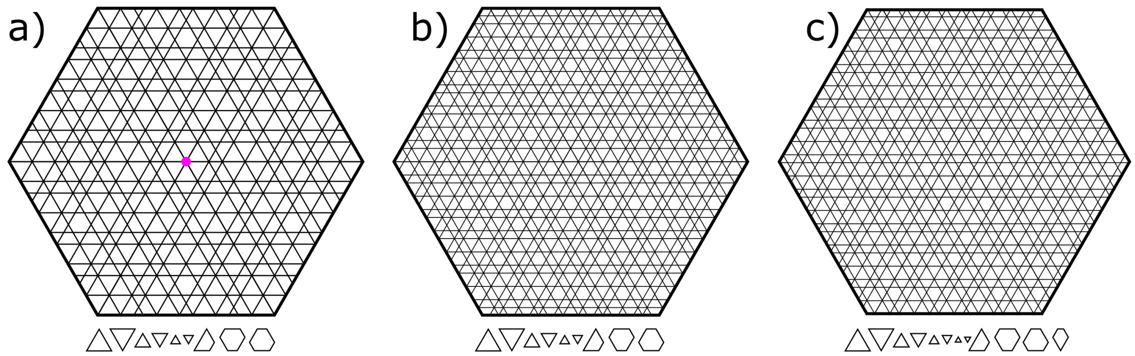

Figure 6.3: **Fibonacci tri–grids:** **(a)** Three Fibonacci sequences are overlaid at 120° relative to each other. A pink circle shows the centre of rotational symmetry. Constituent tiles are below. **(b)** Same as **(a)**, but one set of sequences shifted by L. **(c)** Same as **(a)**, with one set of sequences shifted by L+S.

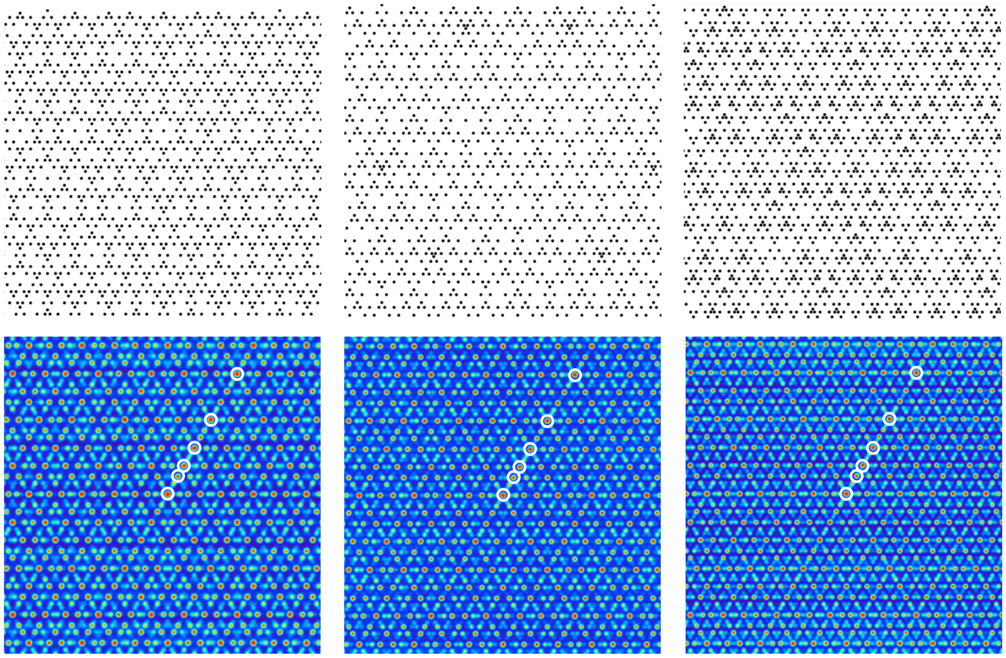

Figure 6.4: **Tri–grid vertices:** The vertices of the three tri–grids generated in Figure 6.3. Below each are the auto–correlation functions taken from each.

tiles is not ideal, for example. This issue could be solved by colouring specific orientations of each tile, but this method increases the number of tiles and unique deflation rules to

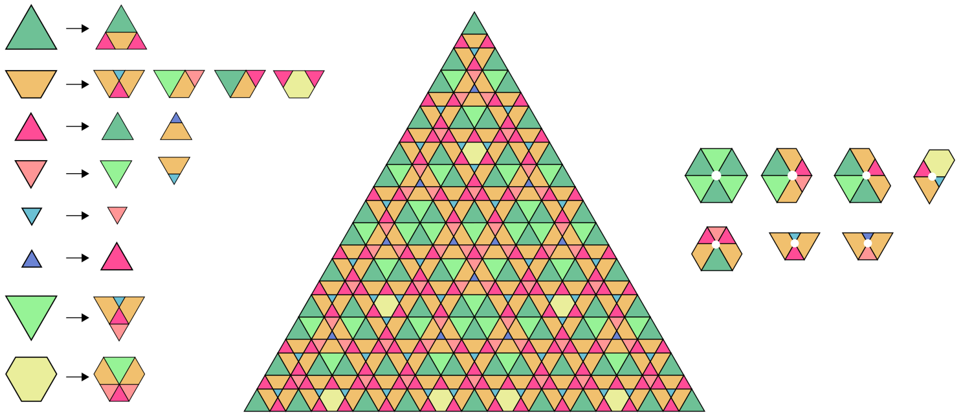

Figure 6.5: **The tri–grid tiling:** Starting with the green triangle, a tri–grid tiling is produced using the deflation rules on the left–hand side, whilst enforcing the vertex configurations on the right–hand side.

a tedious level. However, its 3–fold rotational nature, aperiodicity, and long–range order are guaranteed by its construction using the Fibonacci sequences, and is therefore a good example of a new quasiperiodic tiling which fills all space.

Rhombus tiling

The hyperspace construction of the Penrose tiling has previously been explained. The projection of a 5D hyper–cube onto 3D space gives a rhombic icosahedron, which then gives 4 atomic windows. Any projected vertices of the 5D hypercube which fall within these acceptance windows correspond to vertices of the Penrose P3 tiling. It has also been shown that the superposition of the rhombic icosahedron along its 5–fold axis suggests the thick and thin rhombs of the P3 tiling. It follows that a rotation of the rhombic icosahedron (and therefore a different projection plane through the 5D hypercube) would give a different set of atomic windows with which to project through. Here, a geometric argument will be made that demonstrates such a rotation produces a 3–fold aperiodic tiling.

Figure 6.6 shows a rhombic icosahedron which has been rotated to demonstrate its 3–fold axis. A set of planes which would act as atomic windows are also shown adjacent. These are shown below, and are a set of triangles, and trapezoids which are reminiscent of the tiles created in the previous section. A projection of the edges of the rhombic

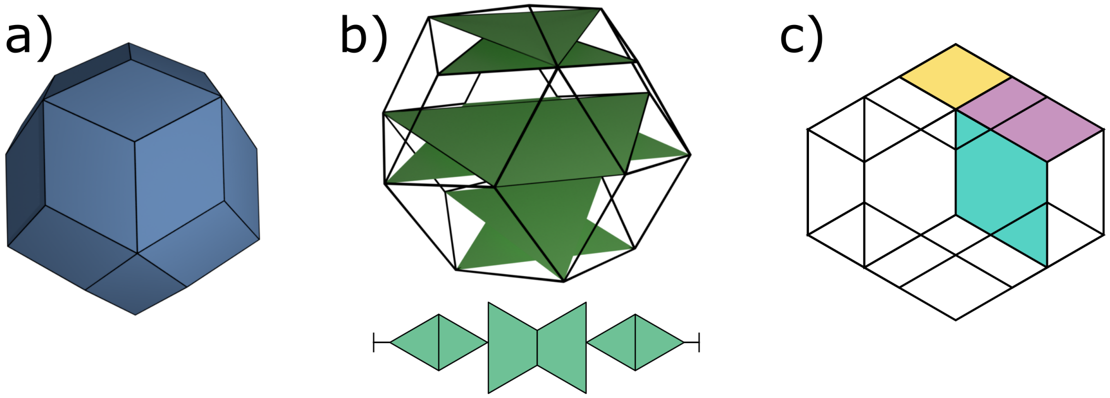

Figure 6.6: **Rhombic icosahedron and 3–fold projection windows: (a)** The rhombic icosahedron tilted to show its 3–fold axis vertical to the page. **(b)** The planes of the rhombic icosahedron which would act as the acceptance windows of projection. **(c)** Superposition of the edges of the rhombic icosahedron. Three constituent tiles are highlighted: large rhomb (blue), small rhomb (yellow), and skewed rhomb (pink)

icosahedron along its 3–fold orientation is also shown, which produces a set of rhombs. These are coloured yellow (small rhomb), pink (skewed rhomb), and blue (large rhomb). Using these tiles as a precursor, Figure 6.7 shows a section of a 3–fold aperiodic tiling. Underneath are a set of vertex configurations. Two of these configurations (far left and far right) could produce a periodic set if only these vertices were considered. Therefore, it is likely that refinement is needed by giving the larger rhombs unique colours, or by stating that these vertex types are not allowed to exist 'consecutively'. Like the tri–grid tiling, the deflations of each of the constituent tiles are non–discrete, and are not shown here. An auto–correlation function of the vertices of the tiling is shown in the top–right of Figure 6.7. As expected, τ–scaled high intensity spots are found.

Much like the relationship between the P1 and P3 Penrose tilings shown in Figure 6.1, there is a relationship between the tri–grid and rhombus tiling. Figure 6.8 shows a section of the tri–grid tiling overlaid with the edges of the rhombus tiling, white. There is a 60° rotation difference between the two. It can be seen that there is a relationship between each of the tiles. For example, and highlighted adjacent, are three large rhombs, and two skewed rhomb tiles with different tri–grid tiling constituents. Each of the large rhomb tiles have been coloured differently (blue, green, red) to show that their tri–grid constituents are unique, and likewise for the two skewed rhombs. These relationships could be the key

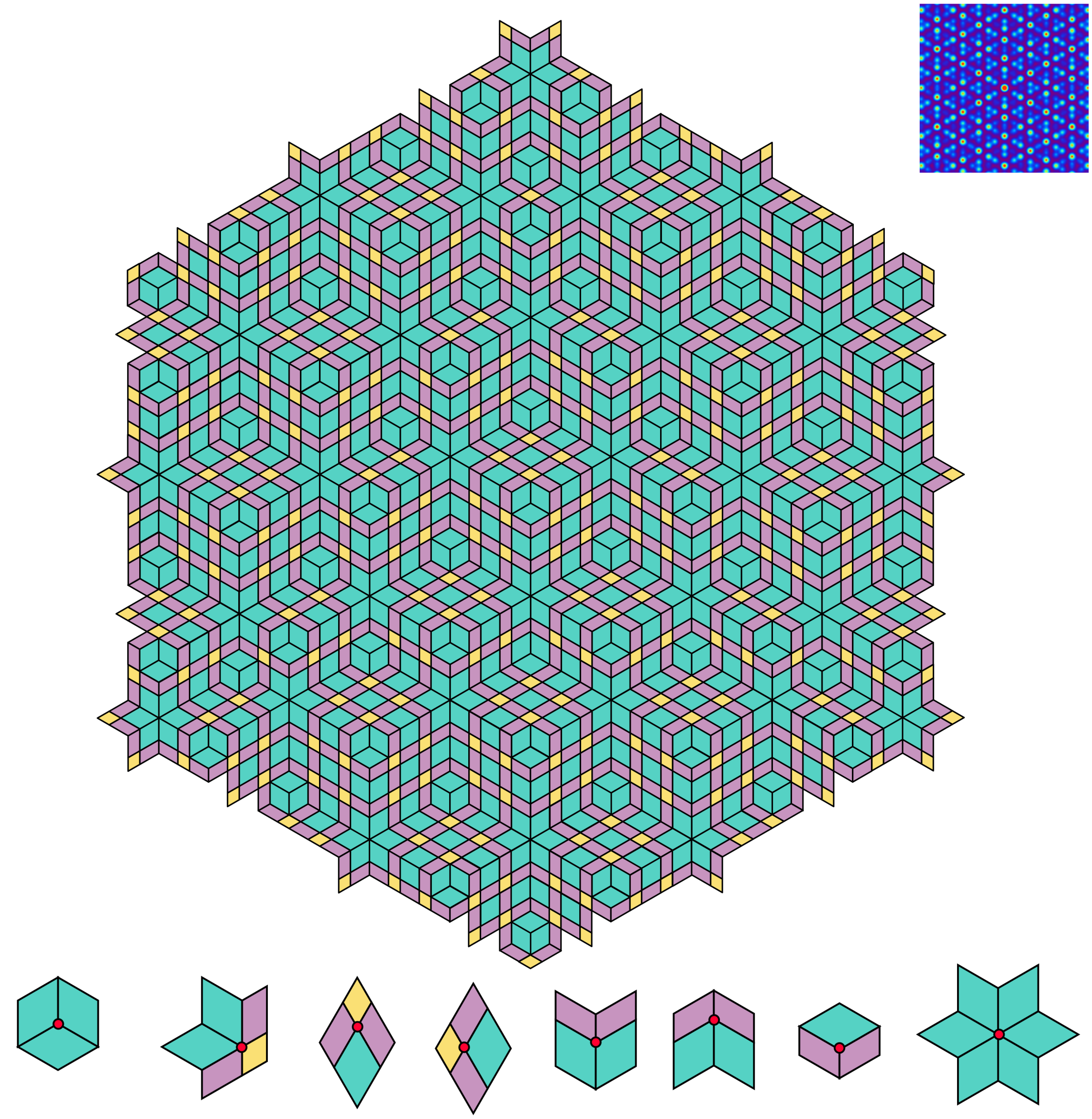

Figure 6.7: **Rhombus tiling:** Using the three tiles created in Figure 6.7(c), a tiling can be grown with vertex enforcement rules (shown below). The tiling is aperiodic, has long-range order, and is 3–fold symmetric.

to understanding or deriving discrete deflation rules (i.e. unique colours). Again however, this could lead to an unwieldy amount of tiles.

It can be said that these tilings are mutually locally derivable [151], where each is obtainable from the other. For example, the rhomb and diamond tiling can be obtained by removing extraneous edges, and vice versa. This relationship serves to prove that not only can the tri–grid be constructed through a consequence of higher–dimensional projection, but also that the deflation rules for both tilings appear to be related.

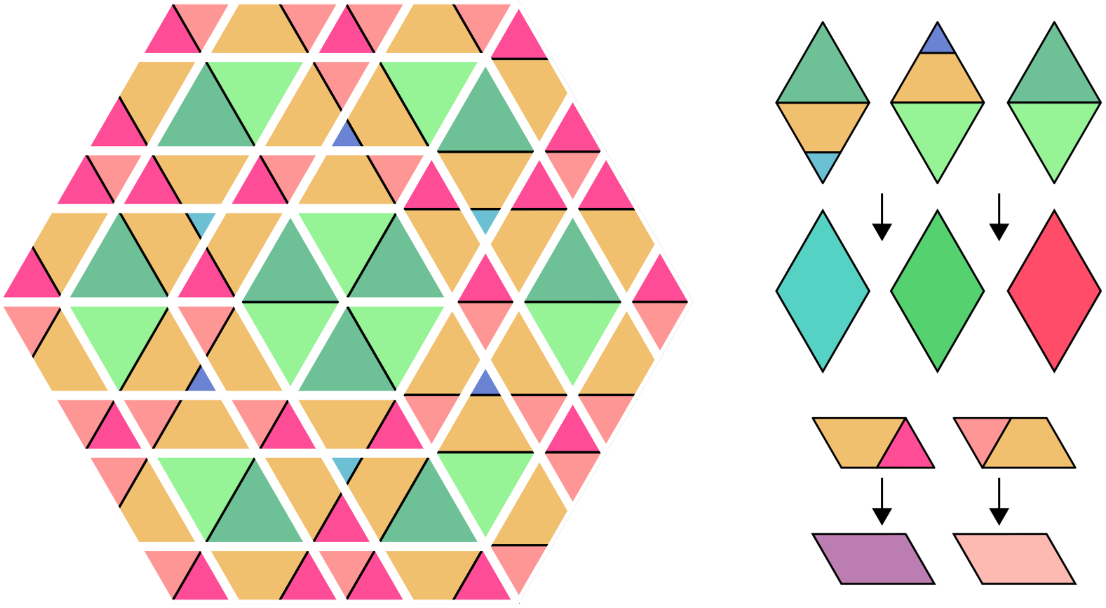

Figure 6.8: **Tri–grid and rhombus tiling relationship:** The rhombus tiling is overlaid in white over the tri–grid. The right–hand side shows relationships between each of the tiles.

6.4 Summary

Examples of two new 3–fold aperiodic tilings have been given using geometric arguments. First, a version was created using a superposition of three Fibonacci sequence sets, placed at 120° relative to each other. This can produce a number of discrete tilings dependent on the relative position of each grid. An example tiling was shown with vertex matching rules and rough deflation examples. Then, using an approximate analogue of the 5D hyperspace projection method, a rhombus and diamond tiling was presented. Again, its aperiodicity and 3–fold symmetry was shown, with vertex configurations given. Its relationship to the tri–grid was highlighted, with suggestions that the lack of discrete deflation rules is in–built into the system.

A rigorous formalism of these tilings is limited by a lack of strict mathematical language. Hopefully in the future, they each can be defined by a method which does not depend simply on aesthetic geometry. The experimental application of the rhomb tiling will be shown in Chapter 7.

Chapter 7

3–fold *i*–Ag–In–Yb: clean surface and Pb adsorption

In this chapter, new STM data from the clean surface of the 3–fold *i*–Ag–In–Yb orientation is re–interpreted with respect to the 3–fold tiling introduced in Chapter 6. It is shown that both cluster centres and general features observed at the surface can be linked by the rhombus tiling. Pb deposition on the surface is then discussed, with adsorption sites explained by planes of the Cd–Yb model. This behaviour is similar to Pb on 5–fold *i*–Ag–In–Yb, as discussed in Chapter 3. However, a difference in density along the 3–fold axis produces a quasi–island Pb film, characterized by sparsely distributed Pb nano–structures.

7.1 Introduction

Unlike the 5–fold *i*–Ag–In–Yb surface, there are only a few studies of the 3–fold termination, with one paper describing its atomic structure, and the other looking at the reactivity of all the high symmetry surfaces of the *i*–Ag–In–Yb system [122, 154, 155].

LEED patterns from the 3–fold *i*–Ag–In–Yb surface show a discrete 3–fold symmetric diffraction pattern, with τ–scaled spots [154]. Similar to the 5–fold surface, the atomic structure of the 3–fold termination can be described by bulk planes of atoms which intersect cluster centres. The observed step–height distribution correlates with the distribution of cluster centre planes in the Cd–Yb model. Step heights of $S = 0.12$ nm, $L = 0.43$ nm were observed, with a frequency of 15% and 85% respectively. Note that this distribution does not create a Fibonacci sequence, unlike the Al–based QCs [155]. As previously mentioned

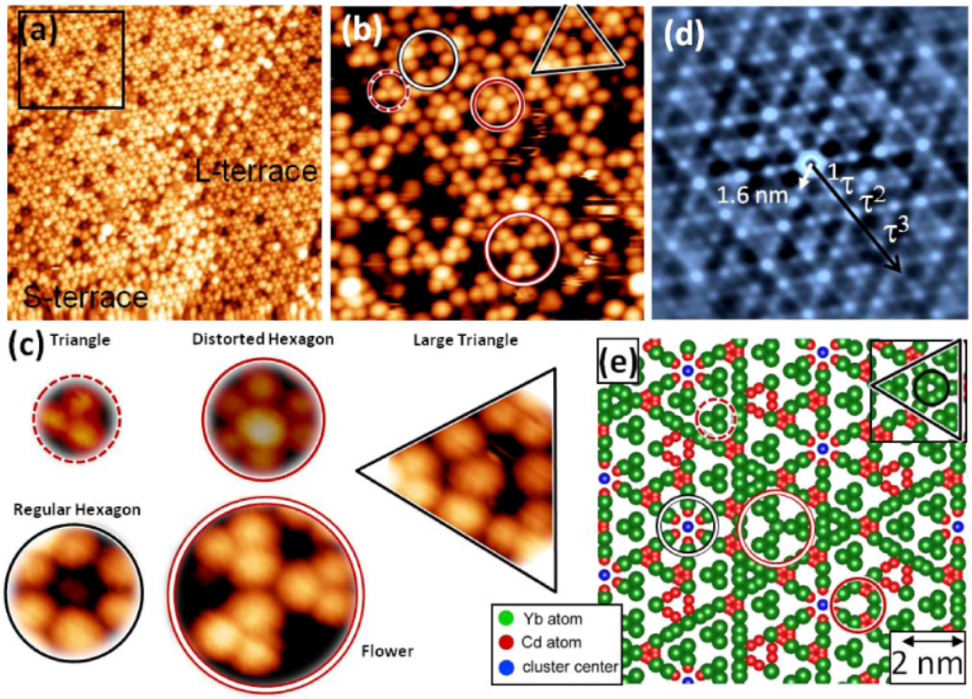

Figure 7.1: **3–fold i–Ag–In–Yb surface:** **(a)** Large scale STM image of an S and L terrace from the 3–fold i–Ag–In–Yb surface. **(b)** Enlarged view of the section highlighted in **(a)**. Several motifs from this image are shown and labelled in **(c)**. **(c)** Triangle, distorted hexagon, large triangle, regular hexagon, and flower motifs highlighted in **(b)**. **(d)** Autocorrelation function of an area of **(a)**. τ–scaled spots are marked. **(e)** Model plane of the surface. Motifs from **(c)** are marked. Reproduced from [154].

in Chapter 2 however, groups of these steps are predicted to form Fibonacci sequences. These planes are dense in In/Yb atoms, and it has been suggested that a high density of In/Yb atoms is required across all surface orientations to reduce surface free energy [156]. Motifs observed by STM were therefore compared to motifs in the cluster centre planes, as shown in Figure 7.1. Here, a series of triangles, hexagons, and 'distorted' hexagons were correlated with Yb arrangements in the cluster centre planes. Ag/In positions were not resolved, unlike with the bias dependent 5–fold termination [66]. However, a certain amount of bias dependency was observed at the 3–fold surface, with Yb atomic resolution only achieved with positive bias.

The stability of each terrace (S or L) was linked to the density of Yb atoms. Fragments of S terraces were routinely observed on top of L terraces, thought to be due to evaporation of S terrace atoms. Here, S terraces contain more ‘glue’ Yb atoms but less cluster Yb atoms. Glue atoms refer to atoms which are not part of the Cd–Yb cluster, but act as joining units between adjacent clusters [6]. However, the overall density of Yb atoms was considered equal between each type of plane. It was concluded that the relatively higher density of glue Yb atoms reduced the stability of the S terraces [154].

Vacancy creation is observed across both types of terraces, and is linked to the relatively homogeneous separation of planes along the 3–fold orientation. Both the 5–fold and 2–fold directions display step–bunching, where closely separated groups of planes form steps, which are then separated by large distances. Along the 3–fold direction however, the relative proximity of neighbouring planes suggests that atoms can ‘jump’ from plane to plane; the implication being that atoms can readily desorb from the surface plane [154]. These vacancies and the generally rough surface that results may provide selective adsorption sites. However, there have been no adsorption studies on the 3–fold orientation – unlike the metallic and molecular growth reported on the 5–fold termination [67, 110, 116, 157].

In this chapter, the 3–fold i–Ag–In–Yb surface will be revisited with respect to the rhombus tiling defined in Chapter 6. Cluster centres and Yb motifs can be linked by the vertices of the constituent rhombus tiles. From here, Pb adsorption will be discussed. Pb has been dosed in order to compare with the multi–layer film on the 5–fold surface, previously discussed in 3. Due to the difference in atomic density along the 3–fold orientation, the Pb grows in a different scheme compared to the 5–fold surface, with quasi–island growth leading to quasicrystalline, 3D nanostructures. The planar and cluster Cd–Yb model first introduced in sections 2.5.2 and 3.2.3 will be referred to often, with a brief summary of the model given at the start of the Pb results section.

7.2 Experimental Details

The surface perpendicular to the 3–fold orientation of an i–Ag–In–Yb quasicrystal was polished with diamond paste of successively finer grade (6–0.25 μm) before washing in methanol. Upon insertion into a UHV chamber, the surface was further prepared by cycles of sputter–annealing. Ar^+ was used to sputter the surface for 30 minutes, with an average drain current recorded at 6.8 μA. The sample was then annealed to 700 K, with each anneal lasting 2 hours. Surface cleanliness was monitored by STM.

For the Pb experiments, Pb was dosed from a crucible, contained within a Focus EFM 3 evaporator. The flux of the evaporated Pb beam was monitored and kept at a constant rate of $\sim 5 \times 10^{11}$ atoms $\text{cm}^{-2}\text{s}^{-1}$.

7.3 Results

7.3.1 Clean surface tiling analysis

As the clean surface of the 3–fold *i*–Ag–In–Yb has been atomically resolved and, in a previous study, compared to planes of the Cd–Yb model, this section will simply show how the 3–fold rhombus tiling defined in Chapter 6 can be used practically, to link, for example, cluster centres at the surface termination. As the tiling was first introduced in this work, such a comparison has not been made previously.

Along the 5–fold and 3–fold orientation, individual, equatorially truncated clusters do not donate their Yb atoms to the surface plane. Rather, Yb positions can be explained by clusters which are centred either above or below the cluster centre plane before truncation. Figure 7.2(a) shows an example. Here, three Cd–Yb clusters are shown, with only their 3rd (Yb, green) and 4th (Cd or Ag/In, blue) shells shown. The middle cluster is centred at a surface truncation plane. The left and right clusters are centred below and above this truncation respectively. Cluster centres are coloured to correspond with their position (red is below, gold is surface, and purple is above). It can be seen that the surface–centred

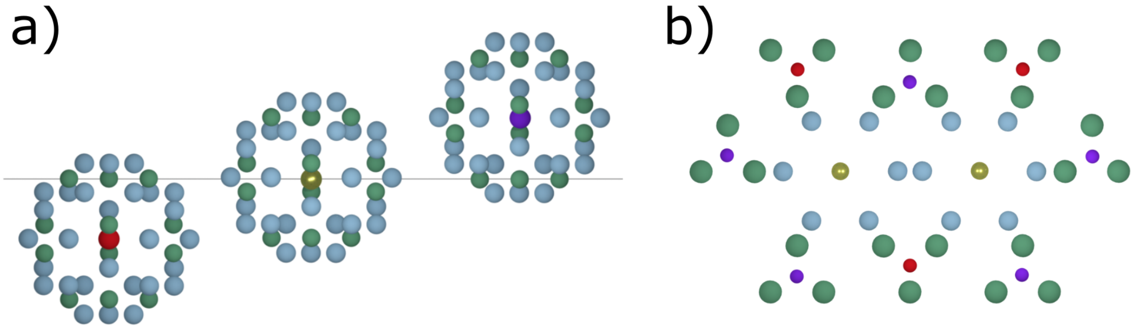

Figure 7.2: **3–fold Cd–Yb cluster surface truncation:** **(a)** Three Cd–Yb clusters are shown with only their 3rd (Yb, green) and 4th (Cd or Ag/In, blue) shells shown. Cluster centres are coloured with respect to a surface truncation: red is below, gold is surface–centred, whilst purple is above the surface. **(b)** A top–down view of a surface arrangement. Cluster centres are shown, highlighting the contribution of each cluster to the surface plane.

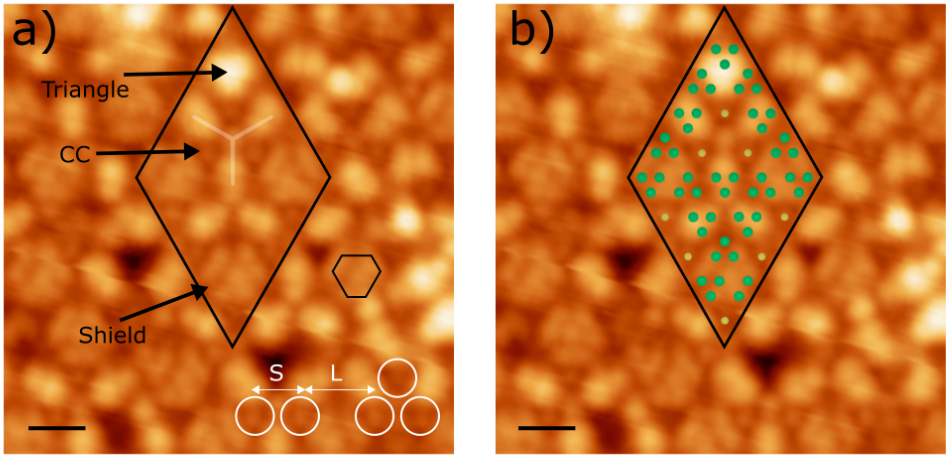

Figure 7.3: **3–fold surface model:** **(a)** STM image (V_b = 3079 mV, I_t = 0.119 nA) of the clean 3–fold *i*–Ag–In–Yb surface. Marked are motifs previously observed in [154]. Surface cluster centres are also marked, either by an arrow (CC), or by white circles. **(b)** Same image as **(a)**, with the Cd–Yb model overlaid. Yb atoms are green, cluster centres are gold. Scale bars both represent 2 nm.

cluster donates Cd atoms only to the substrate. Similarly, both the above and below surface clusters donate Yb atoms only. Figure 7.2(b) shows a top–down view of an example of such an arrangement. Two Cd hexagons are surrounded by up and down Yb triangles, with their donating cluster centres coloured with respect to the colour scheme in Figure 7.2(a). Here, up triangles are donated by above surface clusters, and vice versa. As only Yb atoms are resolved on the 3–fold surface by STM, we are therefore observing atoms which are not donated by surface–centred clusters [154]. However, common Yb motifs which are created by the interaction of below and above surface clusters can be linked to the Cd–Yb model, as discussed above.

Figure 7.3(a) shows an STM image obtained from the 3–fold surface with near atomic resolution. Highlighted by a diamond is a section of the surface containing motifs from Figure 7.1. Labelled is a distorted hexagon, reminiscent of the shield tile from the tri–grid in chapter 6. The shield tile is shown adjacent in black. Also marked by three translucent lines is a ‘flower’ which is resolved as three protrusions. A single triangle is also marked. In between these motifs are small protrusions, with one marked by an arrow. Others are highlighted below by white circles. The separation of these protrusions along the high symmetry axes are $S = 1.57 \pm 0.07$ nm, and $L = 2.43 \pm 0.07$ nm. These lengths, along with the Yb motifs, can be used to match the protrusions to surface truncated cluster centres. Figure 7.3(b) shows an overlay of the Cd–Yb model on top of (a). Green circles are Yb atoms, golden circles are the cluster centres. Here each Yb motif is replicated with respect to Figure 7.1 and the previous report on the surface [154]. Likewise, the protrusions from Figure 7.3(a) match the model cluster centres. The model cluster centre separations are given with a percentage difference to the experimentally measured values: S = 1.57 nm (±1%), and L = 2.53 nm (±4%). As these protrusions do not match any Yb sites, and fit with the model surface cluster centres, it is proposed that, despite the cluster centre containing no atoms, in some form, each protrusion is indicative of a surface–truncated cluster centre.

These protrusions could belong to atoms from the 1^{st} shell, which lie 0.091 nm below the surface plane in the Cd–Yb model. The protrusions observed lie, on average, 0.10 ± 0.03 nm below the Yb atoms. The 1^{st} shell atoms are typically not considered in terms of surface structure or as part of an adsorption scheme, as this shell reorients itself within the Cd–Yb bulk cluster dynamically – essentially ‘spinning’, with only a time–averaged position considered [158–160]. The dynamic timescale of the tetrahedron is on the order of a few picoseconds. It is possible to consider, then, that a time–averaged position is observed by STM if the partial density of states of the shell is considered constant over the timescale of the raster of the STM scan (on the order of seconds).

Before the experimental cluster centres can be linked by the 3–fold rhombus tiling, it is important to note the degree to which a tiling can link together Cd–Yb cluster centres in the model. Figures 7.4(a, b) show the cluster centres of 5–fold and 3–fold Cd–Yb surface planes, respectively. Linking the centres together in (a) is a Penrose P1 tiling in black (edge length 2.54 nm), and also in purple (edge length 1.57 nm). Circled in black are ‘extraneous’ cluster centres which are ‘missed’ by the tiling, whilst purple circles indicate non–existent cluster centres at the vertices of the τ–deflated tiling. A similar scheme for the 3–fold distribution is labelled in Figure 7.4(b), with the same edge lengths. The match between the cluster centres and the rhombus tiling vertices is excellent, as expected from the link to the 3D Penrose tiling structure [6].

This simple example illustrates the concept that the cluster centre distribution on either surface is not bound by a single discrete 2D tiling of a particular length scale. Rather, when matching cluster centres to a tiling, a choice must be made to either ‘miss’ cluster centres (black), or to create a tiling in which not every vertex intersects with physical cluster centres (purple). For the experimental comparison, an edge length of 2.54 nm is

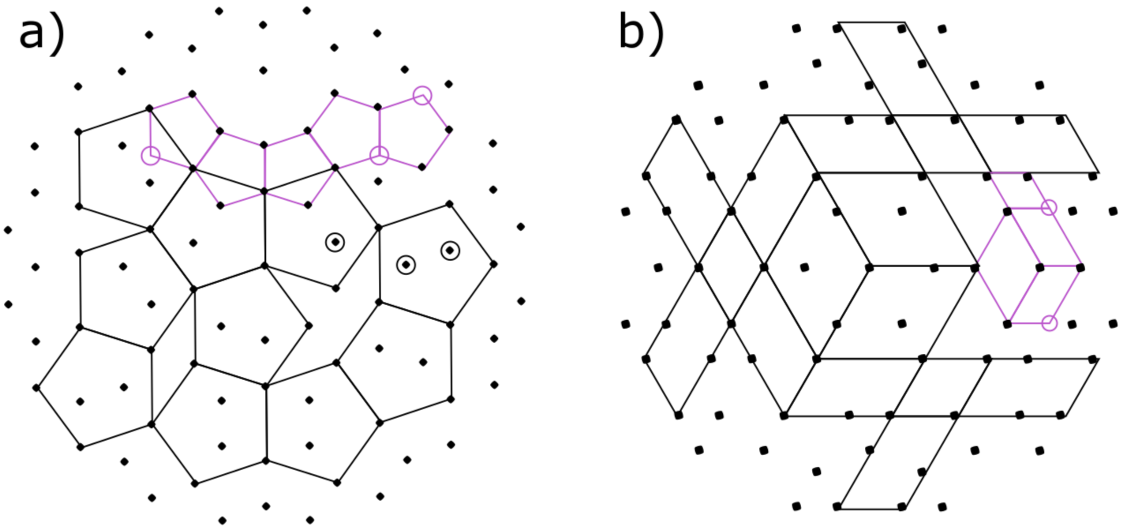

Figure 7.4: **Penrose and 3–fold rhombus tiling comparison:** **(a)** The distribution of cluster centres at a surface plane of the 5–fold *i*–Ag–In–Yb QC. Cluster centres are linked by a Penrose P1 tiling with two edge lengths: black = 2.54 nm, purple = 1.57 nm. **(b)** Same as **(a)**, along the 3–fold orientation. A rhombus tiling is overlaid, with edge lengths: black = 2.54 nm, purple = 1.57 nm.

chosen for the rhombus tiling – whereby cluster centres are sometimes 'missed'. This length refers to the large rhombus tile edge length.

Figure 7.5(a) shows a high contrast, larger scale STM image from Figure 7.3. Here, the protrusions are more visible than in Figure 7.3, at the expense of some resolution of Yb features. Using this image, a collection of surface cluster centre protrusions can be marked by blue circles, and linked by the the rhombus tiling. Figure 7.5(b) shows (a) with cluster centres and 3–fold rhombus tiles overlaid. The vertices of each tile is matched to a surface cluster centre. The good fit between the experimental cluster centres and tiling vertices indicates the rhombus tiling is a good match to the data. Likewise, the mutually locally derivable nature of the rhombus and tri–grid tiling infer that the tri–grid could also link the cluster centres highlighted.

Additionally, Figure 7.5(c) shows the rhombus tiling linking individual shield motifs and bright protrusions. The shield structures are explained by clusters both above and below the surface truncation plane 'donating' Yb triangles. Therefore, it is more accurate to say that the vertices intersect with either an up or down Yb triangle donated from

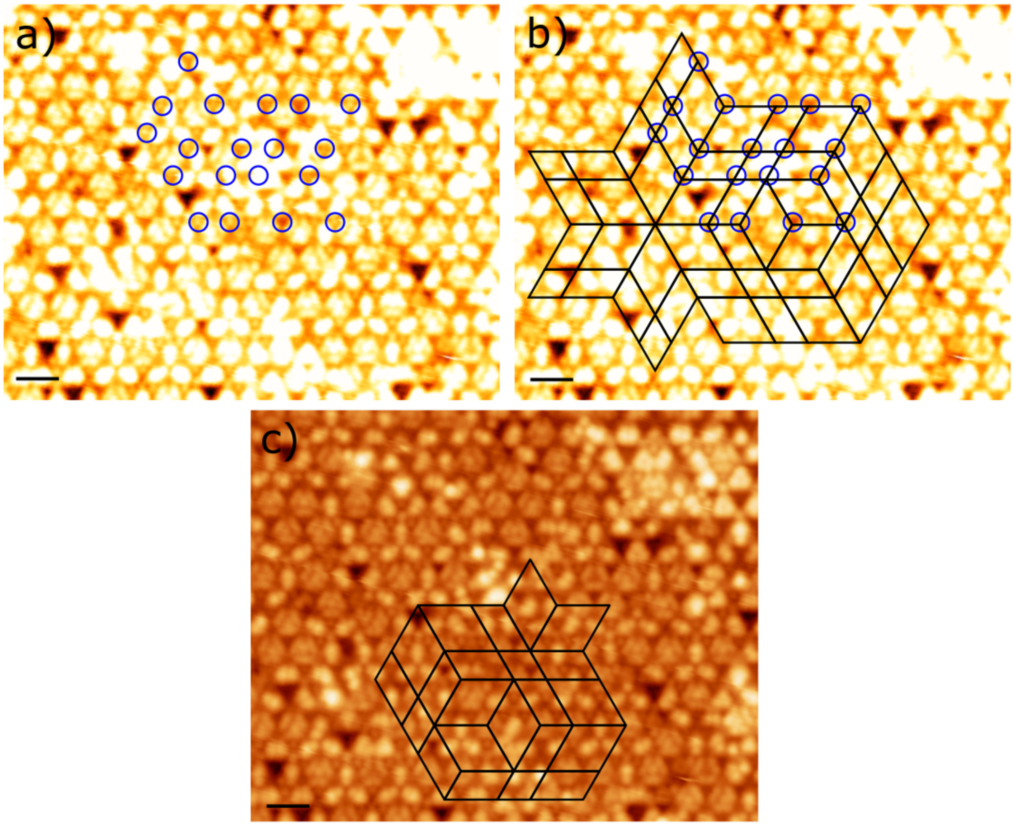

Figure 7.5: **The rhombus tiling on the 3–fold *i*–Ag–In–Yb surface: (a)** High contrast STM image of the 3–fold *i*–Ag–In–Yb surface. Surface cluster centres are highlighted in blue. **(b)** Same as **(a)**, with tiles from the 3–fold rhombus tiling overlaid. **(c)** STM image with rhombus tiles linking shield Yb motifs. A white circle indicates an 'up' triangle from Figure 7.1. All scale bars are 3 nm.

a cluster either above or below the surface. This tiling therefore maps below or above surface–centred clusters.

7.3.2 Pb dosed 3–fold surface

Dosing Pb on the 3–fold *i*–Ag–In–Yb surface produces a quasicrystalline arrangement of 3–dimensional nanostructures. Here, Pb is considered to grow in a 'quasi'–Volmer–Weber type growth mode, where successive Pb layers begin growing before the previous layer reaches full ML coverage. Pb atoms adsorb at specific heights above the substrate. Their

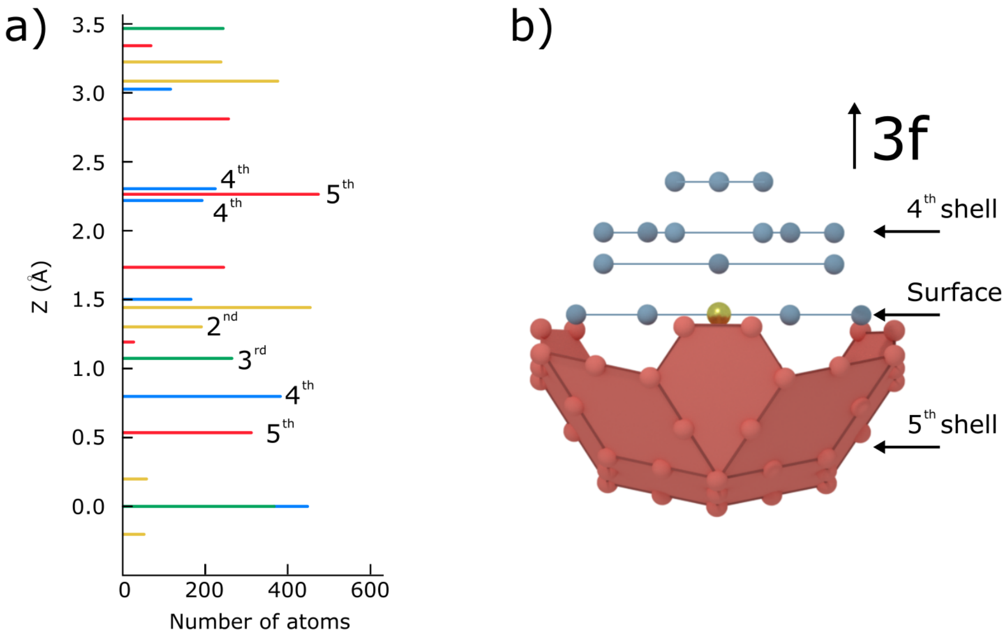

Figure 7.6: Planar Cd–Yb model: (a) Planes of either Cd or Yb atoms can be stacked in z, corresponding to their heights in individual Cd–Yb clusters. The chart shows the density of planes of atoms from each shell, where the 2nd is yellow, 3rd is green, 4th blue, and 5th red. A few planes are marked as so. A close collection of planes are labelled for later discussion. **(b)** A truncated cluster shows how to consider the planes, where the atoms shown above the surface plane are from the 4th. The surface plane is labelled. The cluster centre is shown as gold.

in–plane adsorption positions can be explained by planes of the Cd–Yb model, as with the 5–fold system.

Here, the structure of each layer will be discussed. To determine which plane can describe adsorption sites, a 'height–motif' technique is used: the height of each layer is measured above either the substrate or above previous layers. This height is compared to a planar model of the 3–fold orientation. Shells from the Cd–Yb cluster model contribute layers of planes at specific heights in z, Figure 7.6. Matching heights therefore suggest planes which can describe in–plane adsorption positions. Motifs in the planes can then be compared to motifs observed in each layer. Subsequently, the relative (and often unique) geometries between each layer can be compared between model and experimental observation. Figure 7.6, which details the planar model, will therefore be referred to with respect to the heights of planes above the substrate. The 1$^{\text{st}}$ shell is omitted from this figure, as it is not relevant for explaining adsorption sites. A table of heights is also included at the end of this section.

The contrasting growth method to the multi–layer film system on the 5–fold surface will be discussed, along with its implications for the 3–fold system.

First layer

At low Pb coverage, it is difficult to distinguish Pb atoms and the substrate due to the roughness of the clean surface (RMS roughness $= 0.05 \pm 0.01$ nm). At higher coverages however, Pb grows with a structure which is distinctive from the substrate. Figure 7.7(a) shows an STM image after dosing Pb for 10 minutes, with a coverage of approximately 0.6 ML. The image has been filtered so that the substrate is barely visible, and the bright protrusions are Pb atoms. The coverage was therefore estimated by subtracting the area representing the substrate from the image. Contained within three white triangles, labelled as 1–3, are motifs which appear throughout the film. Here, each motif will be referred as motif $1 = \mathrm{M}_1$, etc. Their edge lengths are measured as $\mathrm{M}_1 = 1.11 \pm 0.08$ nm, $\mathrm{M}_2 = 1.5 \pm 0.1$ nm, and $\mathrm{M}_3 = 2.6 \pm 0.1$ nm. The three motifs are related to each other by: $\mathrm{M}_3 = \tau \mathrm{M}_2$, and $\mathrm{M}_2/M_1 = 2/\tau$. Each labelled motif are oriented 'upwards', although downwards orientations of each are also found. Marked by a dashed triangle is a bright protrusion sitting at the centre of a downwards facing M_2 triangle. This is the start of the second layer of Pb.

Figure 7.7(b) is an FFT of Figure 7.7(a), which shows τ–scaled spots along a set of 6–fold rotational axes, a consequence of the inversion symmetry of the motifs (up and down orientations). Likewise, Figure 7.7(c) shows an autocorrelation function from Figure 7.7(a) with the same τ–scaled behaviour and 6–fold symmetry. Thus, the film is quasiperiodic considering the definition outlined in Chapter 4.

The height of the film above the substrate is measured using the histogram in Figure 7.7(e). Marked are the heights of the substrate and the film, with the difference also shown, 0.058 ± 0.003 nm. The planar model of the 3–fold orientation (Figure (7.6)) shows a plane 0.054 nm above the surface termination, which is attributed to the 5th shell of the Cd–Yb cluster. The plane is shown in Figure 7.7(d). It contains dense triangles, hexagons, and, predominantly, dimers oriented along the principal 3–fold axes. These closely separated features (nearest neighbour ~ 0.3nm) are not resolved: the average diameter of individual

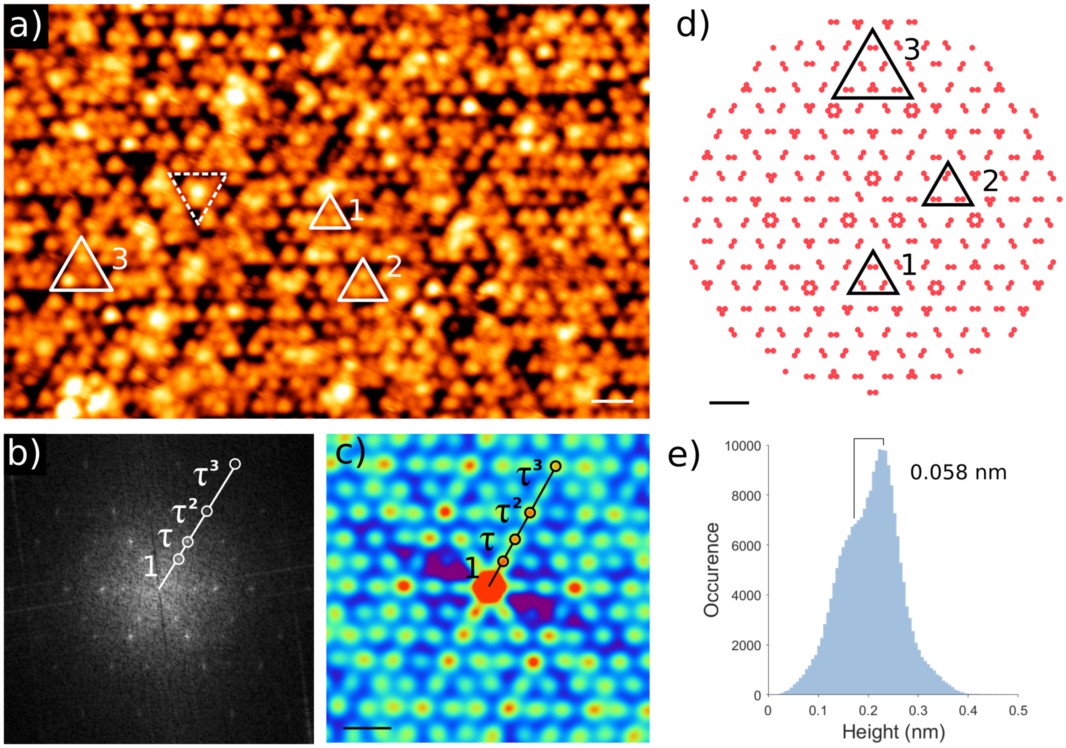

Figure 7.7: **First Pb layer on the 3–fold *i*–Ag–In–Yb surface:** **(a)** STM image (V_b = −1969 mV, I_t = 0.243 nA) of the first Pb layer. Highlighted in white are three motifs for comparison with the model structure. Marked in a dashed triangle is the start of the second layer. Scale bar is 4 nm. **(b)** An FFT of (a). Marked are τ–scaled spots, indicating quasiperiodicity. **(c)** Autocorrelation function of (a), also showing τ–scaled spots of high intensity. Scale bar is 2 nm. **(d)** Model plane from the 5th Cd–Yb shell which can explain adsorption positions of Pb atoms. Marked are the same motifs as in (a). Scale bar is 2 nm. **(e)** A histogram used to calculate the height of the Pb atoms above the substrate.

protrusions has been measured along the three high symmetry directions as: 0.8 ± 0.1 nm. This measurement is consistent with two Pb atoms with a Van der Waals radius of 0.2 nm [161] separated by 0.3 nm, as predicted by the model plane. Given the lack of resolution achieved by STM however, it may be more accurate to describe this layer as groups (dimers/trimers) of Pb atoms which lie at the average positions of the dense features in Figure 7.7(d).

Figure 7.7(d) shows the highlighted motifs, 1–3, from Figure 7.7(a). The model edge

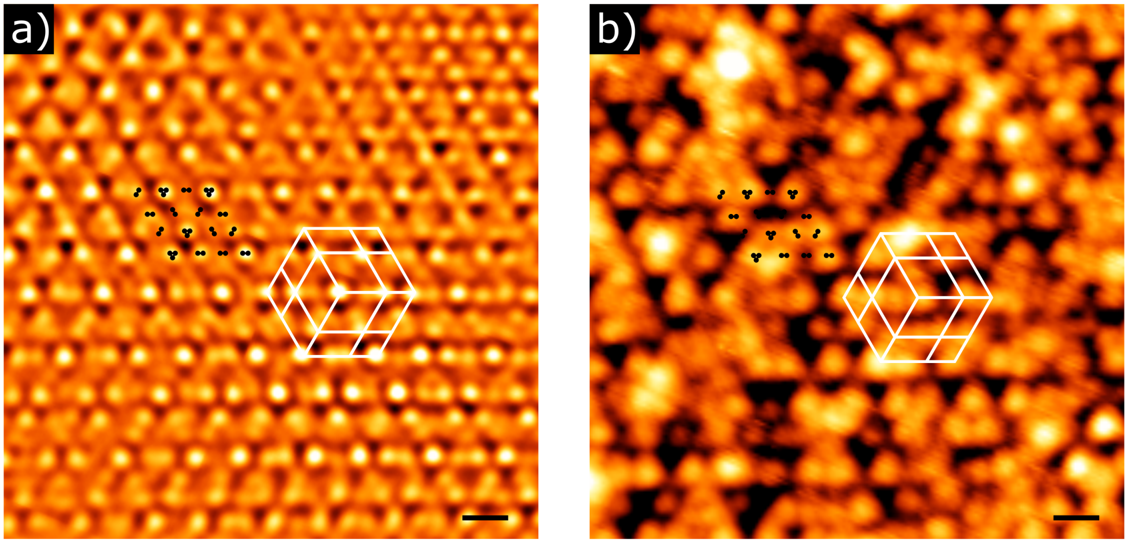

Figure 7.8: **1st Pb layer comparison:** **(a)** Inverse FFT calculated using Figure 7.7(b). Overlaid in black is a section of the plane used to model the first Pb layer. Also shown is a section of the rhombus tiling. Scale bar is 2nm. **(b)** Same as (a), using the raw STM image from Figure 7.7 (a).

lengths of the motifs are calculated by considering, as a single point, the average position of the dimers at each vertex, to compensate for the lack of resolution achieved. They are given, along with their percentage match with the experimental value, as $M_{M1} = 1.17$nm (±5%), $M_{M2} = 1.42$ nm (±6%), and $M_{M3} = 2.68$ nm (±3%), where subscript M refers to the model. The ratio of $M_{M3}/M_{M2} = \tau$, and $M_{M2}/M_{M1} = 2/\tau$, again in agreement with the experimental ratios. The match between the model plane and STM is illustrated by an inverse FFT calculated from Figure 7.7(b). Figure 7.8(a) shows the inverse FFT, with a section of the model plane overlaid. Also shown are protrusions joined by a patch of 3–fold rhombus tiles of edge length 2.53 nm. Figure 7.8(b) shows the original STM image, with the same illustrations overlaid. There is a good fit between the film and model plane.

Second layer

Figure 7.9(a) shows an STM image taken after dosing the clean surface with Pb for 15 minutes. Here, the substrate has been filtered out, so that three Pb layers are visible – the third layer has been marked with a black ring. Two second layer motifs are highlighted and numbered as 4 and 5. M_4 and M_5 have similar edge lengths, $M_4 = 1.1 \pm 0.1$ nm and

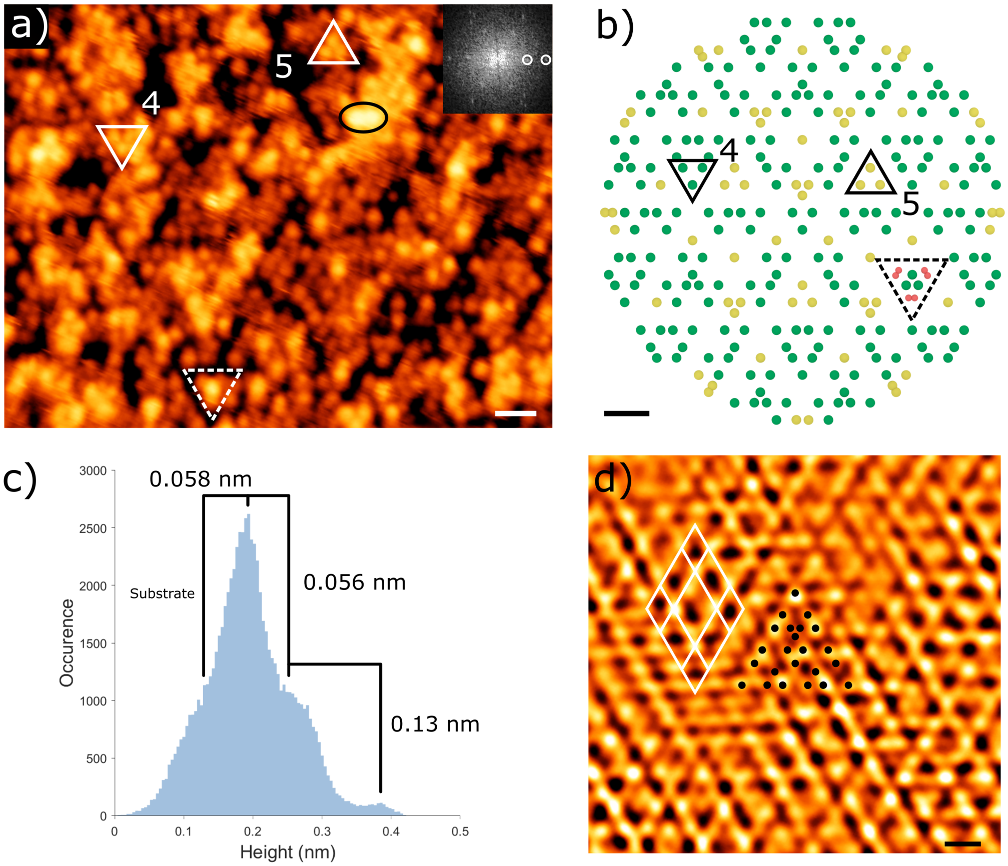

Figure 7.9: **Second Pb layer on the 3–fold i–Ag–In–Yb surface:** **(a)** STM image (V_b =-1543 mV, I_t = 0.101 nA) of the second Pb layer. Highlighted and numbered are two similar motifs in up and down orientations. The dashed triangle is the same motif from Figure 7.7(a). Circled in black is the start of the third layer. Scale bar is 3nm. **(b)** Model plane of the second Pb layer. Green atoms are Yb sites predicted by the Cd–Yb clusters, yellow are Yb glue atoms. Highlighted are the same motifs from **(a)**. The first Pb layer is superimposed on the dashed triangle. Scale bar is 2nm. **(c)** Histogram of **(c)** with relative heights of each layer labelled. **(d)** Inverse FFT of **(a)**. A portion of **(b)** is overlaid, along with a section of the rhombus tiling. Scale bar is 2nm.

M_5 = 1.0 ± 0.1 nm. They are rotated by 60° with respect to each other (down and up orientations respectively). The bright protrusion inside an M_2 triangle from Figure 7.7(a) is marked with a dashed triangle. Inset is an FFT taken from the second layer Pb atoms only, with two sets of τ–scaled spots indicated. Therefore, the second Pb layer is also considered quasiperiodic.

Figure 7.9(c) is a histogram taken from Figure 7.9(a), which shows three distinct peaks above the substrate, which is labelled. The height difference between each peak is marked. The second layer therefore lies 0.056 ± 0.004 nm above the first, corresponding to an atomic plane of Yb atoms in the planar Cd–Yb model (Figure 7.6). Figure 7.9(b) shows this plane. Here, green atoms are Yb sites which can be explained by the 3rd shell of the RTH cluster, whereas yellow atoms are glue atoms from the units that join RTH clusters [6]. Motifs 4 and 5 from Figure 7.9(a) are labelled, with their edge lengths agreeing with the experimental values: $\mathrm{M}_{M4} = 0.97$ nm (±4%), $\mathrm{M}_{M5} = 0.97$ nm (±3%). The match between the model structure and STM image is compared in Figure 7.9(d). Here, a section of the model plane is overlaid on an inverse FFT calculated from the inset of Figure 7.9(a), with a good fit observed. Also overlaid is a section of the rhombus tiling.

The selection of this plane to explain the second layer adsorption sites can also be checked against the relative geometries of the first and second layer Pb atoms. Marked in Figure 7.9(b), inside a dashed triangle, is a second layer triangle with an edge length of 0.60 nm. Surrounding the triangle are atoms which are superimposed from the first layer plane. This configuration would therefore produce the bright protrusion inside an M_2 triangle seen in Figures 7.7(a), 7.9(a), where the small 2nd layer Pb triangle is not resolved and appears as a single point.

Motif 5 is only found in the model plane if it contains at least 1 glue atom, suggesting that Pb adsorbs at sites explained by the cluster–joining units. This is counter to the previous findings on the 5–fold surface, where Pb adsorbing at positions predicted by Yb planes ignore the glue atom sites [67]. The potential explanation for this difference will be discussed later on.

Third layer

After dosing Pb for 30 minutes on the clean surface, the third layer observed in Figure 7.9(a) develops triangular features. Figure 7.10(a) shows an STM image where again the substrate has been filtered out. Here, the first layer is approaching 100% coverage, defined here as completely filling the positions of the model plane used to describe the adsorption sites. Highlighted and numbered is a third layer Pb triangle, motif 6, which is largely the only motif observed in the third layer, occurring only in an ‘up’ orientation. Its edge length is $\mathrm{M}_6 = 0.96 \pm 0.03$ nm. Motif 7 shows second layer Pb atoms which form a shield

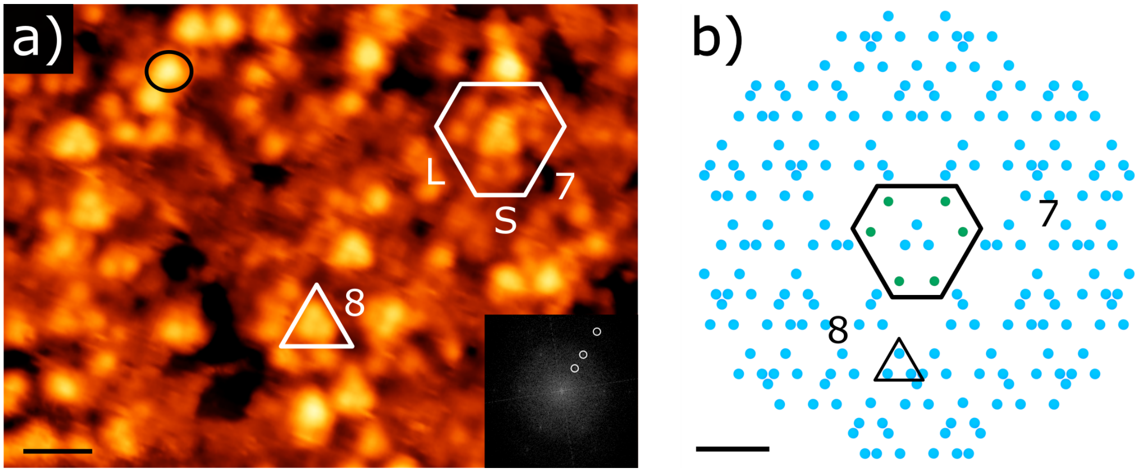

Figure 7.10: **Third Pb layer on the 3–fold *i*–Ag–In–Yb surface:(a)** STM image (V_b =967 mV, I_t = 0.258 nA) of the third Pb layer. Numbered and labelled are two motifs. Motif 7 shows the distinction between the second and third Pb layers. The fourth layer is circled in black. Scale bar is 3 nm. **(b)** Model plane of the third Pb layer. Labelled are the same motifs as in **(a)**. Scale bar is 3 nm.

tile, inside of which sits an M_6 triangle. Its edge lengths are M_{S7} = 1.5 ± 0.1 nm, and M_{L7} = 2.4 ± 0.1 nm, where L/S = 1.6 ± 0.1. Circled in black is the start of the fourth layer.

Using the histogram from Figure 7.9(c), the third layer is 0.130 ± 0.004 nm above the second. Figure 7.6 shows that there are three planes which could explain prospective adsorption sites with this height – one 5th shell plane, and two 4th shell planes, which are marked. The 5th shell plane is discounted as, although it produces triangles of the correct size, they appear in two orientations. The two fourth shell planes both produce triangles of the correct size with a single orientation, yet these planes are rotated by 60° with respect to each other (i.e. one produces 'up' triangles, the other 'down'). Motif 7 can be used to distinguish the correct plane, as its construction is dependant on the superposition and relative orientations of the second and third layers. Figure 7.10(b) shows the plane selected (1.23 nm above the second layer), where the shield feature from the second layer is also included in green. The comparison and match of the second and third model plane geometry is important, as each plane confirms the others' selection: no other combination of second and third layer planes produce the triangle–in–hexagon motif as above. The edge lengths of the model motifs along with their percentage difference are given as: M_{M6} = 1.04

nm (±8%), $M_{MS7} = 1.57$ nm (±5%), and $M_{ML7} = 2.4$ nm (±6%).

STM images filtered to include only the third layer provide a very weak τ–scaled FFT (inset on Figure 7.10(a)). Considering that the Pb positions/motifs match well with a quasiperiodic plane (and the distribution of atoms is qualitatively non–periodic), it is presumed that the low intensity of these spots is indicative of the relatively low coverage of the third layer.

Fourth layer

Figure 7.11(a) shows an STM image after dosing the surface with Pb for 120 minutes. The image has been adjusted to show the third and fourth Pb layers only. Highlighted are three motifs, 8, 9, and 10. A black circle marks the start of further Pb growth, see next subsection for details. Motifs 8 and 9 have similar length scales, and are rotated by 60° with respect to each other (up and down orientations). Their edge lengths are $M_8 = 1.6 \pm 0.1$ nm, and $M_9 = 1.5 \pm 0.1$ nm. Motif 10 consists of three small Pb triangles of edge length 1.0 ± 0.1 nm, constructing a larger triangle with edge length $M_{10} = 2.5 \pm 0.1$ nm. The edge length here is measured from the centre of each triangle at the vertex of the larger triangle structure. A further motif for comparison is highlighted by a dashed triangle. Figure 7.11(c) shows an FFT taken from the fourth Pb layer only. Two sets of 6–fold τ–scaled spots are observed, and are marked. This suggests that the fourth layer is also quasicrystalline.

Figure 7.11(b) shows an enlarged view of the feature contained within the dashed triangle. This configuration can be used to find the height of the fourth layer. Adjacent to the fourth layer structure is a triangular formation which consists of three M_6 triangles from the third layer, which are marked. Highlighted is the direction of a line profile, which is shown below the STM image.

Using the line profile, the relative height difference between the two layers is measured as: 0.11 ± 0.01 nm. The planar Cd–Yb model gives a plane 0.12 nm above the third layer (Figure 7.6), which is constructed of 3rd shell (Yb atoms), and shown in Figure 7.11(d). Glue Yb atoms are not included in this figure, as there is no strong evidence to suggest adsorption at these sites in this layer. Labelled are the motifs observed in Figure 7.11(a), with their edge lengths given with their percentage difference to the experimental values: $M_{M8} = 1.57$ nm (±2%), $M_{M9} = 1.57$ nm (±5%), and $M_{M10} = 2.54$ nm (±2%). The individual triangles which form M_{M10} have a model edge length of 0.97 nm (±3%).

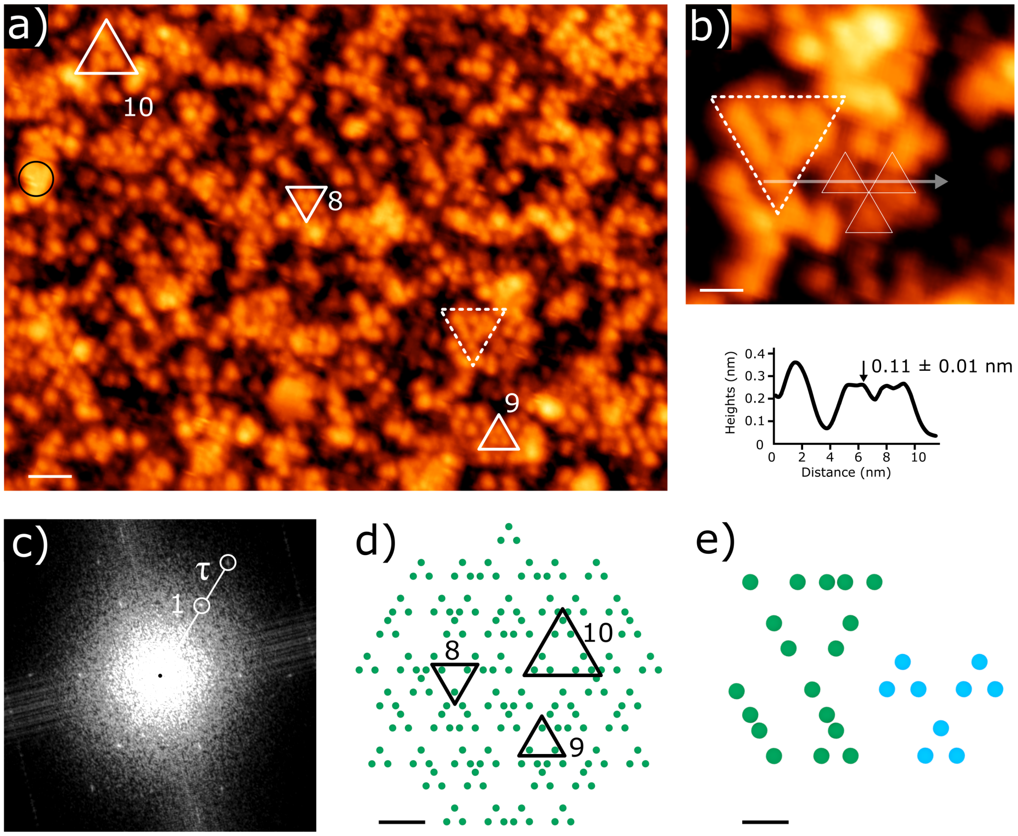

Figure 7.11: **Fourth Pb layer on the 3–fold *i*–Ag–In–Yb surface:** **(a)** STM image (V_b =2725 mV, I_t = 0.168 nA) of the fourth Pb layer. Motifs 8–10 are labelled. A dashed triangle marks **(b)**, which is used to distinguish between the fourth and third layers. A black circle notes the beginning of another Pb layer. Scale bar is 3 nm. **(b)** An enlarged view of the dashed triangle from **(a)**, with a line profile between the fourth and third layer shown. Scale bar is 2 nm. **(c)** An FFT from the fourth Pb layer. τ–scaled spots are shown. **(d)** A model plane of the fourth Pb layer. Highlighted are the same motifs as in **(a)**. Scale bar is 2 nm. **(e)** Enlarged model view of **(b)**, with the third layer superimposed. Scale bar is 1 nm.

As with the triangle–in–shield construction in Figure 7.10(a), a comparison between the fourth and third layer geometries can indicate whether the correct plane has been chosen to explain adsorption sites. Figure 7.11(e) shows an enhanced model view of Figure 7.11(b) and its surrounding atoms in green, alongside three M_6 triangles in blue, whose positions are predicted by the third plane. This arrangement matches very well with the

Layer	Height$_{STM}$ (nm)	Height$_{M}$ (nm)	Motif	Edge$_{STM}$ (nm)	Edge$_{M}$ (nm)
1	0.06 ± 0.01	0.05	1	1.11 ± 0.08	1.17
			2	1.5 ± 0.1	1.42
			3	2.6 ± 0.1	2.68
2	0.11 ± 0.01	0.11	4	1.1 ± 0.1	0.97
			5	1.0 ± 0.1	0.97
3	0.23 ± 0.01	0.23	6	0.96 ± 0.03	1.04
			7(S)	1.5 ± 0.1	1.57
			7(L)	2.4 ± 0.1	2.54
4	0.35 ± 0.02	0.35	8	1.6 ± 0.1	1.57
			9	1.5 ± 0.1	1.57
			10	2.5 ± 0.1	2.54

Table 7.1: **3–fold Pb heights and edge lengths:** The heights of Pb layers and edge lengths of motifs, compared to their model plane counterparts. Subscript STM refers to the experimentally measured heights and edge lengths. Subscript M refers to the Cd–Yb model values. Here, heights are referred to as above the substrate.

experimental observation, and, again, can only occur if these particular planes are selected to explain the adsorption sites. For clarity, the edge lengths of all experimental and model motifs are collected alongside the heights of each plane/layer in Table (7.1).

Islands

Further Pb deposition (> 150 minutes) results in crystalline Pb islands. Figure 7.12 shows a collection of STM images at a range of magnifications, obtained after dosing for 240 minutes. Highlighted in Figure 7.12(a) is an angle, $\alpha = 120 \pm 7°$, between two edges of an island. Likewise marked in Figure 7.12(b) is $\beta = 61 \pm 4°$. These angles are indicative of 3–fold and 6–fold symmetry respectively. Atomic resolution of the islands was not achieved, so their crystalline nature is inferred: considering the co–existence of small islands and quasicrystalline nano–structures in Figure 7.12(c), the islands are identified as growth of the [111] orientation of fcc Pb (60°), which are constricted along a set of 3–fold axes (120°). Such an observation is consistent with crystalline allotropes of Pb observed on the 5–fold i–Ag–In–Yb surface, which show crystalline island edge angles of $n\frac{\pi}{5}$ [162]. The formation of islands before previous layers reach 100% occupancy Figure 7.12(c) indicates that crystalline growth is preferred to filling, say, the third and fourth quasicrystalline Pb layers.

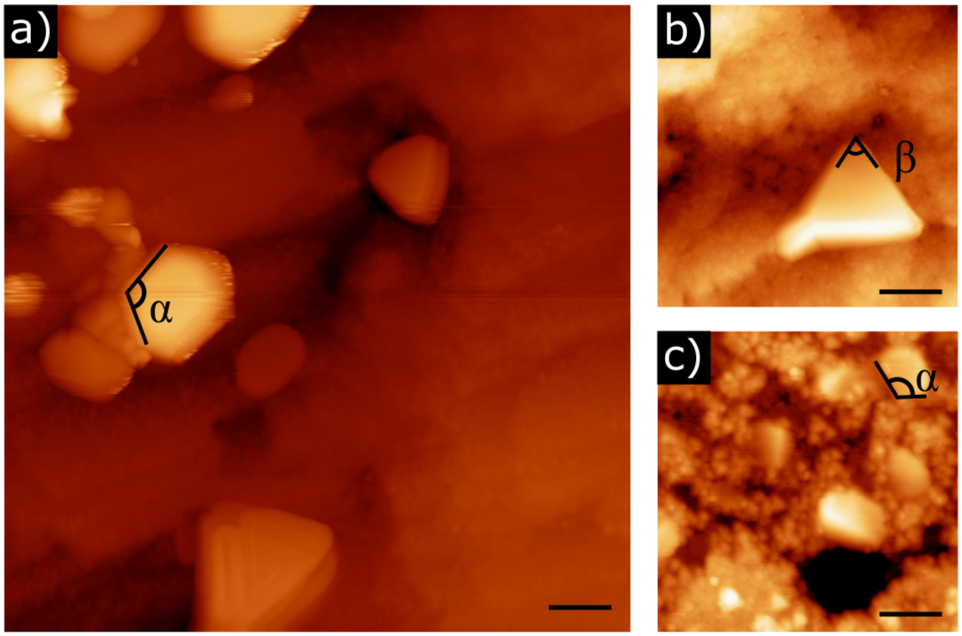

Figure 7.12: **Crystalline Pb islands:** **(a)** High coverage Pb produces crystalline islands. Marked as α is the angle between edges of a Pb island. Scale bar is 40 nm. **(b)** Same as **(a)**, with a different angle, β, highlighted. Scale bar is 50 nm. **(c)** Simultaneous measurement of crystalline islands and quasicrystalline nano–structures. Scale bar is 9 nm.

7.3.3 Pb nano–structures

A theoretical film where each of the planes is 100% occupied by Pb can be modelled. Figure 7.13(a) shows each layer superimposed on top of each other. Each is coloured with respect to the plane/shell which explains their adsorption sites (Figure 7.6), with the exception of the fourth layer, which is coloured purple to distinguish it from the second layer. Fourth layer atoms are also enlarged for clarity. Labelled are the experimental motifs M_9 and M_{10}. This model film produces areas of high and low atomic density, as evidenced by the fourth layer atoms either stacking on top of the previous layers, or by sparse patches which can extend down to the first Pb layer. A colourmap of the film illustrates this. Figure 7.13(b) shows areas of low and high Pb density in z, where the scale goes from blue to red respectively. The individual triangular shaped protrusion in red are the fourth layer triangles with edge length 0.96 nm. Three of these triangles form motif 10, which is labelled. Also highlighted is motif 9. M_{10} and M_9 from Figure 7.11(a) are also included

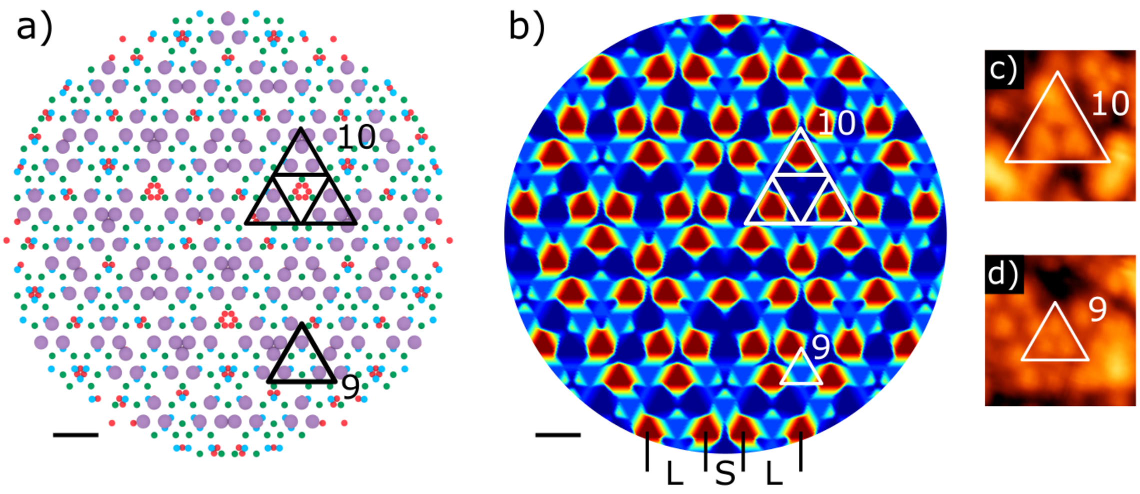

Figure 7.13: **3–fold Pb nano–structures:** **(a)** A model film of all four Pb layers. Highlighted are motifs 9 and 10. Colour scheme is as other figures, with the exception of the final layer, which is coloured purple. **(b)** A colourmap of **(a)**, indicating areas of low and high density (blue to red respectively). Labelled are M_9 and M_{10}. Individual protrusions form a Fibonacci sequence. **(c)** Enlarged view of M_{10}. **(d)** Enlarged view of M_9.

for comparison as enlarged views in (c) and (d) respectively.

The relatively isolated nature of each of the high density triangles indicates a strong distinction between a film of 3D nano–structures and a multi–layer film (as in the 5–fold system). Each red triangle in Figure 7.13(b) has, on average, a hollow of roughly 0.1 nm^3 adjacent to at least two of its edges, whilst the cavity at the centre of M_{10} is $\sim$0.5 nm^3. Furthermore, each triangle can be used as a basis in a Fibonacci chain, with an example highlighted on Figure 7.13(b). This, combined with the FFT from Figure 7.11(a), shows that the distribution of these nano–structures is quasiperiodic.

Figure 7.14 shows a 3D STM image of an area from Figure 7.11(a). Marked with a white ring is M_{10}. An arrow points to a triangular protrusion analogous to those in Figure 7.13(b). Similar protrusions (either whole triangles or with a vertex missing) are distributed throughout the image. The beginnings of the crystalline islands are visible as the darker red areas. Further experiments holding the substrate at raised temperatures could allow a homogenization of the film (in essence recreating the colourmap in Figure 7.13), whereby the Pb which creates the crystalline islands can more readily diffuse to quasiperiodic adsorption sites.

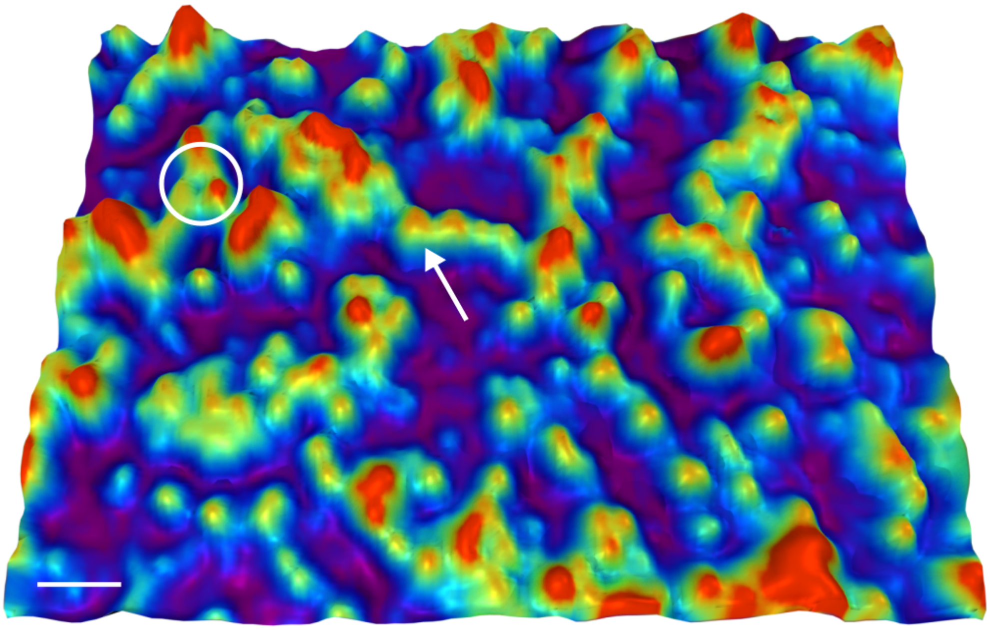

Figure 7.14: **3D view of 3–fold Pb nano–structures:** A 3D representation of a section of Figure 7.11(a). Circled is M_{10}. An arrow indicates one of the small triangular protrusions in Figure 7.13(a,b). Scale bar represents 5 nm.

7.3.4 Pb Growth Mode

To understand the specific nature of the growth mode of Pb here, it is pertinent to compare this system with metallic adsorption on 5–fold *i*–Ag–In–Yb. On the 5–fold surface, where multi–layer systems are formed, Pb and Bi form ‘under’ and ‘inter’ layers which energetically stabilise the films due to a minimisation of nearest neighbour distances. Under–layers are formed underneath the first layer, whilst inter–layers are those between already established layers (i.e. first and second). These layers are unobservable by STM, but are confirmed by Density Functional Theory (DFT) [67, 157]. As a result, the relationship between deposition time and coverage observed by STM is non–linear.

On the 3–fold surface, coverage has been defined here as the fraction of the total available adsorption sites which are filled for each plane. For each layer, the x–y density of the corresponding model plane is calculated. This density is used to calculate the maximum number of sites available over a certain size area (60×60 nm^2) for each layer, defined as a monolayer. Then, the ratio to this maximum is measured for each layer from

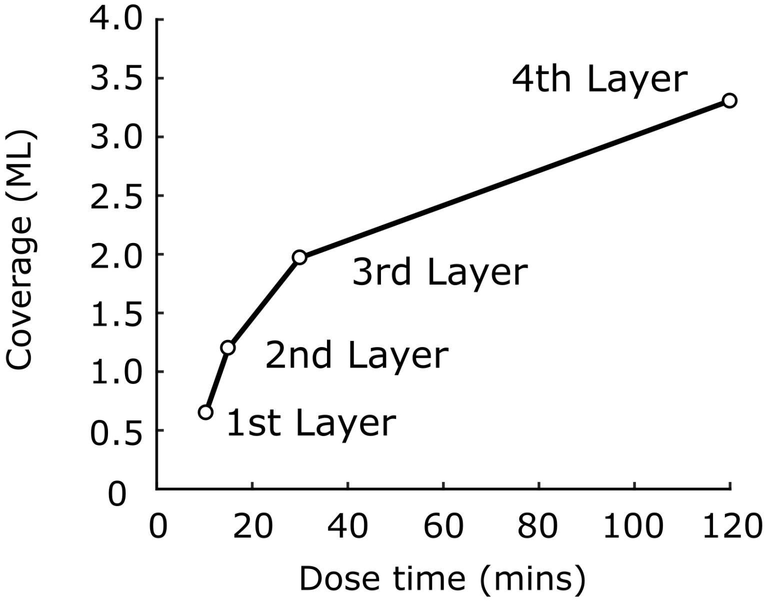

Figure 7.15: **Coverage relationship of Pb on 3–fold $\boldsymbol{i}$–Ag–In–Yb:** The relationship between deposition time and observed coverage by STM. Each layer is labelled with reference to its observation by STM.

the STM images. This method ensures that the contribution from each layer to the total coverage of the film is considered, and neglects any additional sites. Figure 7.15 shows the relationship between the Pb film coverage and the deposition time. Each layer has been labelled. Similar to the 5–fold orientation, we see a non–linear relationship. The potential explanation for this will be discussed in the next section.

Nearest Neighbours

Considering the argument of inter–atomic distances stabilizing films in the 5–fold system, we can look to nearest neighbour (NN) distances within the 3–fold system to explore the non–linear coverage relationship. To do so, the majority of the model film in Figure 7.13(a) can be deconstructed into an arrangement which mimics the Cd–Yb cluster shell geometries. Figure 7.16(a) shows a surface–centred Cd–Yb cluster, which has been truncated equatorially. The 5th, 4th, and 3rd shells are shown as truncated polyhedra. Each Pb layer has been placed at the positions which they ‘occupy’ considering the model planes

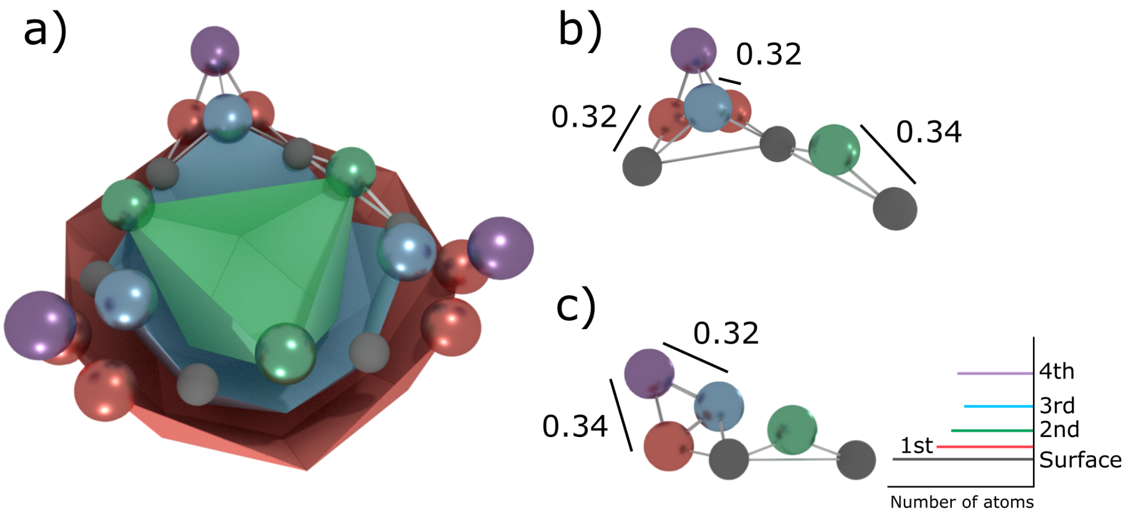

Figure 7.16: **3–fold Pb building block:** **(a)** A truncated Cd–Yb cluster with 3rd, 4th, and 5th shells visible. Pb atoms decorate each shell according to their placement in the model film. Colour scheme is as previous. Grey atoms are surface Cd atoms. **(b)** View of a section of **(a)** with nearest neighbour distances labelled. **(c)** Side–view of **(b)**, with a section of the planar model adjacent showing the relative heights of each layer. Nearest neighbour distances are labelled.

that explain their adsorption positions i.e. the vertices of these shell polyhedra. The colour scheme is as previous for each layer. Surface Cd atoms are in grey. The fourth layer (purple atoms) do not occupy positions explained by the surface truncated cluster, rather, the individual sites originate from three clusters centred below the surface plane (each 'providing' a site for a single atom). This arrangement of all four layers produces M_9 as seen in Figures 7.11(a,d) and 7.13(a,b,d). Likewise, the first layer M_1, second layer M_4, and third layer M_6 motifs are also constructed. The contribution of this 'building block' to other motifs will be discussed later.

Figure 7.16(b) shows a section of the building block, with nearest neighbour distances labelled between various layers and the substrate. All values are on the nm scale. Similarly, Figure 7.16(c) shows a side–view of this section, with further NN distances marked. Adjacent is a representation of the Cd–Yb planar model for each of the Pb layers. The labelled NN values can indicate whether the Pb will interact with the substrate, or other Pb layers. If a nearest–neighbour (NN) distance is larger than that of crystalline Pb (0.32 nm), then it is likely that a stabilising layer is needed. As indicated on Figure 7.16, all

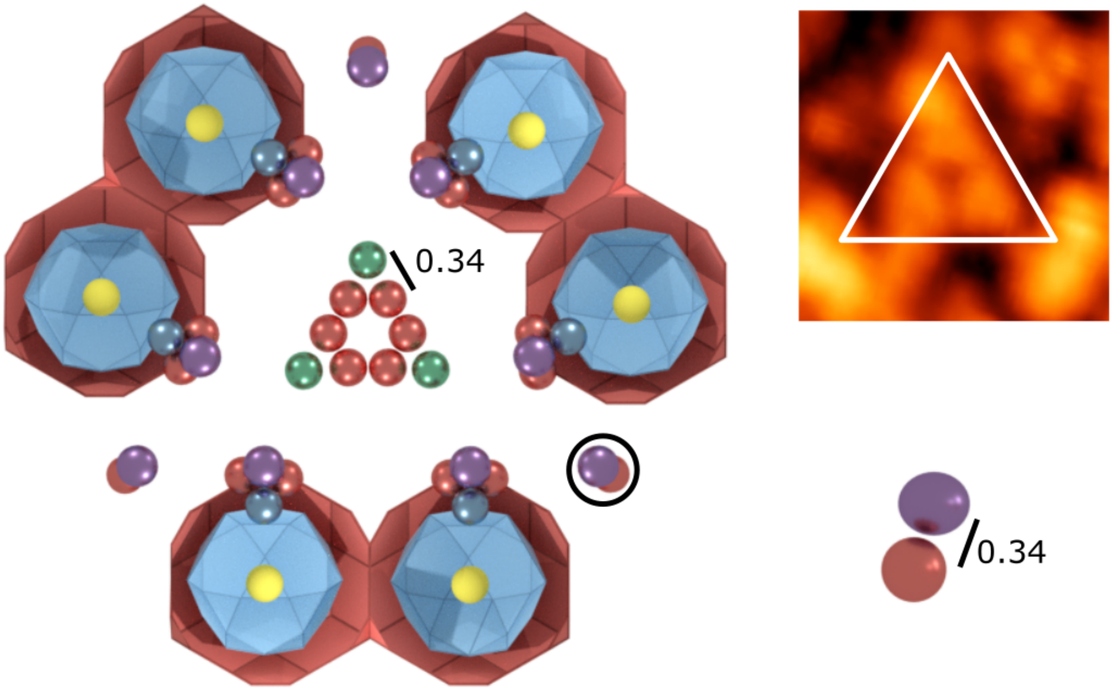

Figure 7.17: **Motif 10 model:** Motif 10 (STM image, right) is constructed using six building blocks from Figure 7.16(a) and three additional ‘units’, one of which is highlighted. These additional units are stabilised by the first Pb layer, as shown adjacent by a labelled side–view and NN distance. The centre of motif 10 shows another arrangement between the first (red hexagon) and second (green triangle) layers. The NN distance marked shows their interaction.

values are within range of this value.

This building block can explain ∼ 85% of the sites in the film. The remaining sites can be explained by isolated interactions between each of the layers. Figure 7.17 shows a model of M_{10}, including the contribution of the building block to its construction. The cluster centres are marked by golden spheres. Each building block ‘donates’ a single fourth layer atom, creating two vertices of the smaller triangles that form M_{10}. The remaining vertices (one is circled) are simply fourth layer atoms which bond directly with the first layer. A side view is shown adjacent, with a NN distance labelled. Likewise, the centre of M_{10} contains a first layer hexagon, with a second layer triangle on top. The NN distance between these two arrangements is labelled. Again, values are on the nm scale. The

Inter–layer distance (nm)	
Layers	NN
S–1	0.32*
S–2	0.34*
S–3	0.40
S–4	0.58
1–2	0.34*
1–3	0.32*
1–4	0.34*
2–3	0.60
2–4	0.82
3–4	0.32*

Intra–layer distance (nm)			
Layer	NN_1	NN_2	Average
1	0.30*	0.97	0.63
2	0.60	0.97	0.78
3	0.52	1.04	0.78
4	0.60	0.97	0.78

Table 7.2: **Nearest neighbour inter– and intra–layer distances of Pb:** (Left) Table of values for distances between each layer. Highlighted with asterisks are values which are close to the nearest neighbour value for crystalline Pb. (Right) Intra–layer distances. NN_i refers to distances which are observed with equal regularity.

remaining $\sim$ 15% of the film can be explained by similar structures which are stabilized by previous layers.

A comparison of specific inter–layer and average intra–layer distances is presented in Table 7.2. Here, each layer is noted by its integer, and the substrate by an S. Distances have been calculated using the model planes. An average value for the intra–layer distance is calculated as, for each model plane, there are two 'NN' separations which are observed with equal regularity. The same is not required with the inter–layer calculations. With the exception of the first layer, each layer is stabilized exclusively (in terms of NN distances) by previous layers, or the substrate, as opposed to intra–layer, x–y interaction. This suggests that stabilising layers are not necessary within this system.

If this is the case, then the non–linear deposition/coverage relationship may be due to a reduction in the sticking coefficient of the film. As previously mentioned in section 7.1, the Yb sites of the substrate are particularly reactive. The sticking coefficent of the surface may then be proportional to the 'capping' of Yb at the surface, so that once the first layer is complete and the substrate is covered – approximately at the inflection point between the third and fourth layers, Figure 7.15 – the sticking coefficient of the system decreases. This also may be due to the quasicrystalline nature of the film. The number of available adsorption sites will decrease as each unique layer is filled, unlike upon a dense homo/hetero–epitaxial interface.

Relative densities

The growth of Pb cannot be explicitly defined in terms of the three growth modes explained in section 3.1. The Pb grows in z after an initial wetting layer, as in the Stranski–Krastanov mode. However, the first layer does not reach 100% coverage until the third layer is well established. Likewise, the 'islands' on top of the first layer in this case do not prioritize adsorbate–adsorbate interaction, as each successive layer is a quasicrystalline allotrope. Neither is the growth mode Volmer–Weber, as, although we see isolated 3D structures, again, their structure must be dependent on a strong interaction with the substrate potential. It may be that, at room temperature, the Pb is grown in a kinetically limited, metastable state, and that adequate thermal energy upon adsorption may allow 'typical' growth as defined by an adsorbate film in equilibrium.

The suggestion from experiment and the model NN distances is that growth is energetically preferred in z rather than x–y. As the adsorption sites are explained by planes of the Cd–Yb system, the preference for out–of–plane growth to in–plane growth can be considered in terms of plane densities. If we consider an equally sized 3D slab of planes in both the 5–fold and 3–fold orientations, then a potential motivator for the two different Pb growth modes is found. Here, there are less atoms per plane, but more planes per nm in z for the 3–fold system i.e. there are more potential sites for adsorption along z rather than in x–y. This may explain why Pb atoms in the second layer adsorb at the 'unstable' glue sites. To speculate, it may be that if the 3–fold orientation is truncated with no relaxation or reconstruction (as is the case), then there may be some directional energy potential created which is minimized by growth along z, as would be expected in the bulk.

7.4 Summary

The clean 3–fold *i*–Ag–In–Yb surface has been revisited with respect to the rhombus tiling. In agreement with the Cd–Yb model, cluster centres at the surface can be linked by tiles, where the vertices of tiles coincide with cluster centres. This practical application highlights the usage of the 3–fold rhombus tiling, as opposed to existing simply as a geometric construction.

Pb was dosed upon the clean surface over a range of coverages. As with previous studies, the growth of Pb appears templated by a surface potential, with Pb atoms occupying sites which can be explained by planes of atoms in the Cd–Yb model. The specific growth mode is unique to this system, with substrate–adsorbate interaction clearly preferred, but with quasi–island growth observed. As a result, Pb nano–structures are grown, which are indicative of the Cd–Yb cluster model.

Further deposition of Pb lead to crystalline islands, consistent with previous work [67, 157, 162]. Potential further research into this system could include fine–tuning the growth process, investigating the properties of the Pb structures (electronic, plasmonic, catalytic), or dosing further atomic or molecular species to assess reactivity/unique templating i.e. utilising the hollows as 'seed' points for growing quasicrystalline thin films.

Chapter 8

2–fold *i*–Ag–In–Yb: clean surface and Pb deposition

In this chapter, new high resolution STM images of the 2–fold *i*–Ag–In–Yb surface are presented and are compared to the Cd–Yb model. These images show different structural features to those previously published – attributed to the STM tip condition. Furthermore, Pb has been dosed on the surface to compare with the other high symmetry Pb/*i*–Ag–In–Yb systems. Here, Pb appears to adopt the surface structure, as opposed to being explained by Cd–Yb bulk planes, as with the other systems.

8.1 Introduction

Previous research concerning the 2–fold surface of the *i*–Ag–In–Yb quasicrystal has led to its description in terms of a bulk truncation of the Cd–Yb model. As with the other high symmetry orientations, its LEED pattern is discrete, and indicative of the surface symmetry, i.e. 2–fold [156]. STM gives step heights of $S = 0.27$ nm and $L = \tau S = 0.45$ nm, which are consistent with the distribution of cluster–centre planes in the Cd–Yb model. Therefore, the surface structure can be explained, as with the other orientations, by dense planes of atoms intersecting Cd–Yb cluster centres.

However, unlike the 5–fold and 3–fold surfaces, atomic resolution of the 2–fold surface was not achieved by STM [66, 154, 156]. Figure 8.1(a) shows a section of the surface observed by STM from a previous report. A row structure is clearly seen, which was compared to the distribution of the 5th shell of the Cd–Yb cluster, Figure 8.1(c). This

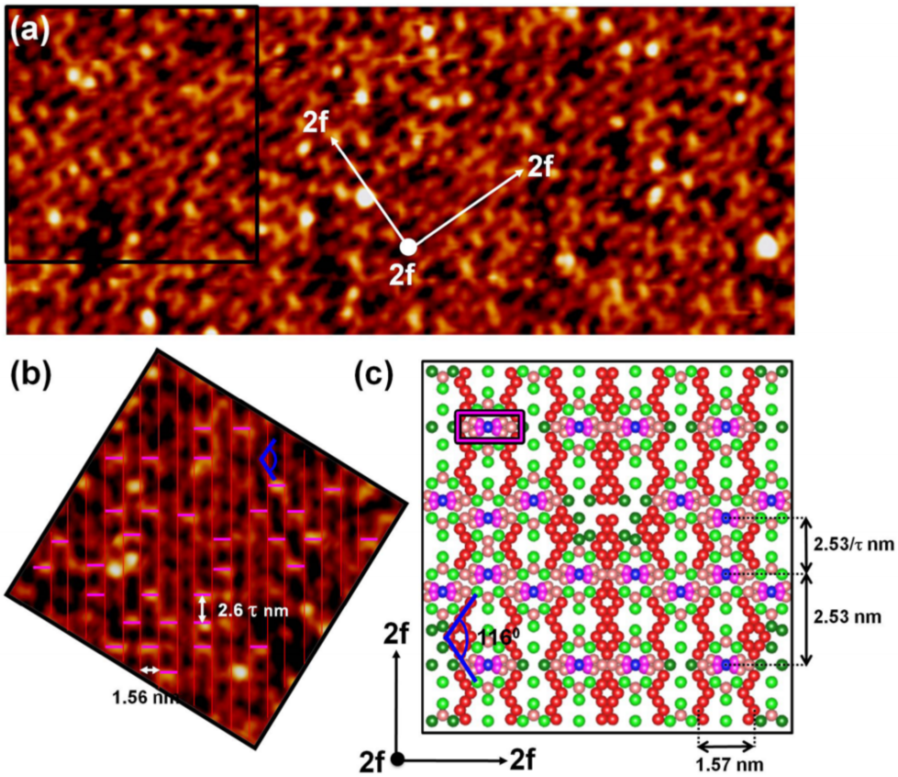

Figure 8.1: **Previous results from the 2–fold *i*–Ag–In–Yb surface:** **(a)** STM image of the 2–fold *i*–Ag–In–Yb surface. Highlighted are the directions of the 2–fold vectors. A black square indicates an area enlarged in **(b)**. **(b)** The row structure, protrusions, and zig–zag nature of individual rows are compared to the Cd–Yb model. **(c)** The cluster–centred atomic plane used to explain the surface. Cluster centres are blue, 5th shell atoms are red, 1st shell are pink, 2nd, 4th shell are light pink, whilst Yb atoms are green – glue atoms are dark green. Reproduced from [156].

shell forms zig–zag rows separated by 1.57 nm. The 'twist' angle i.e. the angle between zig and zag, matched well with the model value. Isolated protrusions are also observed, separated by τ–scaled distances along the direction parallel to the row structure. These were attributed to the 1st shell, with the relatively inhomogeneous distribution attributed to the partial occupancy of these sites within the model used[1] [156, 158–160]. As large terraces were found of comparable size to the other high symmetry directions, the stability

---

[1] The Cd–Yb cluster contains a dynamic tetrahedron as its 1st shell. The atomic model used approximates its position by a partially occupied dodecahedron (occupancy = 0.2).

and surface free energy of the 2–fold surface was considered comparable to the 3–fold and 5–fold orientations.

In the *i*–Ag–In–Yb system, each of the high symmetry surfaces were found to intersect with cluster–centre planes [66,154,156]. Similarly, step heights on each surface were linked to cluster centres along the relevant direction. However, along the 3–fold and 5–fold orientations, these cluster–centre planes were not the most dense. The stability (and therefore selection) of each of these surfaces was related not to overall atomic density, but to the In/Yb density. Indeed, along these two directions, the surface planes contained ∼90% In/Yb [156]. Along the 2–fold orientation however, the densest planes coincide with the cluster–centre planes, with a relatively even surface composition ($Ag_{31}In_{42}Yb_{27}$).

Before this work, there have been no adsorption studies on the 2–fold surface. Here, new STM images will be presented which offer atomic resolution of the surface. Rather than the zig–zag structure observed previously, individual protrusions can be linked directly to the 4^{th} shell of the Cd–Yb cluster, which has an occupancy of 80% In [155]. It is proposed that the bright protrusions are In atoms, which appear to form rows 'on–top' of a Yb distribution. The surface has also been used to template the growth of Pb. Here, as opposed to the other surfaces in the *i*–Ag–In–Yb system, Pb appears to grow epitaxially in a layer–by–layer fashion – that is, mimicking substrate–specific adsorption positions over each of the layers. Further Pb deposition results in a rough system, with crystalline islands aligned along high symmetry directions of the substrate.

8.2 Experimental Details

The 2–fold surface of an *i*–Ag–In–Yb QC was polished with diamond paste of successively finer grades (6–0.25 μm) before washing in methanol. After insertion into a UHV chamber, the sample was cleaned by cycles of sputtering and annealing. The surface was sputtered for 30 minutes with Ar^+, before annealing for 2 hours at 700 K. Pb was dosed at a constant flux of $\sim 5 \times 10^{11}$ atoms $cm^{-2}s^{-1}$ over a range of coverages, using a Focus EFM 3 evaporator.

8.3 Results

8.3.1 Clean Surface

Figure 8.2(a) shows an STM image taken from the clean 2–fold i–Ag–In–Yb surface, with increased resolution compared to the previous report [156]. The clean surface here primarily consists of bright protrusions which are arranged in both horizontal and vertical rows, with finer arrangements between rows sometimes observed. The same image is shown in Figure 8.2(b), where the rows have been highlighted. There are no aperiodic sequences observed. The horizontal separation of vertical rows is $\mathrm{R}_H = 1.27 \pm 0.04$ nm. Occasionally, small perturbations also occur – a purple oval highlights an example in Figure 8.2(b). This separation is measured as 0.94 ± 0.04 nm. The vertical separation of horizontal rows are either $\mathrm{R}_{V1} = 2.06 \pm 0.07$ nm or $\mathrm{R}_{V2} = 2.4 \pm 0.1$ nm. The ratio of these vertical row values is not related to τ, nor do the vertical rows form a Fibonacci sequence. However, the ratio of $\mathrm{R}_{V1}/\mathrm{R}_H$ gives 1.59 ± 0.08. The highlighted rows in Figure 8.2(b) are placed at an average separation between these values (2.2 ± 0.1 nm). Also highlighted within a rectangle is a rectangle with a central protrusion. The two edge lengths of this formation correspond to the horizontal and vertical row (R_{V2}) separations. The diagonal direction (i.e. bottom left to top right, or vice versa) of the rectangle is at $59 \pm 0.1^\circ$ to the horizontal, which corresponds to the angle between the 2–fold and 5–fold axes, as indicated by a set of vectors overlaid on Figure 8.2(b). The average distance from corner to corner of any rectangle is 2.6 ± 0.2 nm – this value is dependent on whether a rectangle is formed by a vertical separation of R_{V1} or R_{V2}.

The FFT of the data from Figure 8.2(a) is shown in Figure 8.2(c). The spots in the FFT have been highlighted by coloured circles to indicate which part of the surface they represent. The row separations (both horizontal and vertical) give rise to purple–circled spots arranged in a diamond. There is no evidence of τ–scaling of these spots in either direction, in agreement with the seemingly periodic rows observed. A weak set of spots appearing at double the vertical separation are also highlighted in purple. The row separations calculated from the primary spots give: $\mathrm{R}_{H-FFT} = 1.25 \pm 0.05$ nm and $\mathrm{R}_{V-FFT} = 2.19 \pm 0.08$ nm. These values agree with the measured R_H, and the average of R_{V1} and R_{V2}. Additionally, three sets of τ–scaled spots are highlighted by white spots. Their angle from the horizontal is $30 \pm 1^\circ$, corresponding to the 5–fold direction in real–space ($90^\circ - 31.7^\circ = 58.3^\circ$, the angle between the 2–fold and 5–fold axes).

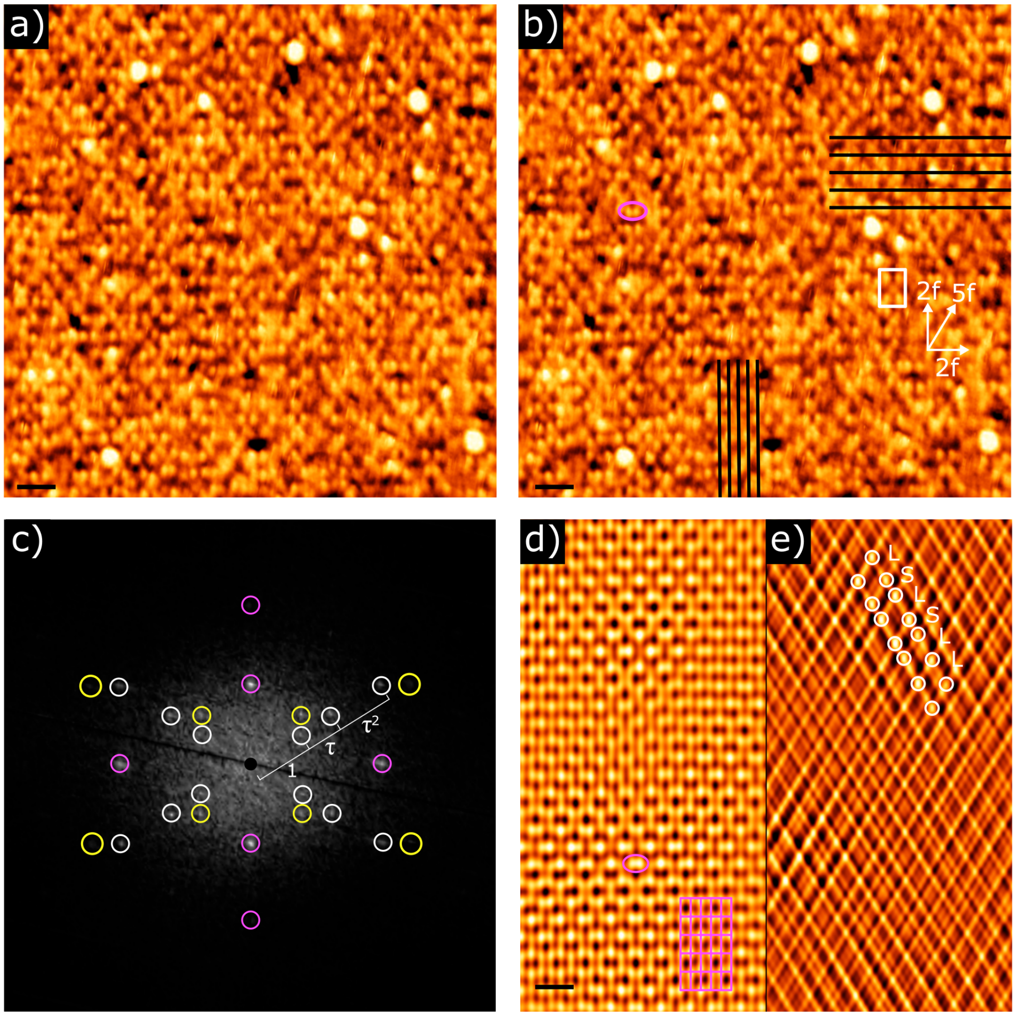

Figure 8.2: **Clean 2–fold $\boldsymbol{i}$–Ag–In–Yb surface:** **(a)** STM image (V_b = 800 mV, I_t = 0.309 nA) of the clean 2–fold i–Ag–In–Yb surface. **(b)** Same image as **(a)**, with horizontal and vertical rows highlighted. Also marked is a rectangular feature, and a closely separated dimer. Vectors indicate the high symmetry axes of the surface. **(c)** FFT of **(a)**. Spots are highlighted which are related to specific features of **(a)**. **(d)** Left: Inverse FFT of purple spots in **(c)**. A lattice highlights the row separation, with an oval highlighting a close dimer. Right: Inverse FFT of white spots in **(c)**. A Fibonacci sequence links high intensity spots along the 5–fold axis. All scale bars represent 5 nm.

Figure 8.2(d) shows the inverse FFT created by the purple spots, in addition to the spots circled in yellow, where a purple lattice indicates the periodic row structure. The

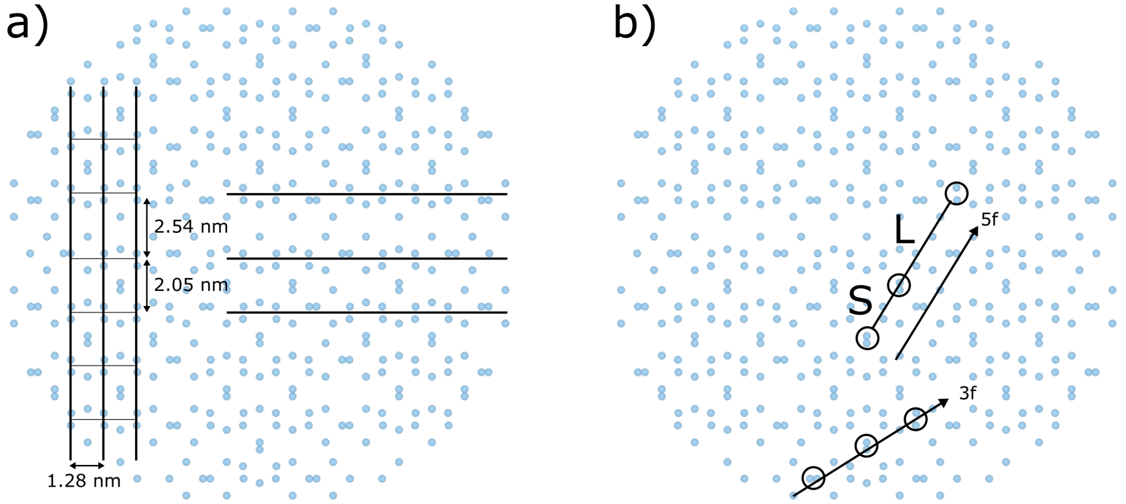

Figure 8.3: **2–fold *i*–Ag–In–Yb surface model: (a)** The 4th shell of the surface plane used to described the 2–fold *i*–Ag–In–Yb surface. Vertical and horizontal rows are highlighted, formed by dimers. Their separations are marked. **(b)** Same as **(a)**, but with circles indicating dimers oriented in the 5–fold and 3–fold direction.

yellow spots induce a slight spatial perturbation in the rows and a modulation in intensity in the inverse FFT. Their origin will be discussed later. The inverse FFT calculated from the white spots is shown in Figure 8.2(e). Here, along the 5–fold direction, high intensity spots are separated by a section of the Fibonacci chain. The length scales of the chain segments are $L = 3.89 \pm 0.06$ nm, and $S = 2.52 \pm 0.08$ nm. This S value corresponds to the length–scale of the diagonal of the highlighted rectangle in Figure 8.2(b).

Using the real–space measurements and the FFT, the surface structure observed by STM can be interpreted by considering the 4th shell of a surface truncated Cd–Yb cluster. Figure 8.3 shows a model of the surface plane, with only the 4th shell atoms shown. Marked are horizontal and vertical row locations, where the horizontal model row separation is $\mathrm{R}_{HM} = 1.27$ nm, and the two vertical rows are $\mathrm{R}_{V1M} = 2.04$ nm, and $\mathrm{R}_{V2M} = 2.54$ nm (where M = model). These rows form a modulated rectangular lattice which matches the dimensions measured by STM. At each vertex are closely separated dimers. It is therefore proposed that these dimers appear as singular protrusions in STM. A rough 'unit cell' can therefore be composed by the rectangular formation in Figure 8.2(b), with dimers at each of its vertices. This may explain why there is no τ–scaling observed in the FFT along the

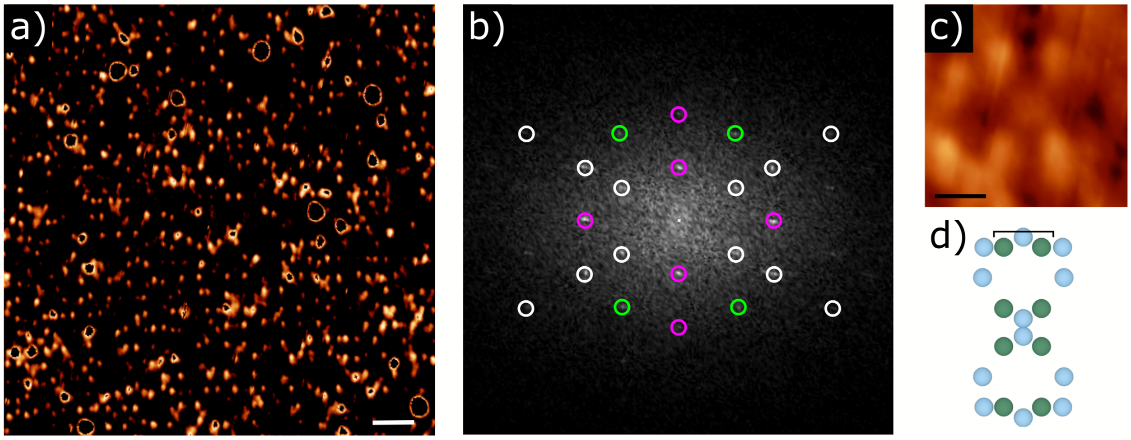

Figure 8.4: **2–fold surface contribution:** **(a)** STM image from Figure 8.2(a), filtered so that only the bright protrusions corresponding to the 4th shell model plane are visible. Scale bar is 5 nm. **(b)** FFT of **(a)**, with coloured spots following the same colour scheme as Figure 8.2(c). Green spots are along the 3–fold axis in real–space. **(c)** Enlarged view of a rectangular motif. Scale bar is 1 nm. **(d)** Model of **(c)**, including Yb atoms (green).

2–fold symmetric axes. Figure 8.3(b) shows that these dimers can be separated along the 5–fold axes by a Fibonacci sequence of the same scale in Figure 8.2(e). The model gives values of $S = 2.41$ nm (±4%), and $L = 3.85$ nm (±1%). Therefore, this model plane can explain the bright features observed by STM.

The chemistry of the 4th shell protrusions (and the reason why they are observed primarily over any other shell) can be inferred by considering the occupancy and density of this shell with reference to the Cd–Yb model. i–Ag–In–Yb is isostructural to Cd–Yb, as previously stated, with Ag/In replacing Cd. The specific nature of this replacement is not known i.e. whether Ag occupies a specific vertex of the 4th shell, for example. However, the atomic occupancy of each shell is known in terms of an approximate ratio: the 4th shell contains ∼80% In, if not more [155]. Now, in terms of atomic density, the 4th shell represents ∼17% of the total atoms in the selected surface plane. Therefore, it is reasonable to speculate that roughly 14–17% of the surface plane contains In from the 4th shell.

Considering this, Figure 8.4 shows Figure 8.2(a) thresholded to show the bright protrusions covering ∼ 19% of the image area. It is speculated that these contributions are from In only. Figure 8.4(b) shows an FFT of Figure 8.4(a), with spots circled considering the same colour scheme as in Figure 8.2(c). Conspicuously, there are no yellow circled spots – and a set of green circled spots are more prominent. These are aligned 60 ± 4° to the horizontal, or 30 ± 2° in real space – corresponding to the 3–fold direction (31.72°). Dimers oriented along the 3–fold direction are highlighted in the model surface plane in Figure 8.3(b).

Therefore, the remaining structure of the surface must have some contribution from the other shells at the surface plane. Figure 8.4(c) shows an enlarged view of the rectangle feature in 8.2(b). At this scale, the contrast difference between the vertices of the rectangle and its centre are more obvious. Likewise, the centre protrusion appears more square–like than the vertices. Figure 8.4(d) shows a model schematic of the rectangle, where Yb atoms are also included. Here, an Yb square is predicted at the centre of the rectangle, fitting with the square centre of Figure 8.4(c). The marked distance between adjacent In–Yb dimers is given as 0.92 nm, which fits well with the observed perturbation in the vertical rows (±2%). It is therefore suggested that Yb atoms have some effect on the observed partial density of states at certain positions, or, at other positions, induce some spatial perturbation. These factors therefore may produce the yellow circled spots in the FFT in Figure 8.2(c). In general, therefore, the surface can be considered as a set of bright protrusions (In atoms) which appear to form a row structure, which sits on a 'base' of Yb atoms. This row structure is consistent the previous report, with the exception here that different structural aspects of the surface (i.e. different Cd–Yb shell contributions) are resolved [156]. This yields a difference in row separation measurements.

The previous report studied bias dependency of the tip to the surface, finding none. Bias dependency was not explored here. The enhanced resolution of the clean surface compared to the original report may be due to the condition and shape of the STM tip.

8.3.2 Pb dosed surface

Pb grown on the 2–fold *i*–Ag–In–Yb surface differs from the 3–fold and 5–fold systems. Here, rather than Pb sitting at sites and heights which are explained by planes 'above' the surface, Pb appears to directly adopt the structure of the underlying substrate over multiple layers. The growth mode is again different to the other systems, with a modified Stranski–Krastanov type mode observed. A dense initial wetting layer is grown to 1 ML coverage, which appears to mimic aspects of the substrate structure. Afterwards, small structures at multiple heights grow upon the first layer along z. Their structure (at each height) also appears indicative of the substrate. Further coverage results in a rough film, with crystalline island–type growth, consistent with the other high symmetry systems [67].

The structure of each Pb layer on the 2–fold surface will be discussed here, and compared to Pb adsorption on the other high symmetry surfaces of *i*–Ag–In–Yb.

First Layer

Figure 8.5(a) shows an STM image taken after dosing the clean surface with Pb for 10 minutes. The coverage of Pb is approximately 0.6 ML, calculated by subtracting the area representing the substrate from the image. Rectangular features with edge lengths of R_H and R_V are often observed from the substrate – one example is highlighted within a white rectangle. The adsorbed Pb can be split into two categories dependent on resolution in STM – either individual Pb atoms, or, larger collections which appear as single protrusions. Examples of each are highlighted by white circles.

To understand the Pb adsorption sites, Pb motifs will be considered with reference to the model substrate. Figure 8.5(a) shows 4 Pb atoms arranged in a vertical line, highlighted by a white oval. The separation of these Pb atoms is 1.28 ± 0.08 nm. Also indicated in Figure 8.5(a) is a diamond, where each of the vertices are protrusions which, individually, appear larger than the atoms highlighted in the vertical chain. The edge lengths of the diamond are 2.40 ± 0.05 nm, and its horizontal and vertical diameter are 2.41 ± 0.04 nm and 4.01 ± 0.08 nm respectively. Both of these motifs can be related to a chemically non–specific model of the substrate. This non–specificity will be discussed later.

Figure 8.5(d) shows the surface model, where each of the Cd–Yb shells have been coloured blue to reveal adsorption sites of high symmetry. Cluster centres are coloured gold. Labelled are the vertical line and the diamond, in addition to other features discussed later. The adsorption sites of both model Pb structures can be categorised as either hexagon or triangle sites, shown in an enlarged view next to Figure 8.5(d), where they are abbreviated as H and T. These are characterised by the surrounding atomic symmetry, so that a hexagonal adsorption site is a site surrounded by six substrate atoms, etc. Using these as model adsorption sites, the separations of the Pb line and percentage difference to the experiment are 1.20 nm (±7%). The edge length, horizontal and vertical diameters of the model diamond are 2.41 nm (±1%), 2.53 nm (±5%), and 4.10 nm (±2%) respectively. The larger radius of the protrusions which form the diamond (in comparison to the single atoms forming a line) could originate from multiple Pb atoms which are adsorbing at closely separated hexagon and triangle sites, as shown in Figure 8.5(d). This may also cause the

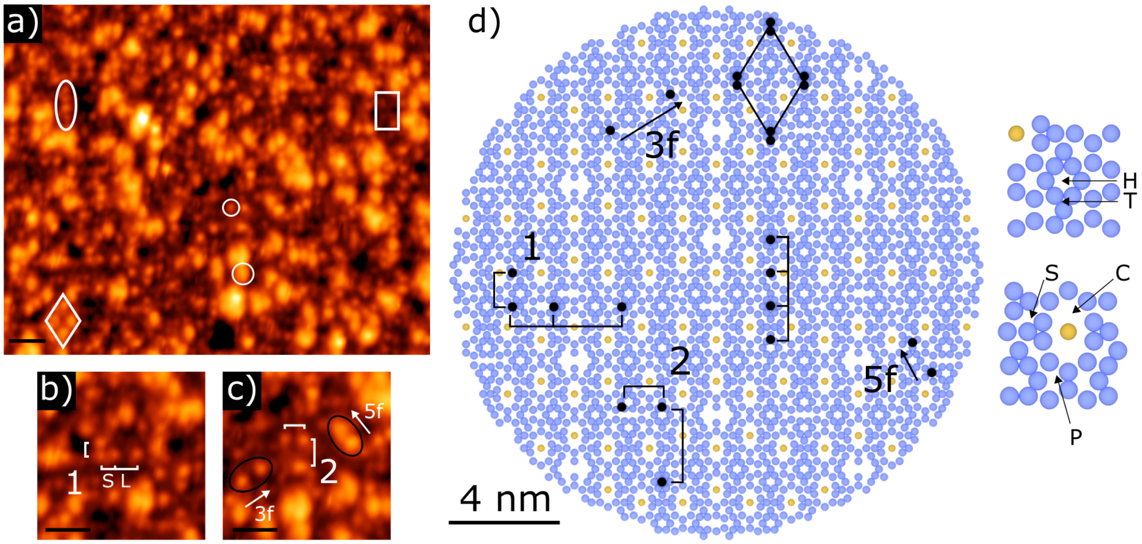

Figure 8.5: **Low coverage Pb on the 2–fold *i*–Ag–In–Yb surface:** **(a)** STM image ($V_b = -0.806$ mV, $I_t = 0.198$ nA) of the 2–fold *i*–Ag–In–Yb surface after dosing with Pb for 10 minutes. A white rectangle indicates a substrate rectangle. An oval highlights 4 Pb atoms. A small circle indicates a single Pb atom, whilst a larger circle shows a denser protrusion. A diamond indicates four Pb protrusions arranged in a diamond. Scale bar represents 5 nm. **(b)** Enlarged area of **(a)**. A Pb structure of atoms is highlighted with horizontal and vertical separations. Scale bar represents 5 nm. **(c)** Enlarged area of **(a)** Another Pb structure is highlighted. Dimers are marked which lie along the 3–fold and 5–fold axes. Scale bar represents 5 nm. **(d)** Model of the potential adsorption sites for the first layer of Pb. Blue atoms are the substrate, yellow, the cluster centres. Each of the highlighted structures in **(a, b, c)** are labelled. Adjacent are enlarged views of the hexagonal, triangular, pentagonal, square, and cluster centre adsorption sites.

variation in percentage difference between model and experimental values as calculated above.

Further examples are also consistent with this hypothesis. Figure 8.5(b) shows an enlarged view of (a). A Pb structure is labelled as '1'. The labelled vertical separation of 1 is 1.22 ± 0.05 nm, whilst the two horizontal values are $S = 1.49 \pm 0.07$ nm, and $L = 2.41 \pm 0.03$ nm. The ratio of L/S is 1.62 ± 0.08, or $\sim \tau$. A similar arrangement is marked in the model in Figure 8.5(d), with corresponding values for the vertical separation: 1.24 nm (±2%), $S = 1.57$ nm (±5%), and $L = 2.54$ nm (±5%). These horizontal isolated atoms are therefore τ–scaled. In addition to hexagonal and triangular adsorption sites, two atoms of motif 1 sit at pentagonal sites, with an example again shown adjacent to Figure 8.5, abbreviated as P. Again, this is characterised by the surrounding substrate atoms forming a pentagon.

Figure 8.5(c) also shows an enlarged view of (a), with a Pb structure labelled as '2'. The horizontal and vertical edge lengths of 2 are 1.5 ± 0.1 nm and 2.79 ± 0.05 nm. Again, the corresponding features are marked in Figure 8.5, with edge lengths: 1.57 nm (±4%) and 2.82 nm (±1%). These atoms sit at T and H sites. In addition, two sets of Pb atoms have been marked on Figure 8.5(c) which are oriented along the 3–fold and 5–fold axes. Their separations are 2.48 ± 0.04 nm and 1.54 ± 0.03 nm respectively. Corresponding sets have been marked on Figure 8.5(d) with 3–fold and 5–fold symmetry directions labelled, with separations of 2.54 nm (±2%), and 1.57 nm (±2%) respectively. Both sets sit at T and P sites.

As such, it is suggested that the Pb atoms are adsorbing at sites with high symmetry. These are labelled adjacent to Figure 8.5(d). In addition to the triangular, pentagonal, and hexagonal sites which have been discussed, a square site is also highlighted. Other potential sites include positions surrounding the cluster–centres. This is contrary to the other high symmetry *i*–Ag–In–Yb surfaces, where the structure of Pb layers were explained using planes 'above' the substrate. The potential explanation for this difference will be discussed later.

If indeed the growth mode is dependent on some aspect of the substrate structure, then a denser Pb layer than the 3–fold and 5–fold Pb systems will be observed. Higher Pb coverage shows that the Pb adopts the row–like substrate structure. Figure 8.6(a) is an STM image of the surface after dosing with Pb for 12 minutes. Here, the coverage is calculated as ∼0.8 ML. A clearly defined row structure is observed in the vertical direction. The start of the second Pb layer is highlighted by a white circle.

The FFT of the high coverage first layer is shown in Figure 8.6(b), taken after thresholding out the substrate contribution. Only 4 spots are visible, appearing along the 2–fold symmetric axes. No τ–scaling is observed, due to a lack of FFT spots. This behaviour is similar to the purple–coloured spots forming a diamond in the FFT taken from the substrate, Figure 8.2(c). Indeed, the lengths of the rows in real–space taken from Figure 8.6(b) are, for the horizontal: 1.22 ± 0.05 nm, and the vertical: 2.1 ± 0.1 nm. These values correspond with those measured from the In/Yb rows from the substrate in Figure 8.2. Therefore, it is suggested that in Figure 8.6(a) and similar to the image of the substrate, Figure 8.2, multiple Pb atoms are resolved as single protrusions, with the film growing in

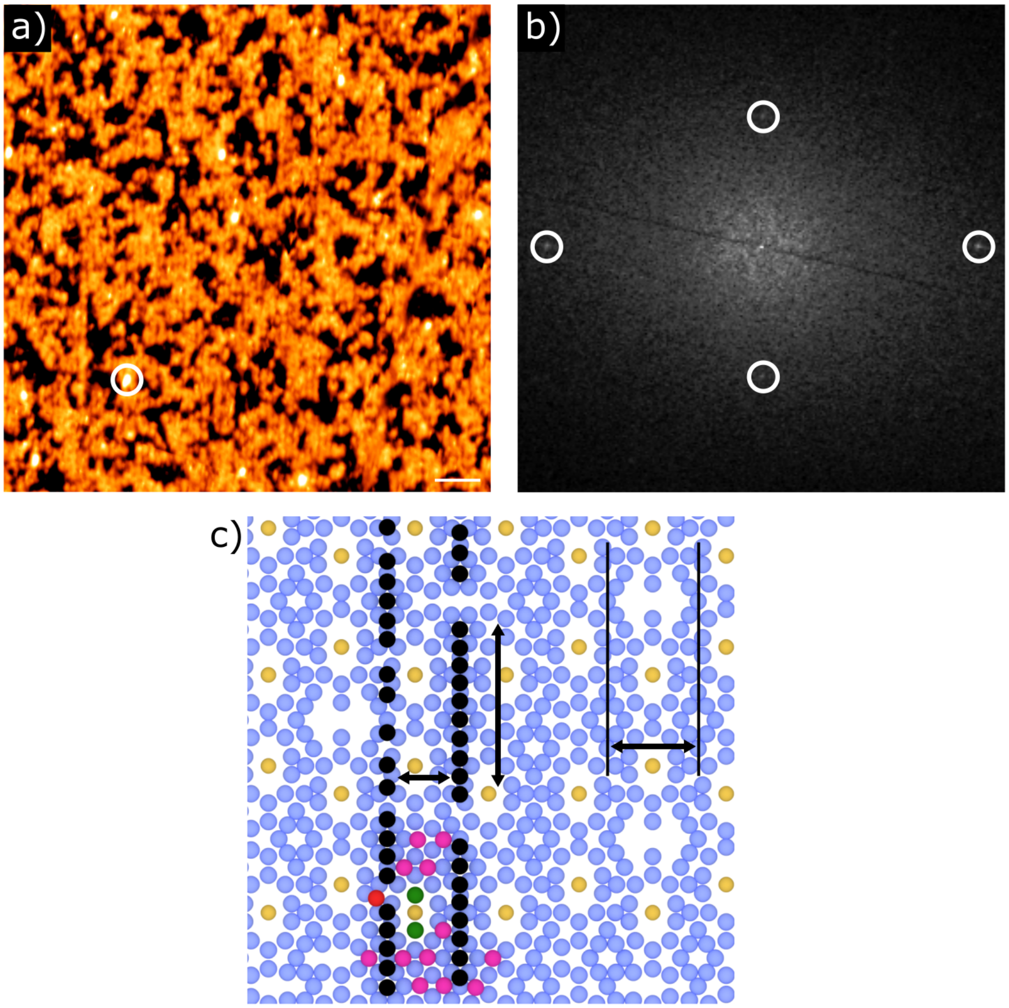

Figure 8.6: **High coverage Pb on the 2–fold i–Ag–In–Yb surface: (a)** STM image (V_b = -100 mV, I_t = 0.149 nA) of high coverage Pb from the first layer. A white circle highlights the start of the second layer. Scale bar is 8nm. **(b)** The FFT taken from **(a)**. Four spots are labelled with no τ–scaling. **(c)** A model of the first Pb layer. Prospective high symmetry T and H sites are occupied along two rows separated by 1.26 nm. A vertical separation of 2.2 nm highlights a section of a row between two gaps in high symmetry sites. A larger row separation is marked on the right–hand side.

a manner commensurate with the row structure of the substrate.

Figure 8.6(c) is a model of the first Pb layer on top of high symmetry sites along one of the 2–fold symmetry axes. Here, each hexagonal and triangular adsorption site is occupied along two rows. These rows are separated by 1.26 nm, marked by a set of arrows. This value fits with the horizontal rows in Figure 8.6(b), (±3%). Also labelled is a vertical separation of a section of one of the rows. This section is created due to gaps between the next hexagonal and triangular adsorption sites. Its length is 2.20 nm, in agreement with the vertical separation measured in Figure 8.6 (±5%). Whilst this section does not appear directly adjacent in the next row, sections of similar lengths and similar start/end points between parallel rows are observed throughout the model structure. This may lead to the corresponding vertical separation FFT spots. Likewise, the non–specific chemical nature of the model presumes a 100% occupancy of each hexagonal and triangular site. In reality, there may be preferred sites at the coverage in Figure 8.6(a) which generate this vertical separation in the FFT.

In Figure 8.5(d), other high symmetry sites were identified. At the bottom of Figure 8.6(c) several pentagonal sites are occupied, shown as pink atoms. These sites appear between the hexagonal and triangular rows, with a much lower frequency than the hexagonal and triangular positions (roughly 40% of the total hexagon and triangle sites). This difference in density of available sites may also play a role in the row structure observed. Cluster centre and square sites are also highlighted with green and red atoms, respectively. They appear with less regularity, and are situated between hexagonal and triangle site rows.

Hexagonal and triangular rows can occasionally be separated by 1.57 nm, as labelled in Figure 8.6(c). This row distance is not measured by STM, nor is it indicated in the FFT of Figure 8.6. The Cd–Yb model predicts these row separations appearing between ∼14% of the total rows. It is suggested then, that either these rows are at low enough occupancy that they do not appear in the FFT, or, that at higher coverage, Pb adsorbs at the rows containing pentagonal or cluster–centre sites, in–between hexagonal and triangular rows. This may lead to a dense structure which is not resolved by STM.

Second Layer

Figure 8.7(a) is an STM image taken after dosing the surface with Pb for 20 minutes. At this coverage, the first layer is almost completely filled, and two further layers are observed. The second layer appears to grow in a row–like structure, oriented along one of the 2–fold axes. A third layer is highlighted by a black circle. Horizontal row separations are marked on Figure 8.7(a) as $S/2$, S, and L. These give values of $S/2 = 0.66 \pm 0.05$ nm,

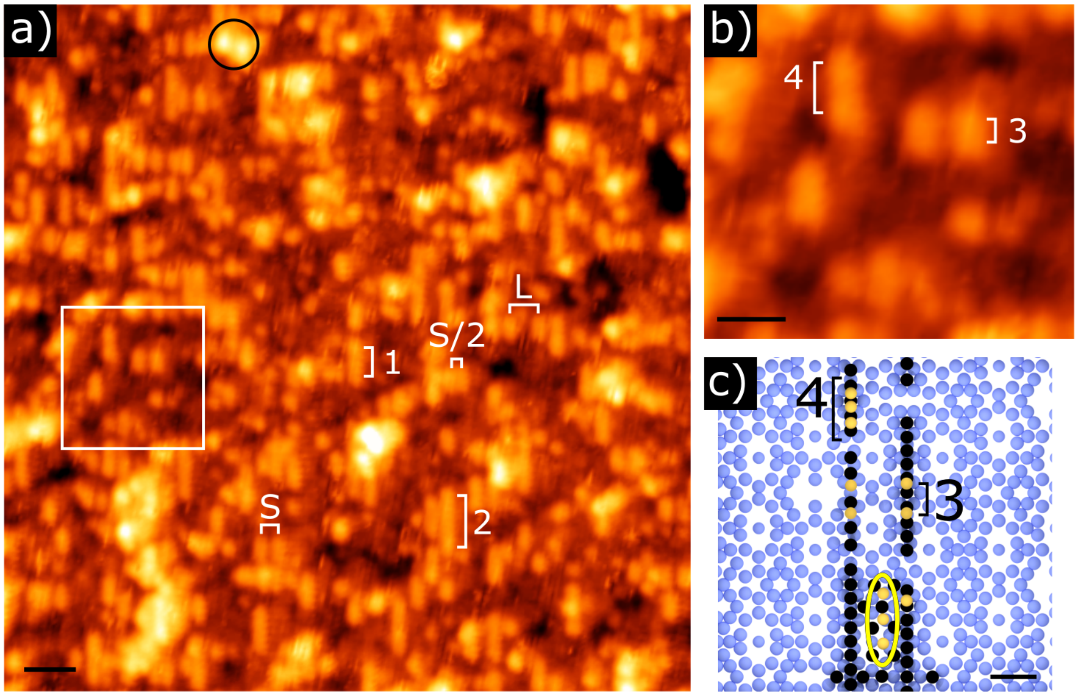

Figure 8.7: **Second Pb layer on the 2–fold *i*–Ag–In–Yb: (a)** STM image (V_b = 500 mV, I_t = 0.5 nA) of the second Pb layer. Rows are separated and marked by $S/2$, S, and L. Segments of rows are marked as 1 and 2. A white box indicates an area of interest shown in **(b)**. A black circle indicates the third layer. Scale bar is 4nm. **(b)** Enlarged view of **(a)**. 3 and 4 are distances noted in the main text. Scale bar is 2 nm. **(c)** Model schematic of the first (black) and second Pb (yellow) layers on the substrate (blue). Distances 3 and 4 from **(b)** are marked. Scale bar represents 1 nm.

$S = 1.26 \pm 0.06$ nm, and $L = 1.96 \pm 0.08$ nm. The relationship between S and L does not appear τ–scaled. Likewise, the smaller row separations are not S/τ. This will be discussed. The lengths of two row segments are marked as 1 and 2, giving values of 2.6 ± 0.1 nm and 4.1 ± 0.1 nm respectively. These segments are τ–scaled, giving a ratio of 1.6 ± 0.1.

Each of these separations and lengths match those of the previous layer. However, the preferred occupancy of hexagonal, triangular, pentagonal, square, and cluster centre–based adsorption sites of the first layer is not known. Therefore, directly understanding specific second layer adsorption sites with respect to an accurate structural model of the first layer is not possible. However, second layer separations can be compared to first layer separations, and as a consequence a rough model can be suggested. For example, the S row separation of the second layer is the same as the first layer horizontal row separation from Figure 8.6(a) (±1%), or, the R_H value from the substrate (±2%). Likewise, $R_H/2 = 0.64$ nm $= S/2$ (±3%). The vertical segments, 1 and 2, are related to the large vertical separation from the substrate $R_{\mathrm{V2M}} = 2.54$ nm, so that $1 = R_{\mathrm{V2M}}$ (±4%), and $2 = \tau R_{\mathrm{V2M}}$ (±1%). These structures and values may also be related to the segments of atoms produced in the vertical chains of the first layer, Figure 8.6(c).

The highly linear nature of the second Pb layer indicates an adsorption site network with similar geometry, which fits with the high density row structure of the first Pb layer. As such, it is suggested that the second layer Pb atoms are adsorbing on top of the first layer Pb rows, with a preference given to the hexagonal and triangular site rows. Figure 8.7(b) shows a collection of second layer Pb protrusions. Labelled as 3 is a single vertex from a rectangular feature. The marked length (i.e. the width of the protrusion forming the vertex) is 0.71 ± 0.02 nm. Likewise, marked as 4, is a length of 1.43 ± 0.03 nm. These features can be explained by the linear adsorption network suggested. Figure 8.7(c) shows a model of the first Pb layer (black) on top of the substrate (blue). These rows are formed along hexagonal and triangular substrate sites. Yellow atoms are second layer Pb, adsorbing at bridge sites in between two first layer Pb atoms. Both 3 and 4 are marked, giving distances and agreements with the experimental values of 0.66 nm (±6%) and 1.40 nm (±2%).

The $S/2$ row value measured from the second layer indicates that it is also possible for a Pb rows to lie between consecutive S rows – giving a finer structure than that observed in the first layer. These rows are analogous to atoms sitting within the pentagonal or cluster–centre rows in the first Pb layer. This also explains the lack of τ–scaling between $S/2$, S, and L, as, rather than adsorbing at quasiperiodically spaced separations (which are often chemically specific, see Mn atoms in Chapter 5) the Pb atoms are adsorbing in–between rows of high density, at sites of high symmetry. A yellow oval in Figure 8.7 highlights three second layer atoms which fall into a row structure between the two high density rows of the first layer as an example.

Third Layer

Dosing the surface with Pb for 20 minutes provides enough coverage to resolve some structure of the third Pb layer. Figure 8.8(a) is an STM image of an area which shows the third layer clearly. Marked is a rectangular arrangement of six Pb atoms, with horizontal

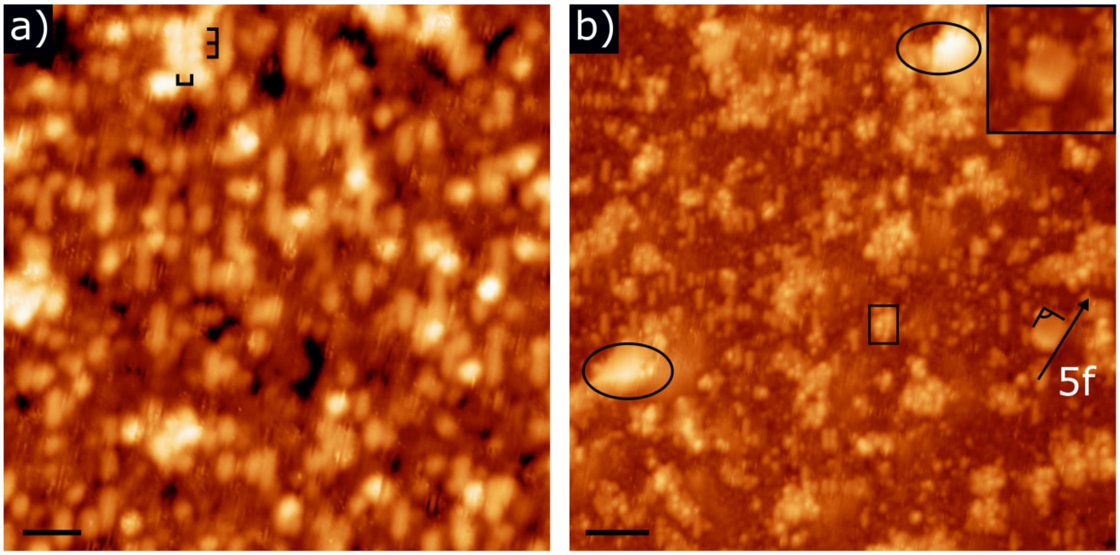

Figure 8.8: **High coverage Pb on the 2–fold *i*–Ag–In–Yb surface: (a)** STM image showing the first, second, and third layers of Pb. Marked are horizontal and vertical separations of a third layer feature. Scale bar is 5nm. **(b)** STM image showing the initial growth of crystalline islands, with examples of 3D growth circled with black ovals. The same rectangular feature from **(a)** is marked with a rectangle. The corner angle of an island is marked, which is itself oriented along the 5–fold direction, also marked. An inset shows an enlarged view of this feature. Scale bar is 10 nm.

and vertical separations labelled. The horizontal separation is 1.26 ± 0.06 nm, whilst the three pairs of horizontal dimers are each separated vertically by 1.23 ± 0.05 nm. Both of these values, again, are reminiscent of the previous layers and the substrate. The relatively sharp signal along the rows of this feature (in contrast to the dense second layer rows) suggests that these are individual atoms/dimers. Isolated third layer atoms are also observed, adsorbing on top of second layer rows.

Further Pb deposition shows that growth of the third Pb layer is preferred to the continuation/completion of the second layer. Figure 8.8(b) is an STM image of the surface after dosing Pb for 90 minutes. Highlighted by a rectangle is a similar feature to that observed in Figure 8.8(a). The coverage of the image appears similar to Figure 8.8(a), indicating that the incident Pb adsorbs preferentially to the second layer, rather than the first. This is different from a layer–by–layer growth scheme (Frank–van der Merwe). Likewise, it is expected under the Stranski–Krastanov growth mode that the islands on top of an initial wetting layer are dependent on adsorbate–adsorbate interaction, resulting in a minimum energy allotrope. Neither occur within this system. Rather, it appears that the sparse density of the second layer compared to the first is preferred for third–layer adsorption.

Marked by two ovals in Figure 8.8(b) are areas of Pb at larger heights than the third layer. Also marked with a set of axes is a crystalline island oriented along the labelled 5–fold axis of symmetry. The highlighted angle between two edges of the island is $92 \pm 1^\circ$, corresponding to a cubic growth plane. Further deposition of Pb results in a larger coverage of these islands upon the surface. The observation of crystalline Pb islands is consistent with previous results in the i–Ag–In–Yb system [67].

8.3.3 Pb on i–Ag–In–Yb

Comparison of growth modes

The adsorption of Pb on the i–Ag–In–Yb system has been reported for the 5–fold surface [67], whilst the 3–fold and 2–fold surfaces have been discussed in this work. The growth mode of Pb is different across each of the high symmetry surfaces. On the 5–fold surface, Pb grows in a strict layer–by–layer system, with each layer explained by planes from the Cd–Yb model. The 3–fold surface produces isolated nano–structures, with growth preferred along z. Each layer was again explained by planes in the Cd–Yb model. However, the 3–fold orientation has a greater density of planes along z, yet smaller in–plane atomic density than the 5–fold system. It was previously deduced that the nature of 'available' adsorption sites in the 3–fold system can be explained by, and is perhaps dependent upon, this variation in density.

The key difference between these systems and the Pb/2–fold surface is that here, Pb appears to grow in a modified Stranski–Krastanov type growth where, over several layers, Pb exhibits a structure related to the substrate. If the previous argument is followed, this difference in growth mode could be linked to the atomic density of the 2–fold surface. As previously discussed and unlike the other high symmetry directions, the 2–fold surface is formed from the densest planes available in the Cd–Yb model, which also coincide with the cluster–centre planes. This is partly due to the fact that the 2–fold surface is composed of all 5 shells from the Cd–Yb cluster – the other surfaces are formed only from the 3rd and 4th shells [66, 154, 156]. A rough atomic density per surface plane for each orientation gives, for the 2–fold: 7.9 atoms per nm^2, the 3–fold: 2.6 atoms per nm^2, and the 5–fold:

4.6 atoms per nm^2. Likewise, the number of planes over a 0.5 nm slab in z, for each orientation gives, for the 2–fold: 28 planes per nm, the 3–fold: 52 planes per nm, and the 5–fold: 36 planes per nm. So, here, the 2–fold surface has the highest in–plane density, yet the sparsest distribution of planes per nm in z in the i–Ag–In–Yb system.

The density of planes may be linked to the surface potential which dictates the adsorption sites for each of the high symmetry surfaces. If we consider the 3–fold and 5–fold systems, successive Pb layers have been matched to 'vacant' planes above the truncated surface in the planar Cd–Yb model. To speculate, the surface potential determining the growth in these systems must in some way represent these vacant planes, either through the truncation of the bulk, or the bulk itself. Upon the 2–fold surface however, the distance between neighbouring planes from the surface may be too large for this potential to act, discussed in the next section. Here, instead, it appears that adsorption sites with high symmetry are the driving force behind the structure of the film. Therefore, rather than a surface potential which dictates film structure, or a strong chemical adsorbate–substrate interaction (as seen with C_{60} on 2–fold Al–Pd–Mn), these sites may be attractive only so that incident Pb atoms may maximise their coordination number.

This theory is strengthened when considering the non–chemically specific substrate model used to explain the film structure. Here, triangular, square, pentagonal, and hexagonal adsorption sites have been identified which can describe the Pb adsorption sites. These sites are in fact composed of a mixture of all the Cd–Yb shells, in a non–specific manner i.e. a pentagonal site could be all Cd, or a mixture of Ag/In etc. As the model fits well with the experimental data, but considers no specific chemistry of the sites, it is suggested that the atom type of each adsorption site is not important.

Layer Heights

In previous work [67], and in Chapter 7, the heights of each Pb layer above the relevant i–Ag–In–Yb substrate have been compared to the planar Cd–Yb model. In doing so, the structure of each layer has been explained using planes of matching heights. The same method has not been employed here, as the heights and structure of the observed Pb layers do not match Cd–Yb planes above the surface termination. Figure 8.9(a) shows the planar Cd–Yb model along the 2–fold orientation. Figure 8.9(b) shows a histogram taken from Figure 8.5, of the height difference between the first layer and the substrate, ~ 1.1 Å. Figure 8.9(c) shows the histogram taken from Figure 8.7(a), which shows the difference

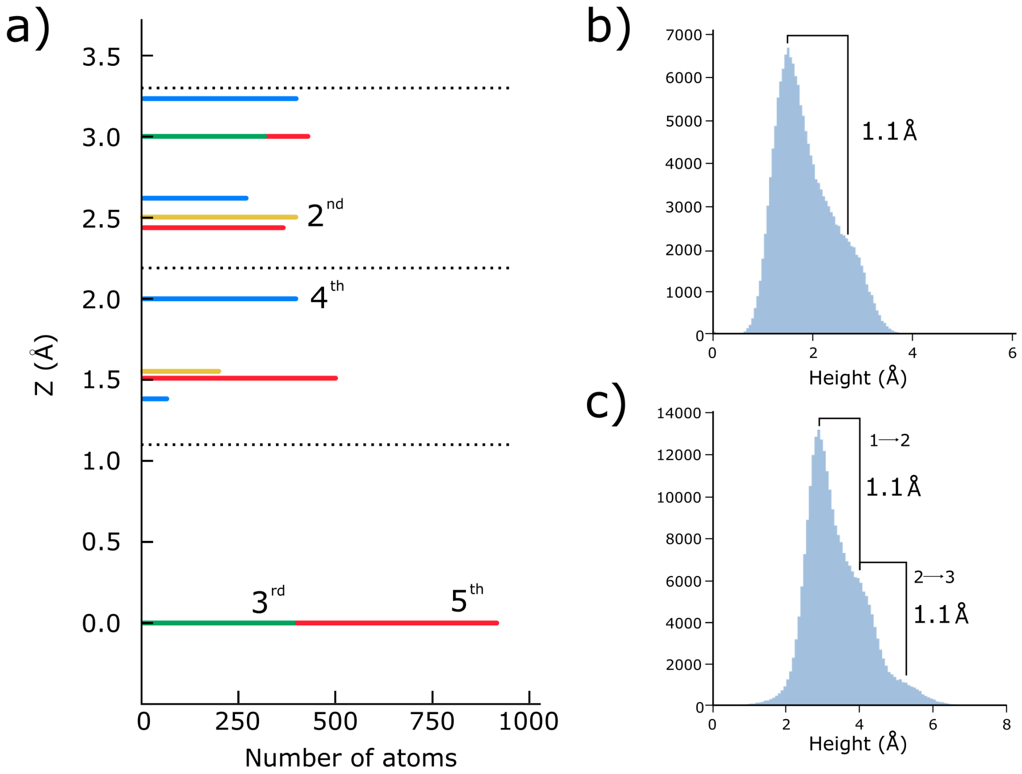

Figure 8.9: **2–fold Pb layer heights:** **(a)** The planar model along the 2–fold axis. Planes are coloured and labelled with their shell numbers as before. Marked with dotted lines are the heights of each Pb layer. **(b)** A histogram taken from Figure 8.5(a). The difference between substrate and Pb layer is marked. **c** A histogram taken from Figure 8.7(a). Marked are the height differences between the first and second, and second and third Pb layers.

between the first and second, second and third Pb layers, marked as 1→2 and 2→3. Each are $\sim$ 1.1 Å. Inspection of the planar model shows no planes at these heights, which are marked as dotted lines. Additionally, the nearest planes which could be considered (albeit with a significant relaxation in z) do not match the observed structure of the Pb in any of the layers.

Stability

Each of the other Pb/*i*–Ag–In–Yb systems have had their coverage and growth mode assessed with respect to stabilising planes. For example, the 5–fold system has inter–

and under– layers which are not observed by STM. These stabilise the film by reducing nearest neighbour distances [67]. The 3–fold system is predicted not to have these planes, as nearest neighbour distances are reduced by vertical growth, Chapter 7. As previously discussed, the Pb/2–fold system appears not to be dependent on the planar Cd–Yb model; rather, it mimics the surface on a layer–by–layer basis. Likewise, the start of the third layer before completion of the second suggests Pb is interacting primarily with itself – adsorbing at sites with low coordination numbers. Additionally, the in–plane atomic density of the 2–fold surface is the highest of all three high symmetry surfaces. As a consequence, the number of available adsorption sites at the substrate is maximal compared to the other high symmetry directions. Naturally, this density of sites reduces the nearest neighbour distance for Pb adatoms in each layer. Therefore, it is inferred that there is also no need for stabilising planes in this system.

8.4 Summary

In this chapter, the clean surface of the 2–fold orientation of the *i*–Ag–In–Yb QC was re–interpreted with respect to the Cd–Yb model. Bright protrusions observed by STM, which are most likely In atoms from the 4^{th} shell of the (Ag/In)–Yb cluster, appear to form a horizontal and vertical row structure. The remaining features observed are most likely cluster and glue Yb atoms. The enhanced resolution compared to the previous report is considered to be STM tip–induced.

After characterization of the surface, Pb was dosed over a range of coverages. Unlike the other high symmetry systems, Pb grows on the 2–fold *i*–Ag–In–Yb in a layer–by–layer fashion, adsorbing at high symmetry sites to match the density of the surface. Second and third Pb layers were observed with similar structure characteristics. The change in growth mode has been speculated to be due to the density of the surface. Higher coverage produces crystalline islands oriented along the high–symmetry axes, consistent with the other systems (see e.g. Chapter 7) [67].

Chapter 9

Summary

The aim of the work contained within this thesis was to expand the understanding of surface and adsorbate structure of quasicrystals with orders of rotational symmetry which are found in periodic systems. This was achieved through the exploration of 2–fold and 3–fold rotationally symmetric surfaces, dosed with either molecules or elemental metals. As a consequence, a number of new structures or adsorption growth–modes were identified.

First, it was shown that dosing C_{60} on the 2–fold i–Al–Pd–Mn surface produced the first example of a Fibonacci square grid in a physical system. This was attributed to a Mn distribution at the surface, predicted by a surface model which was also used to explain bright features of the clean surface. These protrusions were attributed to Al dimers which were constituents of a partially desorbed top layer. The use of C_{60} molecules here demonstrated that they can be used as a probe for determining surface structure if surface chemistry is considered. In addition to these findings, several other phases were explored on the surface. Each of these phases were tentatively identified considering the stoichiometry of the sample, and structural models which appeared to fit the STM data. C_{60} dosed on these phases gave a honeycomb structure, indicating a minimal surface–adsorbate interaction. This highlights the impact surface structure has on templated overlayers – these phases are likely chemically similar, but are structurally different to 2–fold i–Al–Pd–Mn.

Next, two 3–fold aperiodic tilings were introduced. The first was constructed in an analogous manner to the Fibonacci square grid. Here, three Fibonacci sequences were overlaid at 120° relative to each other. This produced a set of tiles, which can be used to fill all space in an aperiodic, long–range manner. Likewise, a set of vertex configuration rules were shown. In addition, a rhombus tiling was introduced which was formed by a projection of the 6D hyper–lattice used to create the Penrose P3 tiling. Again, this tiling covers all space in an aperiodic manner. Vertex configurations were shown, along with the relationship to the tri–grid tiling described above.

The rhombus tiling was then used in a reinterpretation of the 3–fold *i*–Ag–In–Yb surface. Here, protrusions which represent the centre of Cd–Yb clusters were linked by vertices of the tiling. In addition, other bright features were shown to match with the tiling. Then Pb was dosed on the surface, producing a multi–height 3D system of nano–structures. Each layer of Pb was described structurally in terms of vacant planes belonging to the Cd–Yb model. Growth was preferred along z, attributed to the surface potential representing the high atomic density of the bulk in the z direction, and low atomic density in the x–y plane. The growth–mode was identified as a quasi–island type, as, although Pb grew along z, there must be significant surface–adsorbate interaction to grow a quasicrystalline allotrope. High coverages of Pb grew crystalline islands oriented along the high symmetry directions of the surface.

Then, the 2–fold *i*–Ag–In–Yb surface was explored. A finer structure was resolved when compared to previous reports, although similar row features were seen. Bright protrusions arranged in horizontal and vertical rows were considered as In atoms from the 4^{th} shell of the Cd–Yb cluster. Then, Pb was dosed, with a quasi–Stranski–Krastanov growth mode observed. Here, a dense first layer adopted the surface structure by adsorbing at substrate sites with high geometry (hexagonal, triangular, pentagonal, square, and cluster centre sites). The second layer grew in a linear fashion, matching the row structure formed by the first layer. The third layer grew before the second had completed, indicating that the second layer sites were more attractive for adsorption than the first layer. Further Pb deposition resulted in crystalline islands oriented along the high symmetry axes of the surface.

Future studies

As speculated upon in the introduction, a full exploration of as many relevant adsorbates on as many QC surfaces as possible will lead to a better understanding of both the surfaces themselves, but also the adsorption schemes which may be specific to them. Certainly, within this thesis, the advantage of studying ‘over–looked’ surfaces has become apparent. As such, it is suggested that any potential future work should include an iterative approach to adsorption studies. By cycling through the high symmetry surfaces of a particular

QC system, and gradually working through an exhaustive list of viable adsorbates, the catalogue of information already obtained can be built upon. From here, the properties of these systems could be investigated on a more structured basis. For example, how do the properties of quasicrystalline Pb differ to quasicrystalline Bi, or C_{60}?

In addition, it would be interesting to build upon single–adsorbate systems. For instance, it is well known (and documented here) that C_{60} molecules can produce quasicrystalline networks on QC surfaces. But, can these networks be built upon themselves? A 2D multi–molecule network built upon a QC substrate would be a challenging experimental prospect, but perhaps rewarding for creating intriguing systems for exploration. Likewise, a 3D quasicrystalline multi–molecule network would be even more difficult to produce, but would be interesting for application in multi pore–size gas capture, for example.

The tilings outlined in Chapter 6 leave open questions. First of all, both tilings need strict mathematical formalism as opposed to the geometric arguments used to introduced them. This formalism is beyond the scope of this thesis, and is work for the future. Second, the specific deflation rules for both tilings are still to be found – again, problems to be solved in further work.

Aside from quasicrystalline surfaces and adsorbates, the potential for macro–scale exploration of aperiodic structures is as varied as for any other commonly used structure. For instance, how do microwaves propagate through a structure based on the Fibonacci square (or cubic) grid? How would a metal–based structure based on the 3–fold rhombus tiling act under compression? The dispersion of any energy–carrying medium through an aperiodic array could be of interest for any application based on dampening. Hopefully, these questions, as well as the ideas posed above, can be explored in the future.

List of Figures

List of Tables

Bibliography

[1] D. Shechtman, I. Blech, D. Gratias, and J. W. Cahn. Metallic phase with long-range orientational order and no translational symmetry. *Phys. Rev. Lett.*, 53(20):1951, 1984.

[2] D. Levine and P. Steinhardt. Quasicrystals: a new class of ordered structures. *Phys. Rev. Lett.*, 53(26):2477, 1984.

[3] L. Pauling. Apparent icosahedral symmetry is due to directed multiple twinning of cubic crystals. *Nature*, 317(6037):512, 1985.

[4] A. P. Tsai. Icosahedral clusters, icosahedral order and stability of quasicrystals—a view of metallurgy. *Science and Technology of Advanced Materials*, 9(1):013008, 2008.

[5] H. R. Sharma, M. Shimoda, and A. P. Tsai. Quasicrystal surfaces: structure and growth of atomic overlayers. *Advances in Physics*, 56(3):403–464, 2007.

[6] H. Takakura, C. P. Gómez, A. Yamamoto, M. de Boissieu, and A. P. Tsai. Atomic structure of the binary icosahedral Yb–Cd quasicrystal. *Nature Materials*, 6(1):58, 2007.

[7] J. Q. Guo, E. Abe, and A. P. Tsai. Stable icosahedral quasicrystals in binary Cd-Ca and Cd-Yb systems. *Phys. Rev. B*, 62(22):R14605, 2000.

[8] A. P. Tsai, J. Q. Guo, E. Abe, H. Takakura, and T. J. Sato. Alloys: A stable binary quasicrystal. *Nature*, 408(6812):537, 2000.

[9] C. Dong and J-M Dubois. Quasicrystals and crystalline phases in $Al_{65}Cu_{20}Fe_{10}Cr_5$ alloy. *Journal of Materials Science*, 26(6):1647–1654, 1991.

[10] S. Fischer, A. Exner, K. Zielske, J. Perlich, S. Deloudi, W. Steurer, P. Lindner, and S. Förster. Colloidal quasicrystals with 12-fold and 18-fold diffraction symmetry. *Proceedings of the National Academy of Sciences*, 108(5):1810–1814, 2011.

[11] M. Zu, P. Tan, and N. Xu. Forming quasicrystals by monodisperse soft core particles. *Nature Communications*, 8(1):2089, 2017.

[12] N. Wang, H. Chen, and K. H. Kuo. Two-dimensional quasicrystal with eightfold rotational symmetry. *Phys. Rev. Lett.*, 59(9):1010, 1987.

[13] K. Hayashida, T. Dotera, A. Takano, and Y. Matsushita. Polymeric quasicrystal: Mesoscopic quasicrystalline tiling inABC star polymers. *Phys. Rev. Lett.*, 98(19):195502, 2007.

[14] J-M. Dubois, S. S. Kang, and Y. Massiani. Application of quasicrystalline alloys to surface coating of soft metals. *Journal of non-crystalline solids*, 153:443–445, 1993.

[15] A. P. Tsai and M. Yoshimura. Highly active quasicrystalline Al-Cu-Fe catalyst for steam reforming of methanol. *Applied Catalysis A: General*, 214(2):237–241, 2001.

[16] S. S. Kang, J-M. Dubois, and J. Von Stebut. Tribological properties of quasicrystalline coatings. *Journal of Materials Research*, 8(10):2471–2481, 1993.

[17] J. Bamberg, G. Cairns, and D. Kilminster. The crystallographic restriction, permutations, and Goldbach's conjecture. *The American Mathematical Monthly*, 110(3):202–209, 2003.

[18] H. R. Sharma. *Structure, morphology, and dynamics of quasicrystal surfaces*. PhD thesis, Freie Universität Berlin, Universitätsbibliothek, 2002.

[19] P. Guyot, P. Kramer, and M. de Boissieu. Quasicrystals. *Reports on Progress in Physics*, 54(11):1373, 1991.

[20] C. Janot. Quasicrystals: A primer. *Monographs on the Physics and Chemistry of Materials, Oxford University Press, Oxford*, 1992.

[21] R. Lifshitz. The square Fibonacci tiling. *Journal of Alloys and Compounds*, 342(1):186–190, 2002.

[22] Z. V. Vardeny, A. Nahata, and A. Agrawal. Optics of photonic quasicrystals. *Nature Photonics*, 7(3):177–187, 2013.

[23] T. Hattori, N. Tsurumachi, S. Kawato, and H. Nakatsuka. Photonic dispersion relation in a one–dimensional quasicrystal. *Phys. Rev. B*, 50(6):4220, 1994.

[24] E. Maciá. Thermal conductivity of one-dimensional fibonacci quasicrystals. *Phys. Rev. B*, 61(10):6645, 2000.

[25] R. B. Capaz, B. Koiller, and S. L. A. de Queiroz. Gap states and localization properties of one-dimensional fibonacci quasicrystals. *Phys. Rev. B*, 42(10):6402, 1990.

[26] Y. Liu and R. Riklund. Electronic properties of perfect and nonperfect one-dimensional quasicrystals. *Phys. Rev. B*, 35(12):6034, 1987.

[27] R. Penrose. The role of aesthetics in pure and applied mathematical research. *Bull. Inst. Math. Appl.*, 10:266–271, 1974.

[28] R. Penrose. Pentaplexity: a class of non-periodic tilings of the plane. *The mathematical intelligencer*, 2(1):32–37, 1979.

[29] Y. Watanabe, M. Ito, and T. Soma. Nonperiodic tessellation with eightfold rotational symmetry. *Acta Crystallographica Section A: Foundations of Crystallography*, 43(1):133–134, 1987.

[30] P. Stampfli. A dodecagonal quasi-periodic lattice in 2 dimensions. *Helvetica Physica Acta*, 59(6-7):1260–1263, 1986.

[31] N. G. de Bruijn. Algebraic theory of Penrose's non-periodic tilings of the plane. *Kon. Nederl. Akad. Wetensch. Proc. Ser. A*, 43(84):1–7, 1981.

[32] H. Au-Yang and J. H. H. Perk. Quasicrystals: The impact of N. G. de Bruijn. *Indagationes Mathematicae*, 24(4):996–1017, 2013.

[33] J. W. Cahn, D. Shechtman, and D. Gratias. Indexing of icosahedral quasiperiodic crystals. *Journal of Materials Research*, 1(1):13–26, 1986.

[34] A. Yamamoto. Crystallography of quasiperiodic crystals. *Acta Crystallographica Section A*, 52(4):509–560, 1996.

[35] J-M. Dubois. *Useful quasicrystals.* World Scientific, 2005.

[36] M. Boudard, H. Klein, M. de Boissieu, M. Audier, and H. Vincent. Structure of quasicrystalline approximant phase in the Al–Pd–Mn system. *Philosophical Magazine A*, 74(4):939–956, 1996.

[37] A. Yamamoto, H. Takakura, and A. P. Tsai. Six-dimensional model of icosahedral Al-Pd-Mn quasicrystals. *Phys. Rev. B*, 68(9):094201, 2003.

[38] E. Abe. Electron microscopy of quasicrystals–where are the atoms? *Chemical Society Reviews*, 41(20):6787–6798, 2012.

[39] K. N. Ishihara and A. Yamamoto. Penrose patterns and related structures. I: Superstructure and generalized penrose patterns. *Acta Crystallographica Section A*, 44(4):508–516, 1988.

[40] A. I. Goldman and R. F. Kelton. Quasicrystals and crystalline approximants. *Reviews of Modern Physics*, 65(1):213, 1993.

[41] M. Cooper and K. Robinson. The crystal structure of the ternary alloy α (AlMnSi). *Acta Crystallographica*, 20(5):614–617, 1966.

[42] V. Elser and C. L. Henley. Crystal and quasicrystal structures in Al–Mn–Si alloys. *Phys. Rev. Lett.*, 55(26):2883, 1985.

[43] A. L. Mackay. A dense non–crystallographic packing of equal spheres. *Acta Crystallographica*, 15(9):916–918, 1962.

[44] G. Bergman, J. L .T. Waugh, and L. Pauling. The crystal structure of the metallic phase $Mg_{32}(Al, Zn)_{49}$. *Acta Crystallographica*, 10(4):254–259, 1957.

[45] W. Steurer and S. Deloudi. Fascinating quasicrystals. *Acta Crystallographica Section A: Foundations of Crystallography*, 64(1):1–11, 2008.

[46] W. Steurer. Stable clusters in quasicrystals: fact or fiction? *Philosophical Magazine*, 86(6-8):1105–1113, 2006.

[47] C. L. Henley, M. de Boissieu, and W. Steurer. Discussion on clusters, phasons and quasicrystal stabilisation. *Philosophical Magazine*, 86(6-8):1131–1151, 2006.

[48] J-M. Dubois, S. S. Kang, and J. Von Stebut. Quasicrystalline low-friction coatings. *Journal of Materials Science Letters*, 10(9):537–541, 1991.

[49] S. Takeuchi, H. Iwanaga, and T. Shibuya. Hardness of quasicrystals. *Japanese Journal of Applied Physics*, 30(3R):561, 1991.

[50] J-B. Suck, M. Schreiber, and P. Häussler. *Quasicrystals: An introduction to structure, physical properties and applications*, volume 55. Springer Science & Business Media, 2013.

[51] D. Gratias, F. Puyraimond, M. Quiquandon, and A. Katz. Atomic clusters in icosahedral f-type quasicrystals. *Phys. Rev. B*, 63(2):024202, 2000.

[52] A. Yamamoto, H. Takakura, and A. P. Tsai. Structure refinement of i-Al–Pd–Mn quasicrystals by IP-Weissenberg camera data. *Journal of Alloys and Compounds*, 342(1-2):159–163, 2002.

[53] Z. Papadopolos, G. Kasner, J. Ledieu, E. J. Cox, N. V. Richardson, Q. Chen, R. D. Diehl, T. A. Lograsso, A. R. Ross, and R. McGrath. Bulk termination of the quasicrystalline fivefold surface of Al-Pd-Mn. *Phys. Rev. B*, 66:184207, Nov 2002.

[54] M. Gierer, M. A. Van Hove, A. I. Goldman, Z. Shen, S.-L. Chang, C. J. Jenks, C.-M. Zhang, and P. A. Thiel. Structural analysis of the fivefold symmetric surface of the Al-Pd-Mn quasicrystal by low energy electron diffraction. *Phys. Rev. Lett.*, 78:467–470, Jan 1997.

[55] L. Barbier, D. Le Floc'h, Y. Calvayrac, and D. Gratias. Identification of the atomic structure of the fivefold surface of an icosahedral Al-Pd-Mn quasicrystal: Helium diffraction and scanning tunneling microscopy studies. *Phys. Rev. Lett.*, 88(8):085506, 2002.

[56] K. J. Franke, H. R. Sharma, W. Theis, P. Gille, Ph. Ebert, and K. H. Rieder. Quasicrystalline epitaxial single element monolayers on icosahedral Al-Pd-Mn and decagonal Al-Ni-Co quasicrystal surfaces. *Phys. Rev. Lett.*, 89(15):156104, 2002.

[57] T. M. Schaub, D. E. Bürgler, H. J. Güntherodt, and J. B. Suck. Quasicrystalline structure of icosahedral Al-Pd-Mn resolved by scanning tunneling microscopy. *Phys. Rev. Lett.*, 73:1255–1258, Aug 1994.

[58] Z. Shen, C. R. Stoldt, C. J. Jenks, T. A. Lograsso, and P. A. Thiel. Fine structure on flat surfaces of quasicrystalline Al-Pd-Mn. *Phys. Rev. B*, 60:14688–14694, Dec 1999.

[59] H. R. Sharma, M. Shimoda, and A. P. Tsai. Comparison of surface structure of icosahedral Al–Pd–Mn family quasi-crystals. *Japanese Journal of Applied Physics*, 45(3S):2208, 2006.

[60] R. McGrath, H. R. Sharma, J. A. Smerdon, and J. Ledieu. The memory of surfaces: epitaxial growth on quasi–crystals. *Phil. Trans. of R. Soc. A*, 370(1969):2930–2948, 2012.

[61] M. Krajčí and J Hafner. Ab initio study of quasiperiodic monolayers on a fivefold i-Al-Pd-Mn surface. *Phys. Rev. B*, 71(18):184207, 2005.

[62] M. Krajčí, J. Hafner, J. Ledieu, and R. McGrath. Surface vacancies at the fivefold icosahedral Al-Pd-Mn quasicrystal surface: A comparison of ab initio calculated and experimental STM images. *Phys. Rev. B*, 73:024202, Jan 2006.

[63] H. R. Sharma, V. Fournée, M. Shimoda, A. R. Ross, T. A. Lograsso, A. P. Tsai, and A. Yamamoto. Structure of the fivefold surface of the icosahedral Al-Cu-Fe quasicrystal: Experimental evidence of bulk truncations at larger interlayer spacings. *Phys. Rev. Lett.*, 93(16):165502, 2004.

[64] Ph. Ebert, M. Feuerbacher, N. Tamura, M. Wollgarten, and K. Urban. Evidence for a cluster-based structure of AlPdMn single quasicrystals. *Phys. Rev. Lett.*, 77(18):3827, 1996.

[65] H. R. Sharma, M. Shimoda, S. Ohhashi, and A. P. Tsai. First UHV surface studies of single-grain icosahedral Ag–In–Yb quasicrystal. *Philosophical Magazine*, 87(18-21):2989–2994, 2007.

[66] H. R. Sharma, M. Shimoda, K. Sagisaka, H. Takakura, J. A. Smerdon, P. J. Nugent, R. McGrath, D. Fujita, S. Ohhashi, and A. P. Tsai. Structure of the fivefold surface of the Ag-In-Yb icosahedral quasicrystal. *Phys. Rev. B*, 80(12):121401, 2009.

[67] H. R. Sharma, K. Nozawa, J. A. Smerdon, P. J. Nugent, I. McLeod, V. R. Dhanak, M. Shimoda, Y. Ishii, A. P. Tsai, and R. McGrath. Templated three-dimensional growth of quasicrystalline lead. *Nature Communications*, 4:2715, 2013.

[68] Y. Ishii and T. Fujiwara. Hybridization mechanism for cohesion of Cd-based quasicrystals. *Phys. Rev. Lett.*, 87(20):206408, 2001.

[69] W. Steurer, T. Haibach, B. Zhang, S. Kek, and R. Lück. The structure of decagonal $Al_{70}Ni_{15}Co_{15}$. *Acta Crystallographica Section B*, 49(4):661–675, 1993.

[70] A. Yamamoto and S. Weber. Five-dimensional superstructure model of decagonal Al-Ni-Co quasicrystals. *Phys. Rev. Lett.*, 78(23):4430, 1997.

[71] N. Ferralis, K. Pussi, E. J. Cox, M. Gierer, J. Ledieu, I. R. Fisher, C. J. Jenks, M. Lindroos, R. McGrath, and R. D. Diehl. Structure of the tenfold d-Al-Ni-Co quasicrystal surface. *Phys. Rev. B*, 69(15):153404, 2004.

[72] W. Kossel. Extending the law of Bravais. *Nach. Ges. Wiss. Gottingen*, 143:25, 1927.

[73] I. N. Stranski. Zur theorie des kristallwachstums. *Zeitschrift für Physikalische Chemie*, 136(1):259–278, 1928.

[74] M. I. Vesselinov. *Crystal growth for beginners: fundamentals of nucleation, crystal growth and epitaxy*. World Scientific, 2016.

[75] M. Volmer and A. Weber. Keimbildung in übersättigten gebilden. *Zeitschrift für physikalische Chemie*, 119(1):277–301, 1926.

[76] F. C. Frank and J. H. van der Merwe. One-dimensional dislocations. I. Static theory. *Proc. R. of Soc. Lond. A*, 198(1053):205–216, 1949.

[77] F. Frank and J. H. Van der Merwe. One-dimensional dislocations. II. Misfitting monolayers and oriented overgrowth. *Proc. R. of Soc. Lond. A*, 198(1053):216–225, 1949.

[78] I. N. Stranski and L. Krastanow. Zur theorie der orientierten ausscheidung von ionenkristallen aufeinander. *Monatshefte für Chemie und verwandte Teile anderer Wissenschaften*, 71(1):351–364, 1937.

[79] R. McGrath, J. A. Smerdon, H. R. Sharma, W. Theis, and J. Ledieu. The surface science of quasicrystals. *Journal of Physics: Condensed Matter*, 22(8):084022, 2010.

[80] K. J. Franke, P. Gille, K-H. Rieder, and W. Theis. Achieving epitaxy between incommensurate materials by quasicrystalline interlayers. *Phys. Rev. Lett.*, 99(3):036103, 2007.

[81] A. Zangwill. *Physics at Surfaces.* Cambridge University Press, 1988.

[82] E. J. Widjaja and L. D. Marks. Models for quasicrystal–crystal epitaxy. *Journal of Physics: Condensed Matter*, 20(31):314003, 2008.

[83] Z. Wang, X. Yang, and R. Wang. Ar^+-ion-irradiation-induced phase transformation in an $Al_{62}Cu_{25.5}Fe_{12.5}$ icosahedral quasicrystal. *Journal of Physics: Condensed Matter*, 5(41):7569, 1993.

[84] E. V. Shalaeva and A. F. Prekul. Orientation relationships between the icosahedral phase and β solid solution in quasicrystal-forming quenched $Al_{61}Cu_{26}Fe_{13}$ alloys. *The Physics of Metals and Metallography*, 101(2):141–152, 2006.

[85] Z. Shen, M. J. Kramer, C. J. Jenks, A. I. Goldman, T. Lograsso, D. Delaney, M. Heinzig, W. Raberg, and P. A. Thiel. Crystalline surface structures induced by ion sputtering of Al-rich icosahedral quasicrystals. *Phys. Rev. B*, 58:9961–9971, Oct 1998.

[86] R. Lüscher, M. Erbudak, and Y. Weisskopf. Al nanostructures on quasicrystalline Al–Pd–Mn. *Surface Science*, 569(1-3):163–175, 2004.

[87] B. Bolliger, V. E. Dmitrienko, M. Erbudak, R. Lüscher, H-U. Nissen, and A. R. Kortan. Epitactic textures of fcc Al on icosahedral Al-Pd-Mn quasicrystal. *Phys. Rev. B*, 63(5):052203, 2001.

[88] M. Shimoda, T. J. Sato, A. P. Tsai, and J. Q. Guo. Epitaxial crystalline film with psuedo-tenfold symmetry formed by Au-deposition on a decagonal $Al_{72}Ni_{12}Co_{16}$ quasicrystal. *Phys. Rev. B*, 62(17):11288, 2000.

[89] V. Fournée, J. Ledieu, M. Shimoda, Marian Krajčí, H. R. Sharma, and R. McGrath. Thin film growth on quasicrystalline surfaces. *Israel Journal of Chemistry*, 51(11-12):1314–1325, 2011.

[90] J. A. Smerdon, J. Ledieu, R. McGrath, T. C. Q. Noakes, P. Bailey, M. Draxler, C. F. McConville, T. A. Lograsso, and A. R. Ross. Characterization of aperiodic and periodic thin Cu films formed on the five-fold surface of i-Al-Pd-Mn using medium-energy ion scattering spectroscopy. *Phys. Rev. B*, 74(3):035429, 2006.

[91] K. Pussi, M. Gierer, and R. D. Diehl. The uniaxially aperiodic structure of a thin Cu film on fivefold i-Al–Pd–Mn. *Journal of Physics: Condensed Matter*, 21(47):474213, 2009.

[92] J. Ledieu, J. T. Hoeft, D. E. Reid, J. A. Smerdon, R. D. Diehl, T. A. Lograsso, A. R. Ross, and R. McGrath. Pseudomorphic growth of a single element quasiperiodic ultrathin film on a quasicrystal substrate. *Phys. Rev. Lett.*, 92(13):135507, 2004.

[93] K. M. Young, J. A. Smerdon, H. R. Sharma, M. Lahti, K. Pussi, and R. McGrath. Acene adsorption on a Fibonacci-modulated Cu film. *Phys. Rev. B*, 87(8):085407, 2013.

[94] J. Ledieu and R. McGrath. Nanostructured quasiperiodic surfaces: the origin of pentagonal hollows and their role in adsorption and nucleation processes. *Journal of Physics: Condensed Matter*, 15(42):S3113, 2003.

[95] R. McGrath, J. Ledieu, E. J. Cox, and R. D. Diehl. Quasicrystal surfaces: structure and potential as templates. *Journal of Physics: Condensed Matter*, 14(4):R119, 2002.

[96] P. A. Thiel. Quasicrystal surfaces. *Ann. Rev. Phys. Chem.*, 59:129–152, 2008.

[97] J. A. Smerdon, L. H. Wearing, J. K. Parle, L. Leung, H. R. Sharma, J. Ledieu, and R. McGrath. Ordering of adsorbed species on quasicrystal surfaces. *Philosophical Magazine*, 88(13-15):2073–2082, 2008.

[98] J. A. Smerdon, H. R. Sharma, J. Ledieu, and R. McGrath. Nucleation and growth of pseudomorphic monolayers on quasicrystal surfaces. *Journal of Physics: Condensed Matter*, 20(31):314005, 2008.

[99] T. Cai, J. Ledieu, R. McGrath, V. Fournée, T. Lograsso, A. Ross, and P. Thiel. Pseudomorphic starfish: nucleation of extrinsic metal atoms on a quasicrystalline substrate. *Surface Science*, 526(1-2):115–120, 2003.

[100] J. A. Smerdon, J. K. Parle, L. H. Wearing, T. A. Lograsso, A. R. Ross, and R. McGrath. Nucleation and growth of a quasicrystalline monolayer: Bi adsorption on the fivefold surface of i-$Al_{70}Pd_{21}Mn_9$. *Phys. Rev. B*, 78(7):075407, 2008.

[101] J. Ledieu, L. Leung, L. H. Wearing, R. McGrath, T. A. Lograsso, D. Wu, and V. Fournée. Self-assembly, structure, and electronic properties of a quasiperiodic lead monolayer. *Phys. Rev. B*, 77(7):073409, 2008.

[102] J. A. Smerdon, L. Leung, J. K. Parle, C. J. Jenks, R. McGrath, V. Fournée, and J. Ledieu. Formation of a quasicrystalline Pb monolayer on the 10-fold surface of the decagonal Al–Ni–Co quasicrystal. *Surface Science*, 602(14):2496–2501, 2008.

[103] H. R. Sharma, M. Shimoda, A. R. Ross, T. A. Lograsso, and A. P. Tsai. Real-space observation of quasicrystalline Sn monolayer formed on the fivefold surface of icosahedral Al–Cu–Fe quasicrystal. *Phys. Rev. B*, 72(4):045428, 2005.

[104] P. J. Nugent, J. A. Smerdon, R. McGrath, M. Shimoda, C. Cui, A. P. Tsai, and H. R. Sharma. Step-terrace morphology and reactivity to C_{60} of the five-fold icosahedral Ag–In–Yb quasicrystal. *Philosophical Magazine*, 91(19-21):2862–2869, 2011.

[105] V. Fournée, É. Gaudry, J. Ledieu, M-C. De Weerd, D. Wu, and T. Lograsso. Self-organized molecular films with long-range quasiperiodic order. *ACS Nano*, 8(4):3646–3653, 2014.

[106] J. Ledieu, C. A. Muryn, G. Thornton, R. D. Diehl, T. A. Lograsso, D. W. Delaney, and R. McGrath. C_{60} adsorption on the quasicrystalline surface of $Al_{70}Pd_{21}Mn_9$. *Surface Science*, 472(1):89–96, 2001.

[107] M. Quiquandon and D. Gratias. Unique six-dimensional structural model for Al–Pd–Mn and Al–Cu–Fe icosahedral phases. *Phys. Rev. B*, 74(21):214205, 2006.

[108] P. Jena, S. N. Khanna, and B. K. N. Rao. *Physics and chemistry of finite systems: from clusters to crystals*, volume 374. Springer Science & Business Media, 2013.

[109] G. Zeger, D. Plachke, H. D. Carstanjen, and H-R Trebin. Quasicrystalline d-AlCuCo identified as random tiling by ion channeling combined with particle-induced x-ray emission. *Phys. Rev. Lett.*, 82(26):5273, 1999.

[110] J. A. Smerdon, K. M. Young, M. Lowe, S. S. Hars, T. P. Yadav, D. Hesp, V. R. Dhanak, A. P. Tsai, H. R. Sharma, and R. McGrath. Templated quasicrystalline molecular ordering. *Nano Letters*, 14(3):1184–1189, 2014.

[111] William IF David, Richard M Ibberson, Judy C Matthewman, Kosmas Prassides, T John S Dennis, Jonathan P Hare, Harold W Kroto, Roger Taylor, and David RM Walton. Crystal structure and bonding of ordered c60. *Nature*, 353(6340):147–149, 1991.

[112] J. A. Gardener, G. A. D. Briggs, and M. R. Castell. Scanning tunneling microscopy studies of C_{60} monolayers on Au(111). *Phys. Rev. B*, 80(23):235434, 2009.

[113] G. Schull and R. Berndt. Orientationally ordered (7× 7) superstructure of C_{60} on Au (111). *Phys. Rev. Lett.*, 99(22):226105, 2007.

[114] T. Hashizume, K. Motai, X. D. Wang, H. Shinohara, H. W. Pickering, and T. Sakurai. Intramolecular structures of C_{60} adsorbed on the Cu (111) 1× 1 surface studied by the field ion-scanning tunneling microscopy. *Journal of Vacuum Science & Technology A: Vacuum, Surfaces, and Films*, 12(4):2097–2100, 1994.

[115] N. A. Wasio, R. C. Quardokus, R. P. Forrest, C. S. Lent, S. A. Corcelli, J. A. Christie, K. W. Henderson, and S. A. Kandel. Self-assembly of hydrogen-bonded two-dimensional quasicrystals. *Nature*, 507(7490):86, 2014.

[116] N. Kalashnyk, J. Ledieu, É. Gaudry, C. Cui, A. P. Tsai, and V. Fournée. Building 2D quasicrystals from 5-fold symmetric corannulene molecules. *Nano Research*, 11(4):2129–2138, 2018.

[117] X. Zeng, G. Ungar, Y. Liu, V. Percec, A. E. Dulcey, and J. K. Hobbs. Supramolecular dendritic liquid quasicrystals. *Nature*, 428(6979):157, 2004.

[118] Z. Zhou and K. D. M. Harris. Design of a molecular quasicrystal. *ChemPhysChem*, 7(8):1649–1653, 2006.

[119] M. O. Blunt, J. C. Russell, M. del Carmen Giménez-López, J. P. Garrahan, X. Lin, M. Schröder, N. R. Champness, and P. H. Beton. Random tiling and topological defects in a two-dimensional molecular network. *Science*, 322(5904):1077–1081, 2008.

[120] K. Oura, V. G. Lifshits, A. A. Saranin, A. V. Zotov, and M. Katayama. *Surface science: an introduction.* Springer Science & Business Media, 2013.

[121] E. Belin-Ferré. *Quasicrystals: Current Topics: Aussois, France, 16-21 May 1999.* World Scientific, 2000.

[122] P. J. Nugent, G. Simutis, V. R. Dhanak, R. McGrath, M. Shimoda, C. Cui, A. P. Tsai, and H. R. Sharma. Surface oxidation of the icosahedral Ag-In-Yb quasicrystal. *Phys. Rev. B*, 82(1):014201, 2010.

[123] A-P. Tsai and C. Cui. Crystal Growth of Quasicrystals. In *Handbook of Crystal Growth*, pages 1113–1156. Elsevier, 2015.

[124] J. Czochralski. Ein neues verfahren zur messung der kristallisationsgeschwindigkeit der metalle. *Zeitschrift für physikalische Chemie*, 92(1):219–221, 1918.

[125] P. W. Bridgman. Certain physical properties of single crystals of tungsten, antimony, bismuth, tellurium, cadmium, zinc, and tin. In *Proceedings of the American Academy of Arts and Sciences*, volume 60, pages 305–383. JSTOR, 1925.

[126] B. Bolliger, M. Erbudak, A. Hensch, and D. D. Vvedensky. Surface structural phase transitions on icosahedral Al-Pd-Mn. *Mat. Sci. Eng.: A*, pages 859–862, 2000.

[127] G. Binnig and H. Rohrer. Scanning tunneling microscopy. *Surface Science*, 126(1-3):236–244, 1983.

[128] I. Horcas, Rs. Fernández, J. M. Gomez-Rodriguez, J. W. S. X. Colchero, J. W. S. X. M. Gómez-Herrero, and A. M. Baro. WSXM: a software for scanning probe microscopy and a tool for nanotechnology. *Review of Scientific Instruments*, 78(1):013705, 2007.

[129] D. Nečas and P. Klapetek. Gwyddion: an open-source software for SPM data analysis. *Open Physics*, 10(1):181–188, 2012.

[130] R. D. Diehl, J. Ledieu, N. Ferralis, A. W. Szmodis, and R. McGrath. Low-energy electron diffraction from quasicrystal surfaces. *Journal of Physics: Condensed Matter*, 15(3):R63, 2003.

[131] Z. Shen, C. J. Jenks, J. Anderegg, D. W. Delaney, T. A. Lograsso, P. A. Thiel, and A. I. Goldman. Structure and stability of the twofold surface of icosahedral Al-Pd-Mn by low-energy electron diffraction and x-ray photoemission spectroscopy. *Phys. Rev. Lett.*, 78(6):1050, 1997.

[132] D. Reid, J. A. Smerdon, J. Ledieu, and R. McGrath. The clean and copper-dosed two-fold surface of the icosahedral Al–Pd–Mn quasicrystal. *Surface Science*, 600(18):4132–4136, 2006.

[133] O. Gröning, R. Widmer, P. Ruffieux, and P. Gröning. Scanning tunnelling microscopy with atomic resolution on the twofold surface of the icosahedral AlPdMn quasicrystal. *Philosophical Magazine*, 86(6-8):773–779, 2006.

[134] V. Fournée, A.R. Ross, T.A. Lograsso, J.W. Evans, and P.A. Thiel. Growth of Ag thin films on complex surfaces of quasicrystals and approximant phases. *Surface Science*, 537(1–3):5 – 26, 2003.

[135] M. Boudard, M. de Boissieu, Ch. Janot, G. Heger, C. Beeli, H-U. Nissen, H. Vincent, R. Ibberson, M. Audier, and J-M. Dubois. Neutron and X-ray single-crystal study of the AlPdMn icosahedral phase. *Journal of Physics: Condensed Matter*, 4(50):10149, 1992.

[136] Fournée, V. and Ross, A. R. and Lograsso, T. A. and Anderegg, J. W and Dong, C. and Kramer, M. and Fisher, I. R. and Canfield, P. C. and Thiel, P. A. Surface structures of approximant phases in the Al-Pd-Mn system. *Phys. Rev. B*, 66(16):165423, 2002.

[137] J. Ledieu, P. Unsworth, T. A. Lograsso, A. R. Ross, and R. McGrath. Ordering of Si atoms on the fivefold Al-Pd-Mn quasicrystal surface. *Phys. Rev. B*, 73(1):012204, 2006.

[138] R. C. Haddon. The fullerenes: powerful carbon-based electron acceptors. *Phil. Trans. R. Soc. Lond. A*, 343(1667):53–62, 1993.

[139] J. Ledieu, C. A. Muryn, G. Thornton, G. Cappello, J. Chevrier, R. D. Diehl, T. A. Lograsso, D. Delaney, and R. McGrath. Decomposition of the five-fold surface of $Al_{70}Pd_{21}Mn_9$ at elevated temperature. *Materials Science and Engineering: A*, 294:871–873, 2000.

[140] Z. Shen, M. J. Kramer, C. J. Jenks, A. I. Goldman, T. Lograsso, D. Delaney, M. Heinzig, W. Raberg, and P. A. Thiel. Crystalline surface structures induced by ion sputtering of Al-rich icosahedral quasicrystals. *Phys. Rev. B*, 58(15):9961, 1998.

[141] P. Villars and L. D. Calvert. Pearson's Handbook of Crystallographic Data for Intermediate Phases. *American Society of Metals, Cleveland, OH*, 1985.

[142] B. Grushko. Again regarding the Al–Pd phase diagram. *Journal of Alloys and Compounds*, 557:102–111, 2013.

[143] H. Poincaré. Mathematical creation. *The Monist*, pages 321–335, 1910.

[144] D. Wells. Are these the most beautiful? *The Mathematical Intelligencer*, 12(3):37–41, 1990.

[145] N. Sinclair. The aesthetic "is" relevant. *For the learning of mathematics*, 21(1):25–32, 2001.

[146] N. Sinclair. The kissing triangles: The aesthetics of mathematical discovery. *International Journal of Computers for Mathematical Learning*, 7(1):45–63, 2002.

[147] N. Sinclair. The roles of the aesthetic in mathematical inquiry. *Mathematical Thinking and Learning*, 6(3):261–284, 2004.

[148] H. R. Sharma, K. J. Franke, W. Theis, A. Riemann, S. Fölsch, P. Gille, and K. H. Rieder. Structure and morphology of the tenfold surface of decagonal $Al_{71.8}Ni_{14.8}Co_{13.4}$ in its low-temperature random tiling type-I modification. *Phys. Rev. B*, 70(23):235409, 2004.

[149] S. Förster, K. Meinel, R. Hammer, M. Trautmann, and W. Widdra. Quasicrystalline structure formation in a classical crystalline thin-film system. *Nature*, 502(7470):215, 2013.

[150] R. M. Robinson. Undecidability and nonperiodicity for tilings of the plane. *Inventiones mathematicae*, 12(3):177–209, 1971.

[151] M. Baake, M. Scholottmann, and P. D. Jarvis. Quasiperiodic tilings with tenfold symmetry and equivalence with respect to local derivability. *Journal of Physics A: Mathematical and General*, 24(19):4637, 1991.

[152] W. Steurer and T. Haibach. *Reciprocal-space images of aperiodic crystals.* Wiley Online Library, 2010.

[153] W. Steurer and J. Dshemuchadse. *Intermetallics: structures, properties, and statistics*, volume 26. Oxford University Press, 2016.

[154] C. Cui, P. J. Nugent, M. Shimoda, J. Ledieu, V. Fournée, A. P. Tsai, R. McGrath, and H. R. Sharma. The atomic structure of the threefold surface of the icosahedral Ag–In–Yb quasicrystal. *Journal of Physics: Condensed Matter*, 24(44):445011, 2012.

[155] C. Cui, M. Shimoda, and A. P. Tsai. Studies on icosahedral Ag–In–Yb: a prototype for Tsai-type quasicrystals. *RSC Advances*, 4(87):46907–46921, 2014.

[156] C. Cui, P. J. Nugent, M. Shimoda, J. Ledieu, V. Fournée, A. P. Tsai, R. McGrath, and H. R. Sharma. Structure of the twofold surface of the icosahedral Ag–In–Yb quasicrystal. *Journal of Physics: Condensed Matter*, 26(1):015001, 2013.

[157] S. S. Hars, H. R. Sharma, J. A. Smerdon, S. Coates, K. Nozawa, A. P. Tsai, and R. McGrath. Growth of a bismuth thin film on the five-fold surface of the icosahedral Ag–In–Yb quasicrystal. *Surface Science*, 2018.

[158] H. Euchner, T. Yamada, S. Rols, T. Ishimasa, Y. Kaneko, J. Ollivier, H. Schober, M. Mihalkovic, and M. de Boissieu. Tetrahedron dynamics in the icosahedral quasicrystals i-ZnMgSc and i-ZnAgSc and the cubic 1/1-approximant Zn_6Sc. *Journal of Physics: Condensed Matter*, 25(11):115405, 2013.

[159] C. P. Gómez and S. Lidin. Comparative structural study of the disordered M–Cd_6 quasicrystal approximants. *Phys. Rev. B*, 68(2):024203, 2003.

[160] K. Nishimoto, T. Sato, and R. Tamura. Low-temperature superstructures of a series of Cd_6–M (M= Ca, Y, Sr, Pr, Nd, Sm, Gd, Tb, Dy, Ho, Er, Tm, Yb and Lu) crystalline approximants. *Journal of Physics: Condensed Matter*, 25(23):235403, 2013.

[161] M. Mantina, A. C. Chamberlin, R. Valero, C. J. Cramer, and D. G. Truhlar. Consistent van der Waals radii for the whole main group. *The Journal of Physical Chemistry A*, 113(19):5806–5812, 2009.

[162] H. R. Sharma, J. A. Smerdon, P. J. Nugent, A. Ribeiro, I. McLeod, V. R. Dhanak, M. Shimoda, A. P. Tsai, and R. McGrath. Crystalline and quasicrystalline allotropes of Pb formed on the fivefold surface of icosahedral Ag-In-Yb. *The Journal of Chemical Physics*, 140(17):174710, 2014.

[163] M. Sierpiński. Sur une courbe dont tout point est un point de ramification. *Compte Rendus hebdomadaires des seance de l'Academie des Science de Paris*, 160:302–305, 1915.

[164] E. W. Weisstein. Sierpiński Sieve, http://mathworld.wolfram.com/SierpinskiSieve.html.

[165] H. J. Jeffrey. Chaos game representation of gene structure. *Nucleic acids research*, 18(8):2163–2170, 1990.

[166] P. W. K. Rothemund, N. Papadakis, and E. Winfree. Algorithmic self-assembly of DNA Sierpinski triangles. *PLoS biology*, 2(12):e424, 2004.

[167] E. Bullmore, M. Brammer, I. Harvey, R. Persaud, R. Murray, and M. Ron. Fractal analysis of the boundary between white matter and cerebral cortex in magnetic resonance images: a controlled study of schizophrenic and manic-depressive patients. *Psychological medicine*, 24(3):771–781, 1994.

[168] A. Soesoo, J. Kalda, P. Bons, K. Urtson, and V. Kalm. Fractality in geology: a possible use of fractals in the studies of partial melting processes. In *Proceedings of the Estonian Academy of Sciences, Geology*, volume 53, pages 13–27. Estonian Academy Publishers, 2004.

[169] Y. Fisher. Fractal image compression. *Fractals*, 2(03):347–361, 1994.

[170] K. J. Hsü and A. Hsü. Self-similarity of the "1/f noise" called music. *Proceedings of the National Academy of Sciences*, 88(8):3507–3509, 1991.

[171] J. Shang, Y. Wang, M. Chen, J. Dai, X. Zhou, J. Kuttner, G. Hilt, X. Shao, J. M. Gottfried, and K. Wu. Assembling molecular Sierpiński triangle fractals. *Nature chemistry*, 7(5):389, 2015.

[172] C. Li, X. Zhang, N. Li, Y. Wang, J. Yang, G. Gu, Y. Zhang, S. Hou, L. Peng, K. Wu, et al. Construction of Sierpiński Triangles up to the Fifth Order. *Journal of the American Chemical Society*, 139(39):13749–13753, 2017.

[173] S. N. Kempkes, M. R. Slot, S. E. Freeney, S. J. M. Zevenhuizen, D. Vanmaekelbergh, I. Swart, and C. M. Smith. Design and characterization of electrons in a fractal geometry. *Nature Physics*, page 1, 2018.

[174] D. Broomhead, J. Montaldi, and N. Sidorov. Golden gaskets: variations on the Sierpiński sieve. *Nonlinearity*, 17(4):1455, 2004.

Appendix A

τ–deflated Sierpiński triangle

The Sierpiński triangle is a fractal constructed by recursively subdividing an equilateral triangle into three smaller equilateral triangles [163]. Its mathematical definition is beyond the scope of this work, so it will be defined simplistically. Other resources can be used to explore its definition, such as [164], and references therein. Like many other fractal entities, its usefulness is not just limited to its aesthetic qualities. Its mathematical definition is applicable in biology with examples including self–assembly of DNA, gene structure, and diagnostic medicine [165–167]. Other fields include geology [168], image processing

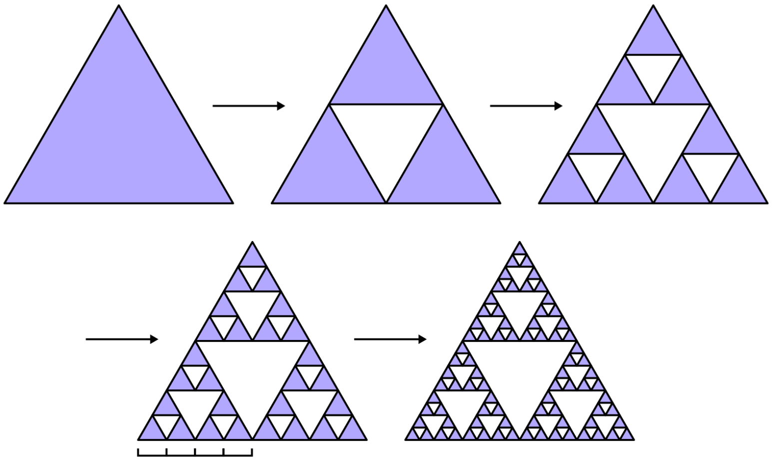

Figure A.1: **Sierpiński triangle after 4 generations:** Starting from top left, an equilateral triangle is subdivided into 3 smaller equilateral triangles. Each successive triangle is recursively treated in the same manner.

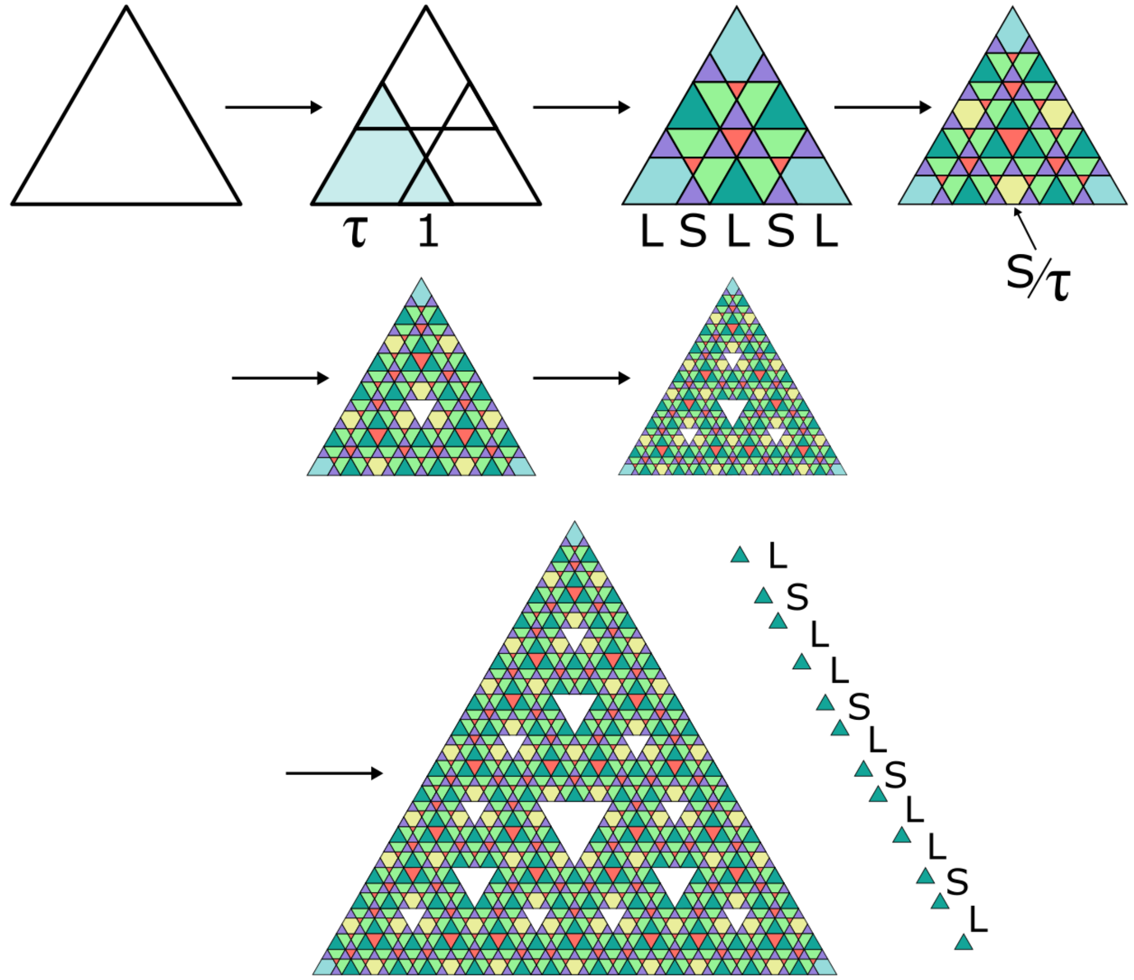

Figure A.2: **Aperiodic Sierpiński triangle** An aperiodic tiling is created using the Sierpiński triangle method. Labelled across the figure are τ and Fibonacci sequence–related lengths and tiles.

[169], and music theory [170]. Examples of experimentally constructed Sierpiński triangles include molecular arrays, and a quantum fractal produced by CO on a copper surface [171–173].

Figure A.1 shows how the triangle is constructed. An equilateral triangle is shrunk into 3 equilateral triangles, and each are placed at the vertices of the original triangle. Importantly, the ratio of edge lengths between the first generation and the original triangle is given as $n = 0.5$. Now, each of these triangles is shrunk, and so on. Figure A.1 shows

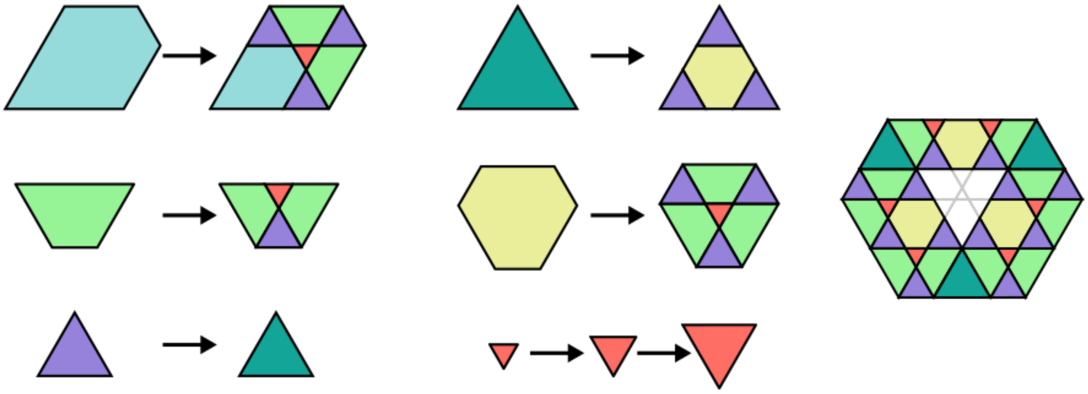

Figure A.3: **'Tiles' of the aperiodic Sierpiński triangle:** Each tile created using the Sierpiński method is shown, with deflation rules for each. On the right hand side is a hole, with grey lines showing 'leap–of–faith' tiles inside.

the procedure for 4 generations. The end result is a self–similar fractal, with large holes created. Labelled underneath the 3$^{\text{rd}}$ generation are a set of line segments corresponding to the base of several triangles. They form a periodic sequence.

Now, if the ratio of the edge lengths between successive generations, n, is altered, these triangles can either overlap (if n is increased) or create enlarged holes (if n is decreased). If we choose an irrational ratio so that $n = 1/\tau = 0.618...$ then the overlap creates a fractal triangle with an in–built relationship to the Fibonacci sequence. Broomhead, Montaldi, and Sidorov provide a generalization and some properties of the case of a Sierpiński system with $n = 0.618...$ [174]. Here, it shall be shown that it has links to an aperiodic tiling. Figure A.2 shows such a construction. The first generation has its bottom left triangle coloured to highlight the overlap on its top and right–hand corners.

The overlap creates a set of 'tiles': three triangles, three kite type tiles, and a smaller centre triangle, or hole. The ratio of the labelled kite edge length to the triangles is τ:1, as marked. Likewise, a section of the Fibonacci sequence is labelled on the edge lengths of the second generation. As the generations progress, the sequence of edge lengths includes S/τ positions as noted on the third generation. These can be combined with nearby S edge lengths to create an L length, upholding the Fibonacci sequence. Likewise, individual tiles are separated by a Fibonacci sequence, as shown adjacent to the sixth generation. This behaviour occurs along each of the three high symmetry directions. As this construction is self–similar, each of the constituent tiles can be deflated. Figure A.3 shows the constituent tiles, and each of their deflation rules. Amongst several colours of triangles are a kite (blue), a trapezoid (light green), and a shield (yellow).

It should be noted that the red downwards facing triangle tiles are not strictly part of the Sierpiński triangle. They are a coincidence of the overlapping geometry, and should simply be holes. These tiles are eventually replaced by a hole once their edges do not coincide with surrounding tiles. However, a secondary tiling can be created if the hole is treated as a tile – taking a 'leap of faith' by continuing the coincidental lines that surround the hole. An example is shown in Figure A.3. Light grey lines therefore infer the deflation rules of the hole. These create the same tiles of the original deflation (generation 1), yet inverted, with τ–deflated edge lengths compared to the 'original' tiles. Indeed, if one re–applies this method after each generation, a second set of tiles is created. These tiles are the same shapes as the first set, but rather, are all τ–deflated and inverted. As such, their deflation rules are different. This second set of tiles then produces upward facing holes. Eventually, these holes grow large enough to require another leap–of–faith, leading to the creation of the original set of tiles. Therefore, each 'version' of this leap–of–faith tiling creates either up or down holes which self–perpetuates the other version.

Here, a purely geometric link has been made between a Sierpiński system and two aperiodic 'tilings'. The first is constructed from a set of 5 tiles, with 3 additional tiles filling certain sized holes created by the overlapping nature of the Sierpiński triangle method. Each tile has a set of deflation rules. The growth of large holes in the tiling could be considered analogous to the 'dead' surfaces created by building a Penrose P3 tiling only using edge–matching rules [20]. The second tiling is created by extending the lines of the original across these holes. These create further tiles in a fractal manner. Both versions exhibit aperiodicity as a result of the ratio $n = 1/\tau$. Their long–range order is guaranteed by their fractal nature. Likewise, 3–fold symmetry is guaranteed by the nature of the Sierpiński deflation i.e. placing triangles at the corners of triangles.

Appendix B

Publications

Project Publications

- **S. Coates**, J. Smerdon, R. McGrath and H. R. Sharma. A molecular overlayer with the Fibonacci square grid structure. *Nature Communications*, 9, 2018.
- **S. Coates**, S. Thorn, R. McGrath, and H. R. Sharma. Quasicrystalline Pb nanostructures at the 3–fold *i*–Ag–In–Yb surface. *In preparation.*
- **S. Coates**, R. McGrath, and H. R. Sharma. Pb thin film on 2–fold *i*–Ag–In–Yb. *In preparation.*
- **S. Coates**, R. McGrath, and H. R. Sharma. C_{60} adsorption on periodic phases of the 2–fold *i*–Al–Pd–Mn surface. *In preparation.*
- **S. Coates**, S. Thorn, R. McGrath, and H. R. Sharma. Pb on high symmetry surfaces of the *i*–Ag–In–Yb system: a review. *In preparation.*
- **S. Coates**, R. Lifshitz, U. Grimm. A 3–fold aperiodic tiling. *In preparation.*

Other Publications

- **S. Coates**, A. Al–Mahboob, R. McGrath, H. R. Sharma. Preparation dependent surface structure of NiAl(100). *Journal of Physics: Conference Series*, 809(1). IOP Publishing, 2017.

- S. S. Hars, H. R. Sharma, J. A. Smerdon, **S. Coates**, K. Nozawa, A. P. Tsai, R. McGrath. Growth of a bismuth thin film on the five-fold surface of the icosahedral Ag–In–Yb quasicrystal. *Surface Science*, 678: 222-227, 2018.
- **S. Coates**, D. Burnie, J. Ledieu, V. Fournée, H. R. Sharma. ZnPc on Al_9Co_2. *In preparation.*

Oral Presentations

- *Quasicrystalline overlayers with orders of rotational symmetry commensurate with periodic systems.* Invited seminar, Argonne National Lab, 2018.
- *Quasicrystalline overlayers with orders of rotational symmetry commensurate with periodic systems.* Aperiodic Conference, 2018.
- *Surface structure determination using C_{60}.* RSC: Structure and Chemistry Symposium London, 2018.
- *Fibonacci modulation of a C_{60} thin film.* C–MAC days, 2017.
- *ZnPc adsorption on Al–based intermetallic alloys.* C–MAC days, 2016.
- *Preparation dependent surface structure of NiAl(100).* ICQ13, 2016.

Poster Presentations

- *Quasicrystalline overlayers with orders of rotational symmetry commensurate with periodic systems.* Aperiodic Conference, 2018.
- *Quasicrystalline overlayers with orders of rotational symmetry commensurate with periodic systems.* Surface Science Day, 2018.
- *Fibonacci modulation of a C_{60} thin film.* Surface Science Day, 2017.
- *ZnPc adsorption on Al–based intermetallic alloys.* NANOENERGY, 2016.
- *Preparation dependent surface structure of NiAl(100).* C–MAC Euroschool, 2016.
- *Quasicrystals as catalysts for the steam reforming of methanol.* C–MAC days, 2015.